Leibniz
Universität
Hannover

Resonant High Harmonic Generation and Extreme-Ultraviolet Frequency Combs Driven by Few-Cycle Laser Pulses

Von der Fakultät für Mathematik und Physik
der Gottfried Wilhelm Leibniz Universität Hannover
zur Erlangung des Grades
DOKTORIN DER NATURWISSENSCHAFTEN (Dr. rer. nat.)

genehmigte Dissertation
von
Maria Tudorovskaya
geboren am 14.05.1985, in Moskau

2015

Referenten:

Prof. Dr. Manfred Lein (Leibniz Universität Hannover)
Prof. Dr. Alejandro Saenz (Humboldt-Universität zu Berlin)

Mitglieder der Promotionskommission:

Prof. Dr. Christian Ospelkaus (Leibniz Universität Hannover)
Prof. Dr. Manfred Lein (Leibniz Universität Hannover)
Prof. Dr. Klemens Hammerer (Leibniz Universität Hannover)

Tag der Promotion:

15. Juli 2015

Keywords:

high harmonic generation
two-state quantum system
extreme-ultraviolet frequency comb

Schlagworte:

Erzeugung hoher Harmonischer
Zweizustandssystem
Extrem-Ultraviolett Frequenzkamm

Table of Contents

List of Figures

List of Tables

List of Abbreviations

ATI	Above Threshold Ionization
CEP	Carrier Envelope Phase
FQ	Frequency Comb
FWHM	Full Width at Half Maximum
HHG	High(-Order) Harmonic Generation
IR	Infrared
MPI	Multi-Photon Ionization
RWA	Rotating Wave Approximation
SEA	Single-Electron Approximation
SFA	Strong Field Approximation
SOM	Split-Operator Method
TDSE	Time Dependent Schrödinger Equation
XUV	Extreme Ultraviolet

List of Symbols

ϵ	HHG driving field ellipticity
ϵ_0	vacuum permittivity
$\mathcal{E}_{\mathrm{g,e,res}}$	ground, bound excited or resonant metastable state energy
γ	Keldysh parameter
Γ	metastable state width
ω_0	IR laser field frequency
ω_{XUV}	XUV field frequency
$\mathcal{E}_i$	energy of the quantum state i
μ_{ij}	dipole matrix element corresponding to the transition between the states i and j
ϕ_0	CEP, phase of HHG-driving laser field
I or I_i	laser field intensity
I_a	atomic unit of field intensity
I_p	ionization potential
U_p	ponderomotive potential
E_0	driving laser field intensity
E_a	atomic unit of field strength
r_c	characteristic travel distance of an electron
V_0	model potential well
V_0^{2l}	potential well with two bound states
V_0^{res}	potential well with one stable and one metastable states
$\mathbf{v}_{\mathrm{drift}}$	electron drift verlocity
t_i and t_r	ionization and recombination times, respectively
$XUV_{l,s}$	long or short XUV pulse

Zusammenfassung

In der vorliegenden Doktorarbeit untersuchen wir Aspekte der Wechselwirkung zwischen Atomen und starken Laserfeldern. Unser Hauptaugenmerk liegt dabei auf der Erzeugung hoher Harmonischer (HHG), die durch starke Infrarot-Laserpulse angetrieben werden. Mit Hilfe von HHG kann man kohärente Lichtquellen schaffen, die das extreme Ultraviolett erreichen und die spektrale Peaks bei ungeraden Vielfachen der Laserfrequenz (sogenannte Harmonische) aufweisen. Wir interessieren uns für die Maximierung der Signalstärke der hohen Harmonischen, weil geringe Effizienz ein Schlüsselproblem der HHG ist. Wir diskutieren sowohl die Verstärkung von individuellen Peaks im HHG-Spektrum als auch die Gesamtemission. Dafür verwenden wir numerische Simulationen der HHG in Atomen mit gebundenen oder metastabilen angeregten Zuständen. Wir untersuchen die Rolle, die ein angeregter Zustand in der Effizienzsteigerung spielt, sowie seinen Einfluss auf die Position und relative Höhe der Peaks. Wir zeigen weiterhin, dass die Peakerhöhung in Gegenwart einer Resonanz erklärt werden kann durch ein Einfangen der ionisierten Elektronen in einen angeregten Zustand und den folgenden Übergang in den Grundzustand. Wir zeigen auch wie die Lebensdauer des angeregten Zustands sich auf die Parameter der resonanten Erhöhung im HHG-Spektrum auswirkt. Um die Gültigkeit des Modells zu beweisen, vergleichen wir unsere Simulationsergebnisse mit einem HHG-Experiment für ein Mangan-Plasma bei verschiedenen Längen der Laserpulse. Wir verwenden die Energie und die Lebensdauer der Riesenresonanz in Mangan um ein Modell-Potential zu konstruieren, in dem der angeregte Zustand die gewünschten Parameter besitzt. Eine qualitative Übereinstimmung der numerischen Ergebnisse mit dem Experiment wird nachgewiesen. Wir betrachten den Effekt eines zusätzlichen extremen ultravioletten Pulses und seine mögliche Rolle bei der harmonischen Emissionssteigerung. Wir zeigen, dass der Extrem-Ultraviolett-Puls Elektronenübergänge induziert und diskutieren die optimale Intensität und Dauer des Pulses. Unser Modell beschreibt elektronische Rabi-Oszillationen und die Aufspaltung der damit verbunden spektralen Peaks. Wir erwähnen auch Eigenschaften und Effizienz des verwandten Prozesses der Erzeugung von schnellen Elektronen, wobei das System mit mehr Photonen als erforderlich ionisiert wird. Zuletzt betrachten wir die Erzeugung von hohen Harmonischen durch Laserpulszüge, um einen Frequenzkamm im extremen Ultraviolett herzustellen. Das Spektrum, das bei HHG mit Pulszügen erhalten wird, hat eine Kammstruktur aufgrund der sich wiederholenden Pulse innerhalb des Zuges. Wir zeigen, dass die "Dichte" des XUV-Frequenzkamms bei sehr kurzen Pulsen offset-abhängig ist, und dass die Position der Zähne definiert wird durch die harmonische Ordnung, zu dem die betrachteten Peaks gehören.

Abstract

In this Thesis we study aspects of the interaction between atoms and powerful laser fields. We focus our attention on high(-order) harmonic generation (HHG), driven by strong infrared laser pulses as a way to produce a coherent source of light reaching the extreme ultraviolet with spectral peaks at odd multiples of the driving laser frequency (so called harmonics). The subject of our interest is to increase high harmonic emission, since low efficiency is one of the key problems of HHG. We discuss both enhancement of individual HHG harmonics as well as the overall emission. We perform numerical simulations of HHG by an atom involving bound or metastable excited states and show the role an excited state plays in the HHG efficiency enhancement and spectrum properties, such as peak positions and relative heights. We show that in the presence of a resonance, the individual peak enhancement is due to the ionized electrons being recaptured by the excited state with the following transition into the ground state. We also show how the excited state lifetime affects parameters of the resonant peak in the HHG spectrum. In order to prove the validity of the model, we make a comparison of the simulation results with an experiment of HHG in manganese plasma for different durations of the laser pulse. We use the energy and the lifetime of the giant resonance in manganese to construct a model potential with corresponding parameters of the excited state, and qualitative agreement of the numerical results with the experiment is demonstrated. We consider the effect of an additional extreme ultraviolet pulse and its possible role in harmonic emission enhancement. We show that the extreme ultraviolet pulse induces electron transitions and discuss the pulse optimal intensity and duration. Our model describes electronic Rabi oscillations and spectral peak splitting associated with them. We touch on properties and efficiency of the related process of above threshold ionization, in which the system is ionized with a higher number of photons than is required for single ionization. Finally, we consider the implementation of high harmonic generation by laser pulse trains for extreme-ultraviolet frequency-comb creation. The spectrum obtained by high harmonic generation with pulse trains leads to a comb structure due to the repetitive nature of the pulses within the train. We show that for few-cycle laser pulses, the XUV frequency comb density is offset-dependent, and the teeth positions are defined by the harmonic order the teeth belong to.

Outline

In the following, we give an overview of the Thesis structure. We start with a brief theoretical review of strong-field processes and commonly used theoretical methods (see Chapter 1) allowing the reader to understand them on both the intuitive semiclassical and quantum mechanical levels.

We proceed with a discussion on the methodological approach to the numerical experiments. We use numerical methods to solve the time-dependent Schrödinger equation in the dipole approximation in the presence of the electric field and neglecting the magnetic field contribution as explained in Chapter 2.

Chapter 3 is dedicated to high harmonic generation in the presence of a shape resonance. Due to its specific shape, the potential supports an excited state with finite lifetime, leading to selective harmonic enhancement. We use a model potential well to investigate high harmonic generation in systems with such a quasi-bound excited state. This approach allows to judge the position, width and height of the resonance in the harmonic spectrum. From the time-frequency analysis of the intensity and phase of the generated harmonics, we find that the results support the four-step model[137] involving the trapping in the resonance as an intermediate step of the process. We find that the resonance gives rise to a clear signature in the HHG spectrum irrespective of the pulse length and the excited state lifetime. We use intensity averaging as a way to model the process in a medium and find that macroscopic effects do not reduce the presence of the resonance. We compare the results of our simulation with an experiment of high harmonic generation in a manganese plasma and show good qualitative agreement.

In Chapter 4, we investigate the generation of high harmonics and above threshold ionization driven by infrared fields assisted by ultraviolet fields. We show that in a quantum system with a bound or metastable excited electronic state, adding a moderate near-resonant extreme ultraviolet pulse can lead to enormous enhancement of photon emission due to populating of the excited state. We also find that in the harmonic generation spectra, the positions of the peaks are shifted away from odd orders of the infrared frequency. We study the dependence of the peak positions on the lifetime of the excited state and the pulse duration.

Finally, Chapter 5 touches a different aspect of HHG, namely applying infrared pulse trains to generate high harmonics. A train consisting of many pulses forms a comb in the frequency domain. HHG can be used to create frequency combs in the ultraviolet and extreme ultraviolet frequency ranges. Since the purpose of the frequency combs is in precision spectroscopy, the exact positions of the comb teeth are of great importance. We look in detail at the structure of the resulting frequency combs depending on the driving field properties such as number of pulses in the train, their duration and relative phase shift (offset phase). We find that ultra-short pulses leading to overlapping harmonics also produce a more dense frequency comb with the density depending on the offset frequency. In particular, we consider the case of an irrational ratio between offset frequency and repetition frequency and find conditions at which the comb can still be observed.

Chapter 1

Introduction to strong-field processes

The development of lasers started a new era in light-atom interaction studies. Before lasers became available, only monochromatic light intensities up to ≈ 10 W/cm^2 were available. Nowadays, with pulsed lasers intensities exceeding the atomic unit of intensity, $I_a = \frac{\epsilon_0 c}{2} E_a^2 \approx 10^{16}$ W/cm^2, and as high as 10^{22} W/cm^2 can be reached experimentally. Here, c is the speed of light, ϵ_0 is the vacuum permittivity and $E_a = 5.1 \cdot 10^9$ V/cm is the atomic unit of the field strength. In this thesis, we are considering fields with intensities in the range $10^{14} - 10^{15}$ W/cm^2. The considered laser field wavelengths are around 760-800 nm which is the normal wavelength region for pulses obtained from Ti:Sapphire laser systems.

Intense laser fields are qualitatively different from weak fields, regarding the interaction with atoms. Multiphoton processes start to play a role such that the dependence of the observed signals on the field intensity is not linear. Perturbation theory cannot be used anymore to describe the process theoretically. In this chapter, we discuss various non-numerical theoretical approaches to explore the classical and quantum mechanical features of the processes.

Atomic units are used in all equations and calculations, i.e. $\hbar$=1, $4\pi\epsilon_0$=1, e=1, m_e=1 where e is the elementary charge and m_e is the electron mass. In figures below we often use atomic units of time and energy. The conversion to SI units is t_a=24.18 as, $\mathcal{E}_h$=27.21 eV, where t_a is the atomic unit of time and $\mathcal{E}_h$ is the atomic unit of energy, or Hartree energy).

1.1 Time-dependent Schrödinger equation

The time-dependent Schrödinger equation (TDSE) for a system with the Hamiltonian H and the wave function Ψ reads

$$i\frac{\partial|\Psi\rangle}{\partial t} = H|\Psi\rangle. \tag{1.1}$$

Below, TDSE is derived in the length gauge providing an intuitive description of the system. All of the presented numerical results are obtained in length gauge as well.

In this work, we use atomic model potentials, treating the strong field process as the problem of a single electron in a potential $V_0(\mathbf{r})$ created by the core. We note, however, that it is not always the case that the single-electron approximation (SEA) is valid. For instance, it has been shown that multi-electron effects and not just the highest occupied orbitals can play a role in strong-field processes[72,109,130] . The unperturbed Hamiltonian is

$$H_0(t) = -\frac{\nabla^2}{2} + V_0(\mathbf{r}). \tag{1.2}$$

In the presence of the laser electric field, $\mathbf{E}(t)$, and neglecting the magnetic field contribution, the Hamiltonian acquires additional terms. We denote the field-matter interaction term with H', and in atomic units it is

$$H'(t) = \mathbf{r}\cdot\mathbf{E}(t). \tag{1.3}$$

Thus the full time-dependent Hamiltonian, $H = H_0 + H'$, reads

$$H(t) = H_0 + \mathbf{r}\cdot\mathbf{E}(t) = -\frac{\nabla^2}{2} + V_0(\mathbf{r}) + \mathbf{r}\cdot\mathbf{E}(t). \tag{1.4}$$

Finally, the time-dependent Schrödinger equation becomes

$$i\frac{\partial|\Psi(\mathbf{r},t)\rangle}{\partial t} = \left[-\frac{\nabla^2}{2} + V_0(\mathbf{r}) + \mathbf{r}\cdot\mathbf{E}(t)\right]|\Psi(\mathbf{r},t)\rangle. \tag{1.5}$$

The TDSE is solved numerically for a given potential and initial conditions.

1.2 Ionization by laser field

1.2.1 Strong-field tunneling and multiphoton regimes

If an atom or a molecule is subject to an electric field, ionization can take place. Before lasers became a common tool, ionization in constant electric field was for a long time known and discussed. Depending on the field parameters and the ionization channel, different mechanisms of ionization, such as one-photon ionization (i.e. photoelectric effect), quantum-mechanical tunneling (for lower-level electrons and/or weaker electric fields) and above-barrier decay (in case of high-level electrons e.g. Rydberg electrons, and/or strong fields) are described[35] .

With intense lasers, processes such as multiphoton ionization (MPI), tunnel ionization and above threshold ionization (ATI) became the subject of research.

The first step to describe different regimes in strong fields within one general theory was made in the work of Keldysh in 1964[91] , where multiphoton and tunnel regimes were shown to be the limits of the same process. In order to distinguish between the two, the γ parameter of adiabaticity is used, which in atomic units is

$$\gamma = \omega_0/\omega_t = \omega_0\sqrt{2I_p}/E_0, \tag{1.6}$$

where ω_0 and ω_t are the driving laser and the tunneling frequencies, respectively, I_p is the ionization potential, E_0 is the laser field amplitude, which, in atomic units, can be found from the field intensity as

$$E_0\ [\text{a.u.}] \approx \sqrt{\frac{\text{I}\ [\text{W/cm}^2]}{350.9\cdot 10^{14}}}. \tag{1.7}$$

For $\gamma \ll 1$ tunneling ionization takes place. If $\gamma \gg 1$, one speaks of multiphoton ionization. For the more detailed description see, for instance, the reviews by Popov[119] and Protopapas *et al.*[122] or the book by Delone and Krainov[37] .

The difference between the multiphoton and tunneling regimes is schematically shown in Figure 1.1.

Let us first consider the case $\gamma \gg 1$ and assume that the ionization goes from the ground state $|\Psi_g\rangle$ to some continuous final state $|\Psi_f\rangle$. In case of one-photon ionization, the probability to ionize is proportional to the squared matrix element $w_1 \propto E_0^2\,|\langle\Psi_g|\boldsymbol{\epsilon}\mathbf{r}|\Psi_f\rangle|^2 \propto I$, where $\boldsymbol{\epsilon}$ is the polarization vector[55] . Now, multiphoton ionization can go via real eigenstates or virtual intermediate states and correspondingly

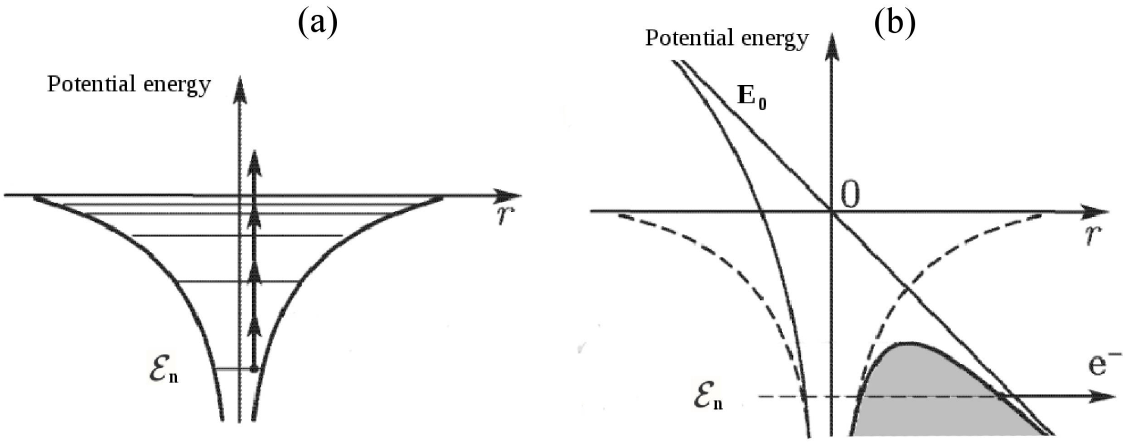

Figure 1.1: Illustration of ionization mechanisms (a) MPI via virtual states, (b) Tunnel ionization. The electric field changes the effective potential for the valence electron causing tunneling. Modified figure from Delone[34] .

occurs as a sequential or as a direct process. Let us say it is K-photon ionization. Analogously to the one-photon case, in the multiphoton regime the ionization probability w_{MPI} is

$$w_{\mathrm{MPI}} \propto I^K, \tag{1.8}$$

If we are interested to find the overall ionization rate, we have to sum over all possible final states as well. In the tunneling regime, $\gamma \ll 1$, the dependence of the ionization probability on the field frequency is negligible and the number of absorbed photons, K_0, is much higher than the minimal number of photons required for ionization, $K_0 \gg I_p/\omega_0$. The Ammosov-Delone-Krainov formula[3] for the tunnel ionization rate by linearly polarized light in the general case of a multi-electron hydrogen-like atom is widely used:

$$w_{ADK} = \sqrt{\frac{3n^{*3}E_0}{\pi Z^3}} \frac{E_0 D^2}{8\pi Z} \exp\left(\frac{2Z^3}{3n^{*3}E_0}\right),\ D = \left(\frac{4eZ^3}{n^{*4E_0}}\right)^{n^*}, \tag{1.9}$$

where $e = 2.718..., n^*$ is the effective principal quantum number of the level, and Z is the core charge. The theory is discussed with remarks in Popov's paper[119] . In Figure 1.2 it is shown schematically that the $\gamma = 1$ corresponds to the switching from the tunneling to the multiphoton regime. From Equation (1.6), at optical frequencies of the driving field the border between the regimes corresponds to an intensity of about 10^{14} W/cm^2. Thus, with the intensities as high as $10^{14} - 10^{15}$ W/cm^2, the main focus of the current work is the tunneling regime of strong field processes.

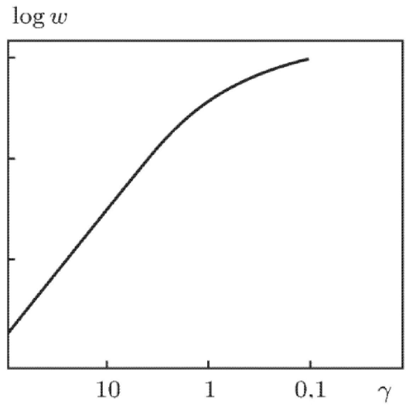

Figure 1.2: Schematic representation of the dependence of the ionization probability $w_{\text{ionization}}$ on the adiabacity parameter γ (from the book of Delone and Krainov[37]).

1.2.2 Above threshold ionization

In the following discussion, we continue to focus on the nonlinear ionization of an atom, in particular above threshold ionization (ATI) in the tunneling regime. We describe the classical features and the quantum approach which are relevant for further investigation of strong field processes.

Classical aspects

Certain features of the ATI spectrum, such as the two typical ATI cutoffs, can be predicted classically. After the ionization has occurred, the electron can be considered as being affected only by the laser field and not by the field of the remaining ion. The motion of the electron obeys the Newton motion equation:

$$\ddot{\mathbf{r}}(t) = -\mathbf{E}(t) \tag{1.10}$$

and thus

$$\dot{\mathbf{r}}(t) = \mathbf{A}(t) - \mathbf{A}(t_0), \tag{1.11}$$

$$\mathbf{r}(t) = \mathbf{A}(t_0)(t_0 - t) + \int_{t_0}^{t} d\tau\, \mathbf{A}(\tau). \tag{1.12}$$

Here, the negative charge of the electron is taken into account and $\mathbf{A}(t)$ is the vector potential, $\mathbf{A}(t) = -\int_{-\infty}^{t} \mathbf{E}(t')dt'$. We have assumed that the electron leaves the core with zero velocity at the moment of ionization, t_0. We assume $\mathbf{A}(-\infty) = \mathbf{A}(\infty) = 0$.

In the field of a continuous wave laser, $\mathbf{E}(t) = \mathbf{E_0}\sin(\omega_0 t)$, Equation (1.10) and

Equation (1.11) can be rewritten as

$$\ddot{\mathbf{r}}(t) = -\mathbf{E_0}\sin(\omega_0 t), \tag{1.13}$$

$$\dot{\mathbf{r}}(t) = \mathbf{v}_{\text{drift}} + \frac{\mathbf{E_0}}{\omega_0}\cos\omega_0 t. \tag{1.14}$$

From Equation (1.12) for the spatial coordinate, one can write

$$\mathbf{r}(t) = \mathbf{r_0} + \mathbf{v}_{\text{drift}} t + \frac{\mathbf{E_0}}{\omega_0^2}\sin\omega_0 t. \tag{1.15}$$

The drift velocity is $\mathbf{v}_{\text{drift}} = -\frac{\mathbf{E_0}}{\omega_0}\cos\omega_0 t_0$ and $\mathbf{r_0} = -\frac{\mathbf{E_0}}{\omega_0^2}\sin\omega_0 t_0 - \mathbf{v}_{\text{drift}} t_0$. We note here that the wavelength λ of the field is long in comparison with the characteristic travel distance of an electron $r_c = E_0/\omega_0^2 \approx 1.5$ nm for $\lambda \approx 800$ nm and $I = 4 \cdot 10^{14}$ W/cm^2.

Since $\mathcal{E}_{\text{kin}} = \dot{\mathbf{r}}^2/2$, one finds the period averaged kinetic energy,

$$\langle \mathcal{E}_{\text{kin}} \rangle = v_{\text{drift}}^2/2 + U_p, \tag{1.16}$$

where U_p is the ponderomotive energy,

$$U_p = \frac{\langle \mathbf{A}^2(t) \rangle}{2} = \frac{E_0^2}{4\omega_0^2}. \tag{1.17}$$

The maximum of the kinetic energy is $2U_p$, which explains the first cutoff of a typical ATI spectrum at $\mathcal{E}_{\text{cutoff}-1}^{ATI} = 2U_p$.

The existence of the second cutoff is due to rescattering of the electrons leaving the core. The rescattering condition is that at some time t_1 the electron returns to the starting point, $\mathbf{r}(t_1) - \mathbf{r}(t_0) = 0$. The electron returns with the momentum $\dot{r}_1 = A(t_1) - A(t_0)$. If elastic rescattering occurs at an angle of 180°, the momentum changes its sign. From that moment to infinity, the electron acquires the momentum of -$A(t_1)$. The final momentum of the electron is

$$\dot{r}_\infty = A(t_0) - 2A(t_1). \tag{1.18}$$

After finding the maximum of this expression with the condition $\mathbf{r}(t_0) - \mathbf{r}(t_1) = 0$ and using Equation (1.15), we find numerically the second cutoff at $\mathcal{E}_{\text{cutoff}-2}^{ATI} = \dot{r}_\infty^2/2 = 10.007U_p$ for $\omega_0 t_0 = 105°$ and $\omega_0 t_1 = 352°$.

Quantum features - strong field approximation

Let us very briefly discuss the formulas derived by Keldysh in the paper mentioned above[91] and the strong field approximation (SFA) developed by Perelomov *et.al*[118] , Faisal[42] and Reiss[128] (for more details see, for example, Beckers's review[11]) since it is relevant to the process of high harmonic generation considered below.

The main idea of the SFA is to calculate the probability amplitude for finding the electron with momentum $\mathbf{p}$ after the ionization from the ground state $|\Psi_g\rangle$. To follow the Keldysh-Faisal-Reiss theory, one should take the orthogonality of eigenstates of the unperturbed Hamiltonian into account and assume no interaction with the ion after the electron leaves the core. To pursue with the derivation, the Dyson equation for the time evolution operator should be used. where K_0 is the minimum number of photons necessary for ionization.

The probability amplitude to detect an electron with the drift momentum $\mathbf{p}$ and corresponding wave function $|\Psi_{\mathbf{p}}\rangle$ after the ionization from the ground state $|\Psi_g\rangle$ is described by the expression[11]

$$M_{\mathbf{p}}^{ATI} \sim \int_{-\infty}^{\infty} dt_1 \int_{-\infty}^{t1} dt_0 \int d^3\mathbf{k} e^{iS_{\mathbf{p}}^{\mathrm{ATI}}(\mathbf{k},t_1,t_0)} m_{\mathbf{p}}(\mathbf{k},t_1,t_0), \tag{1.19}$$

$$m_{\mathbf{p}}(\mathbf{k},t_1,t_0) = \langle \mathbf{p}+\mathbf{A}(t_1)| V_0 |\mathbf{k}+\mathbf{A}(t_1)\rangle \langle \mathbf{k}+\mathbf{A}(t_0)| V_0 |\Psi_g\rangle \tag{1.20}$$

In Equation (1.20) rescattering is taken into account, t_0 denotes the ionization time, t_1 is the time of the recombination and V_0 is the core potential. For the derivation, the so-called Volkov state is taken as the final state. The classical action is

$$S_{\mathbf{p}}^{\mathrm{ATI}}(\mathbf{k},t_1,t_0) = \int_{-\infty}^{t_0} I_p \, d\tau \; - \int_{t_0}^{t_1} d\tau \, \frac{[\mathbf{k}+\mathbf{A}(\tau)]^2}{2} - \int_{t_1}^{\infty} d\tau \, \frac{[\mathbf{p}+\mathbf{A}(\tau)]^2}{2} \tag{1.21}$$

and saddle point approximation requiring $\frac{\partial S_{\mathbf{p}}^{\mathrm{ATI}}(t)}{\partial \xi} = 0$, where $\xi = \{t_0, t_1, \mathbf{k}\}$, leads to the set of equations

$$[\mathbf{k}+\mathbf{A}(t_0)]^2/2 = -I_p, \tag{1.22}$$

$$\mathbf{k}(t_1 - t_0) = -\int_{t_0}^{t_1} d\tau \, \mathbf{A}(\tau), \tag{1.23}$$

$$[\mathbf{k}+\mathbf{A}(t_1)]^2 = [\mathbf{p}+\mathbf{A}(t_1)]^2. \tag{1.24}$$

Equation (1.22) is the energy conservation law at the moment of the ionization, Equation (1.23) indicates that rescattering occurs at the core and Equation (1.24) is the condition for elastic rescattering.

Due to interference of the pulse cycles, the spectrum of above threshold ionization consists of peaks separated by the driving field photon energy. In electric field, the target bound states are shifted by the Stark shift, $\delta\mathcal{E} \propto E_0^2$. The Stark shift is negligible for low-lying states and reaches $E_0^2/(4\omega_0^2)$ for high-lying states. For sufficiently long laser pulses (duration > 10 ps), the emitted photoelectrons are accelerated by the ponderomotive potential giving them the same amount of kinetic energy as is lost in the ionization and compensating the Stark shift[44] . In this case, the peak positions are independent on the field intensity.

$$E_{\text{ATI}} = \begin{cases} K\omega_0 - I_p & \text{long pulse} \\ K'\omega_0 - (I_p + U_p) & \text{short pulse} \end{cases} \qquad K, K' \in \mathbb{N}$$

1.3 High harmonic generation

After the system has been ionized, the emitted electron is accelerated by the oscillating field. There are classically allowed electron trajectories driving it back to the core. The released electron acquires energy while traveling in the continuum. If the electron comes back to the starting point and does not miss the remaining ion, recombination can occur followed by photon emission. The energy of the photon emitted during the recombination is the sum of the kinetic energy of the electron and the ionization potential I_p. Thus, the emitted light can reach the ultraviolet (UV) and the extreme ultraviolet (XUV) range. Since the electric field $\mathbf{E}(t)$ is periodic and one field pulse consists of more than one optical cycles, the spectrum is composed of a set of peaks corresponding to integer multiples of the optical frequency of the driving laser field. Because the laser cycle has an antisymmetric periodicity in respect to $T/2$, where T is the optical period, only odd harmonics are expected for relatively long laser pulses. The process is therefore called high harmonic generation (HHG).

High harmonic generation can occur on different types of targets[46,63,104,110] and gas-phase targets are most commonly used experimentally. In order to enhance the low HHG output, other sources as, for instance, microdroplets[54] and solids[69] have been used. HHG can be used as a source of coherent XUV radiation, for molecular imaging[148] , for creating attosecond pulses and other applications.

We will briefly describe the most common approaches to the theory of high harmonic generation including the classical simple man's model as well as the quantum strong field approximation. Quantum mechanically, if the time-dependent solution of the TDSE is found, the dipole moment of the system, for one electron $\mathbf{d}(t) = \langle \Psi(t)| -\mathbf{r} |\Psi(t)\rangle$, contains the information about the spectrum. Acceleration of the dipole leads to the photon emission. The power spectrum of the second time derivative of the dipole moment, $\ddot{\mathbf{d}}(t)$, is the HHG spectrum. In the section describing the SFA approach, we use the principles and terms developed in the overview of the ionization process presented above.

1.3.1 Simple man's model - electron trajectories.

The simple man's model, developed by Corkum[30] proposes the semiclassical treatment of the high harmonic generation problem and implies that HHG consists of three steps. The first step is the tunnel ionization of the system as the core potential $V_0(\mathbf{r})$ is deformed by the field as described in Section 1.2. The second step is the classical acceleration in the electric field with the Lorentz force. The final step is the recombination of the electron with the remaining ion, which is the inverse process of one-photon photoionization. In the model, only electrons that come back to the core are considered.

HHG spectrum always has a distinct cutoff at higher energies. This feature arises from the fact that the kinetic energy of electrons returning to the core has an upper limit. This limit can be found from the equation of motion and boundary conditions described with the following equation:

$$\mathbf{r}(t_1) = \mathbf{r}(t_0) = 0, \tag{1.25}$$

In Equation (1.25), t_1 is the recombination time for a given ionization time t_0. For each pair t_0, t_1, the kinetic energy $\mathcal{E}_{\text{kin}}(t_1)$ of the electron can be found at the moment when it returns to the core. Figure 1.3 is an example of the time dependence of $\mathcal{E}_{\text{kin}}(t_1)$ in the case of a linearly polarized field $E(t) = E_0 \sin(\omega_0 t)$. Using Equation (1.11) and numerically maximizing the kinetic energy $\mathcal{E}_{\text{kin}}$ with the condition (1.25), we find

$$\mathcal{E}_{\text{kin}}^{\text{max}}(t_1) = \frac{[A(t_1) - A(t_0)]^2}{2} \approx 3.17 U_p. \tag{1.26}$$

The condition of maximum kinetic energy of the returning electron is satisfied at $\omega_0 t_0 = 108°$ and $\omega_0 t_1 = 342°$. This means that the energy of the emitted photon is limited by $\mathcal{E}_{\text{cutoff}}^{\text{HHG}} = I_p + 3.17 U_p$[30] .

Another observation one can make from Figure 1.3 is the existence of two nearly symmetric arms on the left and right hand sides of the maximum. This fact corresponds to the so called short and long trajectories of the electron in the continuum.

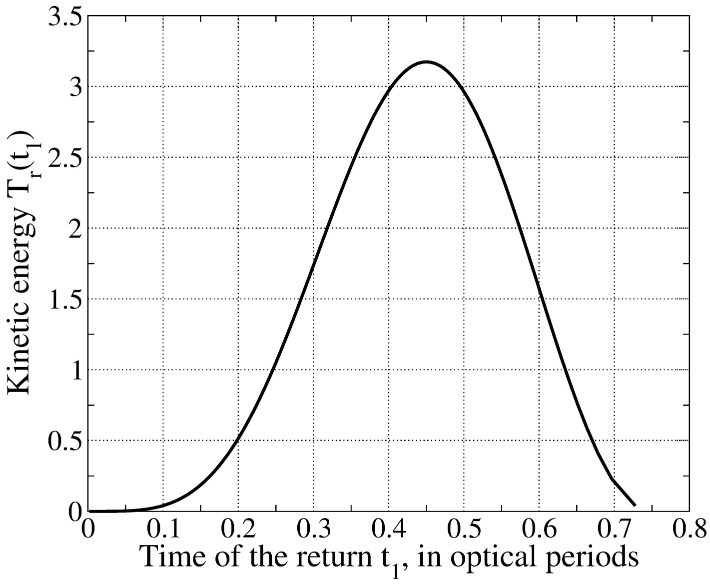

Figure 1.3: Kinetic energy of the returning electron as a function of the recombination time. The field is linearly polarized and satisfies $E(t) = E_0 \sin(\omega_0 t)$. The field intensity is $I = 4 \cdot 10^4$ W/cm^2, $\omega_0 = 0.057$ a.u. The shown returning time is within a half cycle.

Experimentally, the presence of the nearly classical trajectories has been confirmed by the measurement of the attosecond chirp[106] . We will discuss these trajectories in more detail below. The three-step sequence is repeated in every half cycle of the laser field.

1.3.2 Lewenstein model and saddle-point approximation

M. Lewenstein used the SFA method to describe high harmonic generation. In the Lewenstein model[103] , the so called saddle-point approximation is used to solve the time-dependent Schrödinger equation (TDSE) for a single electron in the field of the ionic core. Again, only the ground state, $|\Psi_g(t)\rangle = \mathrm{e}^{iI_pt}\,|\Psi_g\rangle$, and continuum states $|\mathbf{v}\rangle$ are considered contributing to the outcome. The depletion of the ground state is neglected. The continuum states are so called Volkov states, i.e. plane waves with momenta depending on time as they do in classical mechanics. Lewenstein's wave function $|\Psi_L\rangle$ takes the form

$$|\Psi_L\rangle = \mathrm{e}^{iI_pt}\left(a(t)\,|\Psi_g(\mathbf{r})\rangle + \int d^3\mathbf{v} b(\mathbf{v},t)\,|\mathbf{v}\rangle\right), \tag{1.27}$$

where $a(t) \simeq 1$ and $b(\mathbf{v},t)$ are the ground and continuum states amplitudes, respectively.

Within SFA, continuum-continuum transitions are neglected as well. Again, as in the Section 1.2, the influence of the Coulomb potential on the electron moving far from the core is considered insignificant due to the high field intensity. We note that the Lewenstein model is only valid for the harmonics with high orders q and is not in general correct for $\mathrm{q}\omega_0 < \mathrm{I_p}$.

The matrix element of photon emission with frequency ω in the HHG process is[11]

$$M^{\mathrm{HHG}}(\omega) \sim \int_{-\infty}^{\infty} dt_1 \int_{-\infty}^{t_1} dt_0 \int d^3\,\mathbf{k}\; d_{\boldsymbol{\epsilon}}(\mathbf{k}+\mathbf{A}(t_1)) d^*_{\mathbf{E}}(\mathbf{k}+\mathbf{A}(t_0)) e^{iS_\omega(\mathbf{k},t_1,t_0)}, \quad (1.28)$$

$$d_{\boldsymbol{\xi}}(\mathbf{k}+\mathbf{A}(t)) = \langle \Psi_g | \, \mathbf{r}\cdot\boldsymbol{\xi} \, | \mathbf{k}+\mathbf{A}(t) \rangle \,, \; \boldsymbol{\xi} = \{\mathbf{E}, \boldsymbol{\epsilon}\}. \quad (1.29)$$

In Equation (1.29), $\boldsymbol{\epsilon}$ is the polarization of the harmonic with the frequency ω and $S_\omega(\mathbf{k}, t_1, t_0)$ is the action and plays the role of an additional phase of motion in the field.

The action in case of HHG is

$$S^{HHG}_\omega(\mathbf{k}, t_1, t_0) = \int_{-\infty}^{t_0} I_p\, d\tau \; - \int_{t_0}^{t_1} d\tau\, \frac{[\mathbf{k}+\mathbf{A}(\tau)]^2}{2} - \int_{t_1}^{\infty} d\tau\, (-I_p + \omega). \quad (1.30)$$

In Equation (1.30), I_p is the ionization potential. The action in this case has an intuitively clear structure representing the three steps of high harmonic generation: ionization at t_0, acceleration until the time of return t_1 and emission of the photon. The last term of Equation (1.30) is different if the electron does not recombine, but elastically scatters as in case of ATI, see Equation (1.21).

The integral in Equation (1.28) can be approximated using the saddle-point method. The first two equations of the system remain the same as in Equation (1.22) and Equation (1.23), but the last condition changes and expresses now the energy conservation law at the moment of recombination:

$$[\mathbf{k}+\mathbf{A}(t_0)]^2/2 = -I_p, \quad (1.31)$$

$$\mathbf{k}(t_1 - t_0) = -\int_{t_0}^{t_1} d\tau\, \mathbf{A}(\tau), \quad (1.32)$$

$$[\mathbf{k}+\mathbf{A}(t_1)]^2/2 = \omega - I_p. \quad (1.33)$$

According to the Lewenstein model, the cutoff energy gets a correction and becomes $E_{\mathrm{cutoff}} = 3.17U_p + 1.32I_p$.

Very few efforts were made to apply SFA to a system with more than one bound state. For above threshold ionization, Kanno *et al.*[90] considered examples of H and H_2^+ to investigate excited states dynamics by applying S-matrix theory to propagate a wave packet composed of bound electronic states. Batebi and Mohebbi[10] in 2011 derived the HHG emission probability for a two-level system. The probability amplitude in their work is described as a sum of contributions from bound-continuum and bound-bound transition dipoles which are plotted separately for HHG in neon. In the article, it is shown, that the excited state is mostly responsible for the ionization, and that transition from the excited state to the ground state mainly contributes to the HHG efficiency. The authors show that the coherent superposition of the two bound states leads to HHG spectra having distinct plateaus with different conversion efficiencies.

In relation to the topic of this Thesis, in 2013, Strelkov *et al.*[138] applied the SFA approach to a system with an autoionizing state. The idea of their work is the following: the wave function, $|\Psi_S\rangle$, has an additional term related to the quasi-bound excited state $|\Psi_{\mathrm{AI}}(\mathbf{r})\rangle$ with the energy $\mathcal{E}_{\mathrm{res}}$, localized around the origin and decaying with the relatively long lifetime $1/\Gamma$.

$$|\Psi_S(\mathbf{r},t)\rangle = \mathrm{e}^{iI_pt}\left(a(t)\,|\Psi_g(\mathbf{r})\rangle + \int d^3\mathbf{v}b(\mathbf{v},t)\,|\mathbf{v}\rangle\right) + c(t)\,|\Psi_{\mathrm{AI}}(\mathbf{r},t)\rangle\,, \tag{1.34}$$

$$|\Psi_{\mathrm{AI}}(\mathbf{r},t)\rangle = |\Psi_{\mathrm{AI}}(\mathbf{r})\rangle\,\mathrm{e}^{-i(\mathcal{E}_{\mathrm{res}}-i\Gamma/2)t}, \tag{1.35}$$

where $|\psi_{\mathrm{AI}}(\mathbf{r})\rangle$ is a stationary solution in absence of the configuration interaction. With that, the dipole moment gets an additional term in comparison with Lewenstein's model due to transitions between the quasi-bound excited and the ground states, oscillating with the phase $(\mathcal{E}_{\mathrm{res}} - i\Gamma/2 + I_p)t$. As a result, the total dipole moment turns out to have the following dependence:

$$M_S^{\mathrm{HHG}}(\omega) \sim 1 + Q\frac{\Gamma/2}{\Delta\omega + i\Gamma/2}, \tag{1.36}$$

$$\tag{1.37}$$

where Q is a coefficient depending on the excited state width and position as well as on the transition dipole moments for ground-excited state, excited state-continuum and continuum-ground state transitions. The square of the absolute value of the total dipole moment exhibits a Fano-like profile shape around the resonance. The results of the paper show reasonable agreement with experiment and numerical simulation[76] .

1.3.3 High harmonic generation in a medium

In real systems, not only single atom, but also medium effects come into play. Strictly speaking, in this case, a coupled system of Schrödinger and Maxwell equations has to be solved. Assuming cylindrical symmetry around the direction of the propagation z, in cylindrical coordinates $\{r, z\}$, both the harmonic and the fundamental electric (denoted by the index $i = \{f, h\}$) field satisfy

$$\nabla^2 E_i - \frac{1}{c^2}\frac{\partial E_i(r,z,t)}{\partial t^2} = G_i(r,z,t), \tag{1.38}$$

with the speed of light, c, and the source term $G_i(r,z,t)$. The standard further procedure[121] is to switch to the moving frame, $z' = z, t' = t - z/c$ and, assuming $\frac{\partial^2 E_i}{\partial z'^2} \approx 0$, after performing the Fourier transform with respect to t',

$$\nabla_\perp^2 \tilde{E}_i(r,z',\omega) - \frac{2i\omega}{c}\frac{\partial \tilde{E}_i(r,z',\omega)}{\partial z'} = \tilde{G}_i(r,z',\omega). \tag{1.39}$$

Redistribution of free electrons is the main contribution to the source term $G_f(r,z',t')$:

$$G_f(r,z',t') = \frac{\omega_p(r,z',t')^2}{c^2} E_f(r,z',t'), \tag{1.40}$$

$$\omega_p = \sqrt{\epsilon^2 n_e(r,z',t')/\epsilon_0 m_e}, \tag{1.41}$$

with the plasma frequency ω_p and electron density n_e. The electron density can be obtained from the ionization rate or numerically.

For the harmonic field,

$$G_h(r,z',t') = \mu_0 \frac{\partial^2 P_{nl}(r,z',t)}{\partial t^2}, \tag{1.42}$$

where P_{nl} is the nonlinear polarization and is proportional to the dipole moment calculated from SFA or numerically, $P_{nl}(r,z',t) = (n_0 - n_e(r,z',t))d(r,z',t)$. The final harmonic spectrum is obtained after integrating the harmonic field over the spatial coordinates.

1.3.4 Harmonic phase

Each trajectory of the returning electron has a phase factor which also depends on the position of the target on the axis of the field propagation. The dependence of the harmonics phase on the driving laser intensity and frequency comes into play when we are discussing macroscopic propagation. For better efficiency, it is desirable that harmonics are generated coherently depending on the spatial position. Let us say, the light is propagating along z-axis. The phase dependence on macroscopic parameters as the fundamental light is propagating through the focus is given by the following expression[156] :

$$\Phi(z) = (1 + \Delta n_p(\omega) + \Delta n_g(\omega))kz - \tan^{-1}(z/z_R), \quad (1.43)$$

where Δn_p and Δn_g stand for the variations of the refractive indexes due to the laser generated plasma and neutral target gas. z_R is the Rayleigh length (the distance along the z-axis from the waist of the beam to the place where the area of the cross section is doubled). The last term is called the Gouy phase which is the phase shift that the light acquires when passing the focus. For the harmonics, the dependence of the phases can be expressed as

$$\Phi_q(z) = (1 + \Delta n_p(\omega_q) + \Delta n_g(\omega_q))kz - \tan^{-1}\left(z/z_{R_q}\right) + \frac{|\alpha_q| I}{1 + (z/z_r)^2}, \quad (1.44)$$

where I is the intensity of the beam and α_q is the coefficient describing the linear dependence on the intensity[8] . The two trajectories will acquire different phases, and the ratio $\frac{\alpha_q^{long}}{\alpha_q^{short}}$ is about one order of magnitude. One can draw the conclusion that due to the worse coherence long trajectories will not contribute to the final HHG spectrum after propagation through a medium. In general, it is important that the phase mismatch is minimized in order to efficiently produce harmonics in the spectrum plateau.

Chapter 2

Methodological aspects of numerical simulation

In this thesis, the majority of the results are obtained using numerical simulations, and we dedicate this chapter to describing the calculation details. We solve the 1D and 2D time-dependent Schrödinger equation in the presence of a laser field

$$i\frac{\partial|\Psi(\mathbf{r},t)\rangle}{\partial t} = \left[-\frac{\nabla^2}{2} + V_0(\mathbf{r}) + \mathbf{r}\cdot\mathbf{E}(t)\right]|\Psi(\mathbf{r},t)\rangle, \tag{2.1}$$

propagating the initial ground-state wave function in time. Below, we talk about such features of the calculation as propagation strategies, grid and step sizes, assumed electric field temporal dependence, and the calculation of the harmonic spectrum. All SEA calculations are performed in Fortran.

2.1 Ground state and time propagation

The TDSE is solved by means of the split-operator technique (SOM)[45,51] . Using SOM requires that the system Hamiltonian can be written in the form

$$H = T + V, \tag{2.2}$$

where V and T are the potential and kinetic energy operators, respectively. The time evolution of the wave function after a small time step Δt is described with the exponential propagation operator:

$$|\Psi(\mathbf{r},t+\Delta t)\rangle = \exp^{(-iH\Delta t)}|\Psi(\mathbf{r},t)\rangle\,. \tag{2.3}$$

It has been suggested that the exponential operator from Equation (2.3) can be split to two parts containing V and T, which then can be applied sequentially to the wave function in coordinate and momentum space, respectively. To do the forward and inverse Fourier transform, we use the standard FFTW subroutine[155] . We apply the operators at each time step to obtain the evolution of the ground state Ψ_g:

$$|\Psi(t+\Delta t)\rangle \approx \mathrm{e}^{-iT\Delta t/2}\mathrm{e}^{-iV\Delta t}\mathrm{e}^{-iT\Delta t/2}\,|\Psi(t)\rangle\,, \tag{2.4}$$

$$|\Psi(t=0)\rangle = |\Psi_g\rangle\,. \tag{2.5}$$

The numerical error[139] of the method is of the order $\mathcal{O}(\Delta t^3)$, and the requirement on the grids is $\Delta t \ll \Delta x^2$.

In order to obtain the ground state, we start with a random initial state and perform imaginary-time propagation[96] replacing $\Delta t \to -i\Delta\tau$. We propagate according to Equation (2.4) and with the field-free Hamiltonian H_0, Equation (1.2), so that all possible higher-energy states die out exponentially with the time. In this process, we apply normalization after every time step since the imaginary-time propagator $\mathrm{e}^{-H_0\Delta\tau}$ is not unitary. If we propagate for long enough, the process converges. After one step, the squared norm is

$$N = \mathrm{e}^{-2\mathcal{E}_g\Delta\tau}, \tag{2.6}$$

and the ground state energy can be found from Equation (2.6):

$$\mathcal{E}_g = -(\ln N)/(2\Delta\tau) \tag{2.7}$$

We note that an excited state with known principal quantum number can also be found, for example, by field-free propagation of an arbitrary function and projecting out one by one the lower lying states.

We propagate the system in time for two more optical cycles after the pulse is over to make sure that we account for the returning electron.

2.2 Spatial and temporal grids and step size

In the calculation, the key idea when choosing an appropriate grid is to account for most of the spreading electron wave packet. For HHG, the semiclassical treatment of free electrons gives an estimate how far an electron can travel after the ionization and before coming back to the core as a function of the field amplitude E_0 and frequency

ω_0:

$$R_{\max} = 2r_c = 2E_0/\omega_0^2. \tag{2.8}$$

The derivation can be found in Section 1.2. We use a spatial grid as wide as $2L_x$ with $L_x = 280$ a.u. $\approx 5R_{\max}$ along the field polarization. In 2D, the grid size, L_y, was chosen to be the same as L_x (280 a.u.) for circularly polarized pulses, and reduced accordingly with the decrease of polarization degree to be as small as $L_y^{\min}$=70 a.u. if the pulse was polarized along the x-axis.

Despite the fact that the grid is chosen to be large enough to take into account all of the electrons participating in HHG, one should still apply absorbing boundaries at the edge of the grid. We chose a $\sin^2$ absorbing mask with a size equal to 10-15% of the grid length. The boundary is necessary to avoid the electrons leaving on one side to appear on the opposite side of the finite grid, or from being reflected from the boundary.

For ATI calculations, however, not only the returning, but all of the electrons have to be considered, which means a larger spatial grid especially if the intention is to also consider the rescattered electrons with energies up to $10U_p$ (the second ATI cutoff). We write for the minimal grid side in one direction from zero:

$$L_x^{\mathrm{ATI}} = (\text{time of propagation}) \times \upsilon_{\max}, \tag{2.9}$$

and $\upsilon_{\max}$ is the velocity corresponding to the maximal desirable electron energy to be taken into account. For example, if we wish to consider both $2U_p$ and $10U_p$ cutoffs of the ATI spectrum, we must require $v_{\max}^2/2 = QU_p \geq 10U_p$.

For all of the presented results, the spatial step is 0.12-0.25 a.u. and the calculations have been tested for convergence.

As far as the time step is concerned, we chose it such that the evolution operator $\mathrm{e}^{-iE_0\Delta t} \approx 1$ for the chosen field amplitude. We also meet the condition $\Delta t \ll \Delta x^2$, which means that at such small time step the corresponding frequency is sufficiently large to cover the energies represented on the grid, in other words, $\frac{2\pi}{(\Delta t)} \gg \frac{k_{\max}^2}{2} = \frac{\pi^2}{2\Delta x^2}$
.

2.3 Field

The laser field in experiments takes the form of a pulse with finite duration. In all calculations discussed below the field has the form:

$$E(t) = E_0 \sin(\omega_0 t + \phi_0) f(t). \tag{2.10}$$

Here $f(t)$ is the envelope which has trapezoidal, sinusoidal or Gaussian shape, ϕ_0 is the phase shift. The choice of the specific shape of the envelope depends on the experiment that the theory attempts to reproduce. The lengths of the ramps, n_r, and the plateau, n_p, of the trapezoidal envelope we denote in the way $n_r + n_p + n_r$. Alternatively, the ramps of the trapezoidal envelope can be chosen not linear, but $\sin^2$ shape to simulate smoother switch-on and switch-off and avoid undesirable noise. Physical pulses are such that the vector potential is zero at the end and $\int E(t)dt = 0$.

2.4 High harmonic generation spectrum

After the wave function is found as a function of time and coordinate, the dipole acceleration can be calculated as:

$$\mathbf{a}(t) = \langle \Psi(t) | \nabla V_0(\mathbf{r}) + \mathbf{E}(t) | \Psi(t) \rangle , \tag{2.11}$$

or, alternatively as the second time derivative of the dipole moment,

$$\mathbf{a}(t) = -\frac{\partial^2 \langle \Psi(\mathbf{r},t) | \mathbf{r} | \Psi(\mathbf{r},t) \rangle}{\partial t^2}. \tag{2.12}$$

The emitted intensity as a function of energy - the harmonic spectrum - can be found by Fourier transforming the dipole acceleration:

$$S(\omega) = \left| \int dt \ \mathbf{a}(t) e^{i\omega t} \right|^2 . \tag{2.13}$$

2.5 Time-frequency analysis

It is possible to extract the time-frequency dependence of the final emission from the dipole acceleration. To do so, we employ the Gabor transform,[23,61] $G(\omega, t)$. The modulus squared of this function is the time-frequency distribution of the harmonic intensity.

$$|G(\omega,t)|^2 = \left| \int d\tau \; \mathbf{a}(\tau) e^{i\omega\tau} e^{-(t-\tau)^2/2\sigma^2} \right|^2 . \tag{2.14}$$

In the following, we use the parameter $\sigma = 1/(3\omega_0)$. The phase of the Gabor function, $G(\omega,t)$ gives insight into the time-frequency aspects of phase matching.

2.6 Above threshold ionization

Since at each instant in time, the wave function defines the electron density in momentum space, one can obtain the final free electron distribution as a function of momenta, i.e. the above threshold ionization spectra, by neglecting the Coulomb potential effect on the continuum states and performing the Fourier transform after removing the bound states from the total wave function.

To do so, after propagating for two cycles after the laser pulse is over, to make sure that ATI electrons are far away from the core, the inner region with the radius 15-20 a.u. is removed from the integration region. The ATI wave function, $|\Psi_{\mathrm{ATI}}\rangle$, is set to zero around the core, preserved at large distances and smoothed with $\sin^2$ ramps in between, with a size of a few atomic units. Let us $\Psi^p_{\mathrm{ATI}}(p)$ be the electron ATI wave function in momentum representation. The ATI spectrum as a function of the electron momentum p is then

$$A(p) = |\Psi^p_{\mathrm{ATI}}(p)|^2. \tag{2.15}$$

From the fact that electron energy is $E = p^2/2$ and $S(E)dE = A(p)dp$ we get

$$S_{\mathrm{ATI}}(E) = (A(\sqrt{2E}) + A(-\sqrt{2E}))/\sqrt{2E}. \tag{2.16}$$

Chapter 3

High harmonic generation in the presence of a shape resonance

3.1 Introduction

In this chapter, we consider contribution of an excited electronic state with finite lifetime to high-order harmonic generation. For a single valence electron we model such a state with a potential supporting a barrier. The electron can tunnel out from the excited state through the barrier leaving the core unchanged. The lifetime of the electron excited state is dependent on the barrier shape. Below, we use the terms "resonant", "autoionizing" and "metastable" as synonyms to refer to this specific type of excited state.

The efficiency of HHG is notoriously low. In the three-step model, HHG is due to recombination into the valence shell, and recombination is the inverse process of photoionization. Since resonant states play an important role in photoionization, the presence of a resonant excited state is likely to enhance HHG emission as well. Thus, systems known for having a resonance in their photoionization cross section can be considered as potential candidates for efficient high-order harmonic generation.

This chapter is based on our theoretical work published previously[145] . We analyze the effect of a shape resonance on high harmonic generation and calculate harmonic spectra in one- and two-dimensional systems and investigate its properties using the time-frequency analysis of the harmonic intensity and phase. We discuss the mechanism of resonance formation in the HHG process. We model HHG in a medium and find that the signature of the resonance remains significant. Comparison with an experiment of high harmonic generation in a manganese plasma[68] allows us to prove the validity of the theoretical model. We investigate the effect of few-cycle pulses in the situation of the manganese plasma.

3.2 Previous work

Resonant peaks in the photoionization cross section have been intensively investigated in the past. The studies included autoionization resonances[43,124] , shape resonances[92] , and giant resonances[4] . The relation of HHG and photoionization spectra was shown in the paper by Shiner[135] . In the paper, it was demonstrated that HHG in xenon shows features of multi-electron effects, namely, a giant resonance in Xe.

Some papers in the past were dedicated to the multiphoton resonances in high-order harmonic generation[48,59,140] . These studies discussed the resonant excitation of bound states, i.e. a different physical situation, also responsible for the strong enhancement of groups of peaks in above threshold ionization spectra[117] . In contrast, below we discuss resonances in the meaning of metastable states embedded in the electronic continuum of the target system.

Resonant enhancement of individual harmonics has been already observed experimentally with the use of many-cycle laser pulses interacting with plasma plumes, see the review by Ganeev[63] and references therein. Resonant enhancement by few-cycle pulses was investigated later in collaboration with Rashid Ganeev and is discussed below in this chapter. It then has been suggested that a range of harmonics in the HHG spectrum can be enhanced in the presence of a metastable excited state. Some authors have argued that the enhancement can be due to the population of metastable states via a resonant excitation mechanism[85,113,114] .

Another theoretical model explaining the resonant HHG is the four-step model suggested by Strelkov[137] . Strelkov used a potential with a barrier to mimic the autoionizing states of the ions relevant for the experimentally observed HHG in plasma[63] . According to the model, the last step of the usual HHG process (radiative transition to the ground state) is split into two steps: the returning electron is trapped by the target into the resonance and then it relaxes to the ground state emitting the XUV photon. Results of Strelkov's theoretical analysis show quantitative agreement with the experiment. The calculated and measured resonant peak enhancement practically coincide. Still, it remains to be clarified whether the four-step process really takes place in the time-evolution obtained from the TDSE. We verify the four-step the model suggested by Strelkov using the time-frequency analysis of the emission and by varying the ellipticity of the driving field.

Shape resonances may also be important for understanding molecular HHG spectra, e.g. from N_2[100] . Some researchers used time-dependent density functional theory (TDDFT) to model the molecular or atomic potential[26] . In our work we simplify the task by using the single-active electron approximation with a potential exhibiting a shape resonance due to a potential barrier and reproducing the ground state energy, the resonance energy and its lifetime.

The phase-matching aspects of this emission mechanism were discussed in papers by Kulagin and Milošević[98,114] . A qualitative model to simulate the results of HHG propagation in a medium was proposed by Le, Morishita and others[101,116] . We investigate both the single-atom response and phase-matching aspects[58] . We apply the time-frequency analysis to the harmonic phase and use the intensity-averaging approach to model HHG propagation effects.

3.3 Methods

To study the problem of resonant HHG, we numerically solve the TDSE, Equation (1.5), in the presence of a laser field as described in Chapter 2. Below, we describe specific parameters involved in the calculation of HHG spectra such as potentials parameters, electric field pulse shape and intensity and media modeling strategy. We investigate the HHG spectra in 1D from two potentials, $V_0^1(x)$ and $V_0^2(x)$ which have different lifetimes of the excited state, and x is the only spacial coordinate. In one dimension, the electron cannot miss the core on its way back in the oscillating field. We test the theoretical 4-step model[137] in 2D with the potential $V_0^{2\mathrm{D}}(\mathbf{r})$ to see whether the resonance emission is associated with the recollision.

3.3.1 Potential shape

The key difference compared to the usual way to model high-order harmonic generation is the shape of the potential $V_0(r)$ of the unperturbed system. We use a model potential possessing a potential barrier exponentially decaying with the distance from the core. We choose the following shape:

$$\begin{aligned} V_0(r) &= -\alpha_1 + \frac{\alpha_1}{1+e^{\frac{r+\alpha_2}{\alpha_3}}} + \frac{\alpha_1}{1+e^{\frac{-r+\alpha_2}{\alpha_3}}} \\ &+ \frac{\alpha_4}{(\alpha_5+r^2)(1+e^{\frac{r+\alpha_2}{\alpha_3}})} + \frac{\alpha_4}{(\alpha_5+r^2)(1+e^{\frac{-r+\alpha_2}{\alpha_3}})}. \end{aligned} \tag{3.1}$$

The potential barrier leads to the existence of a shape resonance, i.e. a metastable state corresponding to an electron trapped in the interior region with a finite lifetime. A potential described with Equation (3.1) has the following properties relevant in high-order harmonic generation: the ground state energy, $\mathcal{E}_\mathrm{g}$, defining the cutoff, and the

Table 3.1: 1D: potential parameters

param. potential	α_1	α_2	α_3	α_4	α_5	$\mathcal{E}_{\mathrm{g}}$	$\mathcal{E}_{\mathrm{res}}$	Γ
V_0^1	1.32	1.27	0.23	9.5	1.4	-0.54 a.u.	0.95 a.u.	0.030 a.u.
V_0^2	1.5	1.27	0.23	14	1.4	-0.58 a.u.	1.2 a.u.	0.007 a.u.

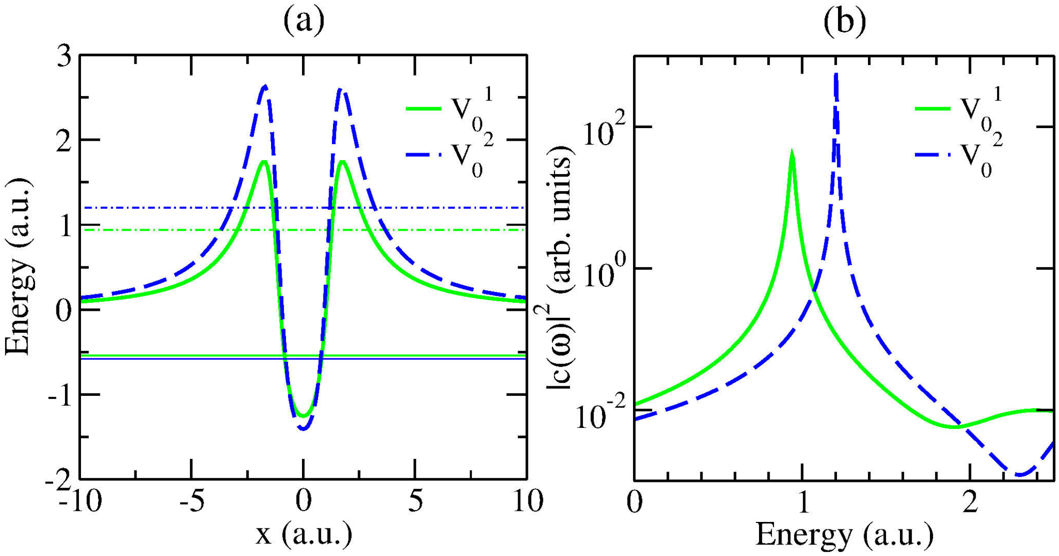

Figure 3.1: (a) The two 1D potentials discussed in this chapter. Parameters are listed in the Table 3.1. The ground-state energies are shown with solid horizontal lines. Shape resonances are shown with dot-dashed horizontal lines. (b) Modulus squared of the Fourier-transformed autocorrelation function showing the resonances of potentials V_0^1 and V_0^2.

resonance energy, $\mathcal{E}_{\mathrm{res}}$, and its lifetime T_{decay}, defining the position and the magnitude of the resonant emission. The inverse of the lifetime is the excited state width, Γ. By varying the height and the width of the potential barrier, i.e. the parameters α_4 and α_5, we can change the excited state energy and its width.

For the 1D case the potential parameters of resonance as well as the states energies are listed in Table 3.1 for the two potentials used in the calculations. Figure 3.1(a) shows the shapes of the 1D potentials V_0^1 and V_0^2. In the 2D case, the potential is rotationally symmetric in the xy-plane, and the electric field vector also lies in the xy-plane. Table 3.2 summarizes the parameters of the potential and the states.

We obtain the resonance energy numerically by inspection of the modulus squared of the Fourier-transformed autocorrelation function $c(t)$, showing the decay of the

Table 3.2: 2D: potential parameters

param. potential	α_1	α_2	α_3	α_4	α_5	$\mathcal{E}_{\mathrm{g}}$	$\mathcal{E}_{\mathrm{res}}$	Γ
V_0^{2D}	1.4	1.5	0.23	6	1.2	-0.38 a.u.	0.66 a.u.	0.057 a.u.

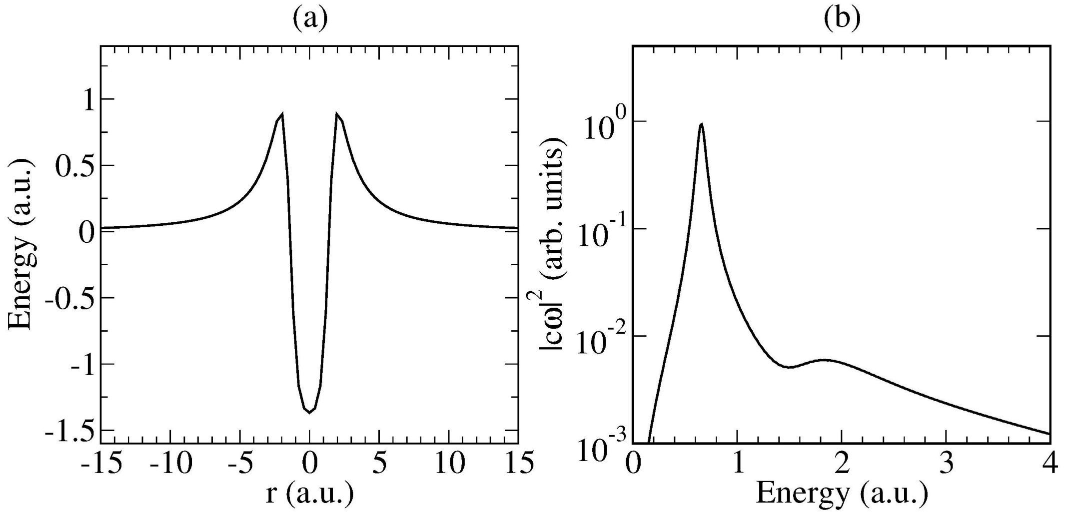

Figure 3.2: (a) The 2D-case potential energy as a function of distance from the core. Parameters are listed in the Table 3.2. (b) Modulus squared of the Fourier-transformed autocorrelation functions showing the resonances of potential V_0^{2D}.

metastable state as a function of time:

$$c(t) = \langle \Phi_0 | \Phi(t) \rangle, \tag{3.2}$$

where $|\Phi(t)\rangle$ is the result of field-free propagation of an arbitrary function $|\Phi_0\rangle$ that overlaps with the resonant state, but is orthogonal to the ground state Ψ_0 such that we do not see the contribution of the ground state in the resulting spectrum $|c(\omega)|^2$. We choose $\Phi_0(\mathbf{r}) = \Phi_G(\mathbf{r}) - \langle \Psi_0 | \Phi_G \rangle \Psi_0(\mathbf{r})$ with a Gaussian wave packet $\Phi_G(\mathbf{r}) = \exp(-(r - 0.9)^2)$. The Fourier transform of the autocorrelation function Equation (3.2) clearly shows the position of the resonance in the 1D case (see Figure 3.1(b)) and in the 2D case (Figure 3.2(b)). The lifetimes are obtained from the widths of the resonant peaks by fitting to the Breit-Wigner formula[99]

$$\sigma(\omega) = \frac{p}{(\omega - \mathcal{E}_{\mathrm{res}})^2 + \Gamma^2/4}, \tag{3.3}$$

where σ describes the shape of the peak as a function of photon frequency ω, p is a freely varied parameter, Γ and $\mathcal{E}_{\mathrm{res}}$ are the resonant state width and position to be fitted. The widths are listed in the Table 3.1 and Table 3.2.

3.3.2 Intensity averaging

Here, we follow the intensity averaging method discussed in our paper[145] . In a real HHG experiment, the macroscopic propagation of harmonics emitted by different atoms of a medium plays an important role[58] . Being distributed in space, different atoms are exposed to different intensities of the laser field. We simulate the phase matching by coherent summation over intensities in an appropriate range ΔI[86,101] in order to study the effect on the HHG spectrum and time-frequency distribution. We calculate the total effective dipole acceleration generated by N uniformly distributed intensities in the range ΔI according to

$$\mathbf{a}_{\text{eff}}(t) = \sum_{i=1}^{N} \mathbf{a}_{I_i}/N. \tag{3.4}$$

It was shown that the results from the intensity-averaging procedure agree with the results from the more complicated macroscopic propagation for the frequently used experimental configuration with the gas jet after the focus[86] . This configuration favors the selection of the short trajectories[5] .

3.3.3 Field parameters

In 1D, calculations are performed for 800 nm wavelength and frequency $\omega_0 = 0.057$ a.u. For the single atom calculations, the field intensity is 4×10^{14} W/cm^2. We employ a “short” and a “long” laser pulse with trapezoidal envelopes. The short pulse has a 1+1+1 shape, *i.e.* one optical cycle switch-on and switch-off times and a one-cycle plateau. The long pulse has a 3.5+2+3.5 shape. These pulses and their parameters are shown in Figure 3.3.

Because the purpose of carrying out the 2D calculations is to test the mechanism rather than to simulate a real system, we use laser field with the frequency ω_0=0.08 a.u. in order to shorten the calculation. The pulse has a trapezoidal envelope and rather short duration, consisting of 1+3+1 optical cycles. As an example, for ellipticity ϵ=0.2 a.u., the x and y components of the 2D field are shown in the Figure 3.4 as a function of time.

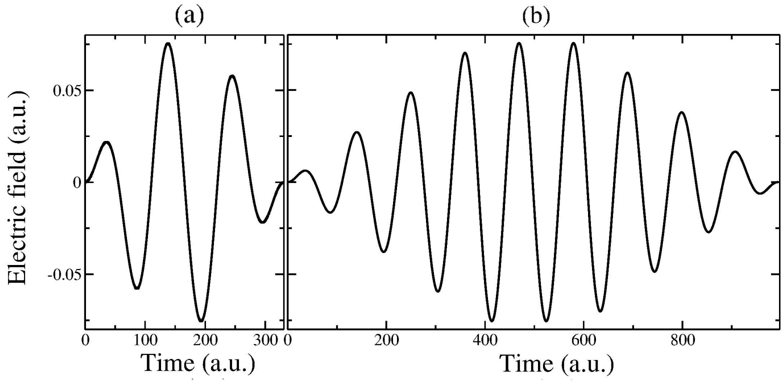

Figure 3.3: Electric field used for the 1D calculations (a) The short pulse with a 1+1+1 envelope. (b) The long pulse with a 3.5+2+3.5 envelope.

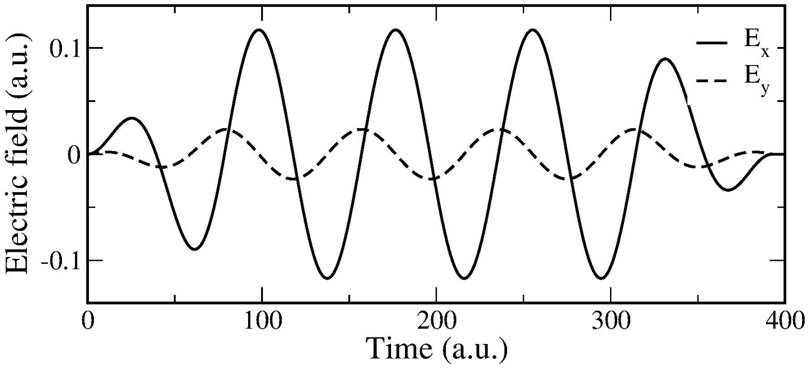

Figure 3.4: Electric field components E_x and E_y used for the 2D calculation. In this example, the ellipticity is ϵ=0.2 a.u.

3.4 High harmonic generation and above threshold ionization by a potential with a shape resonance

3.4.1 Single-atom response in one dimension

First, we address the question whether the HHG spectrum obtained from the numerical solution the TDSE for a single atom shows any signature of the shape resonances in principle. The exact mechanism of resonant HHG will be investigated later by inspection of the spectrum resolved on the time scale.

In Figure 3.5 the HHG spectra are shown for the two different pulse lengths. The cutoffs are in agreement with the semiclassical approximation $I_p + 3.2U_p$ (see Chapter 1). As it happens normally for long pulses with trapezoidal envelope, the harmonic peaks become sharper with increasing pulse length since the full width at

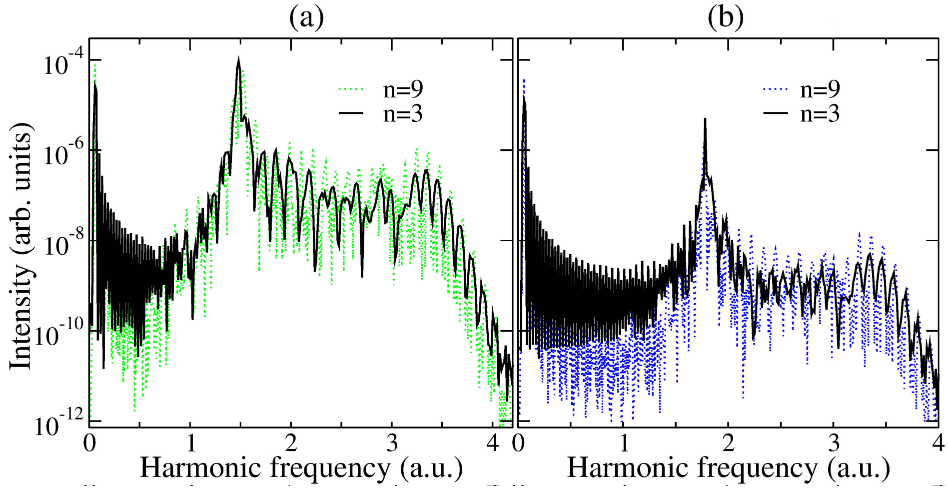

Figure 3.5: HHG spectra calculated with different pulse lengths for the potentials shown in Figure 3.1(a). n is the overall number of optical cycles. (a) HHG spectrum for V_0^1 (solid green curve in Figure 3.1a). (b) HHG spectrum for V_0^2 (dashed blue curve in Figure 3.1a).

half maximum (FWHM) of the pulse in the energy domain reduces. Despite certain differences, for both short and long pulses the spectrum exhibits a strong peak at the harmonic frequency corresponding to the difference between the resonance energy and the ground-state energy, which we denote as Δ.

The potential barrier practically makes it impossible for slow electrons to return to the bound-state region. As a consequence, at energies below the resonance peak, harmonic emission appears to be strongly suppressed. The enhancement of the harmonic peak around Δ is two to three orders of magnitude relative to other plateau harmonic peaks height. Our calculation shows that the resonance is observed at all pulse durations, thus indicating that the resonant emission sets in quickly. The population of the resonance builds up on the time scale below half of an optical cycle and regardless of the state lifetime. This supports the interpretation in terms of the four-step mechanism suggested by Strelkov.

Next, to see the time profile of the emission, we perform the Gabor transform described by Equation (2.14) for the case of the long pulse. The full-scale picture shows a periodic repetition of arches comprising the long and short trajectories, due to the periodic character of the laser field. We only plot sections containing about three half cycles since qualitatively the main features of the emission are well reflected already for this time period. In Figure 3.6(a) and Figure 3.6(b) the Gabor diagrams are shown for V_0^1 and V_0^2, respectively. The long electron trajectories appearing on the right side of the arches clearly are brighter than the short trajectories for both potentials.

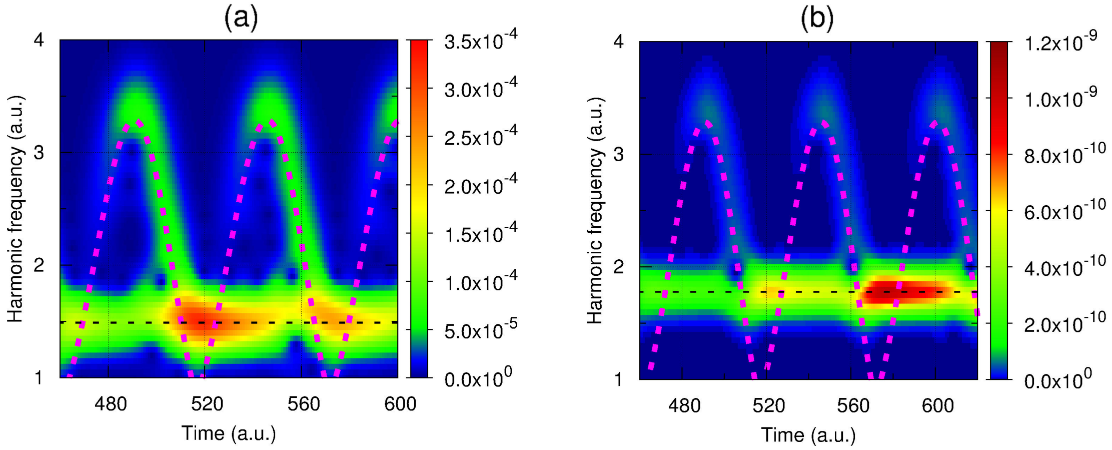

Figure 3.6: Time-frequency distribution of the harmonic radiation for (a) V_0^1 and (b) V_0^2. The laser intensity is 4×10^{14} W/cm^2. The thick dashed purple curves show classical trajectories. The black dashed lines show the positions of the resonances.

This means that the main contribution to the high-frequency part of the spectra is due to those electrons that spend more time in the continuum. The dominance of long trajectories is a well known effect in 1D TDSE calculations, while in 3D TDSE calculations the radiation is dominated by the short trajectories[23] .

The most striking feature of the spectra is the emission at the resonant energy Δ occurring continuously at all times with varying intensity. As the more intense long-trajectory branches cross the "line" formed by the emission at the resonant frequency, the intensity of the emission increases, thus indicating that the resonance radiates more intensely after the electron returns to the core. We conclude that the returning electron is captured to the resonance state in agreement with Strelkov's four-step model[137] . An increase of the resonance population is not clearly seen when the short-trajectory branch crosses the resonance emission frequency. This is due to the relatively low intensity of the emission from the short trajectories, and the signal of the resonant emission at the corresponding time remains hidden.

We can observe the difference in the emission behavior between the two potentials on the time scale of a few optical cycles shown in Figure 3.6. While for V_0^1 the process repeats itself and a strong burst of emission occurs every half-cycle, in case of V_0^2 the resonance seems to be more and more populated every half-cycle each time the electron comes back to the core. We suggest the following explanation. The lifetime of V_0^1 is $1/\Gamma_1 = 34$ a.u., so that the resonance has decayed by the time of the next electron return. In V_0^2 the resonance survives for a longer time since $1/\Gamma_2 = 141$ a.u. It does not decay during a half cycle of the laser pulse so that the population of the resonance

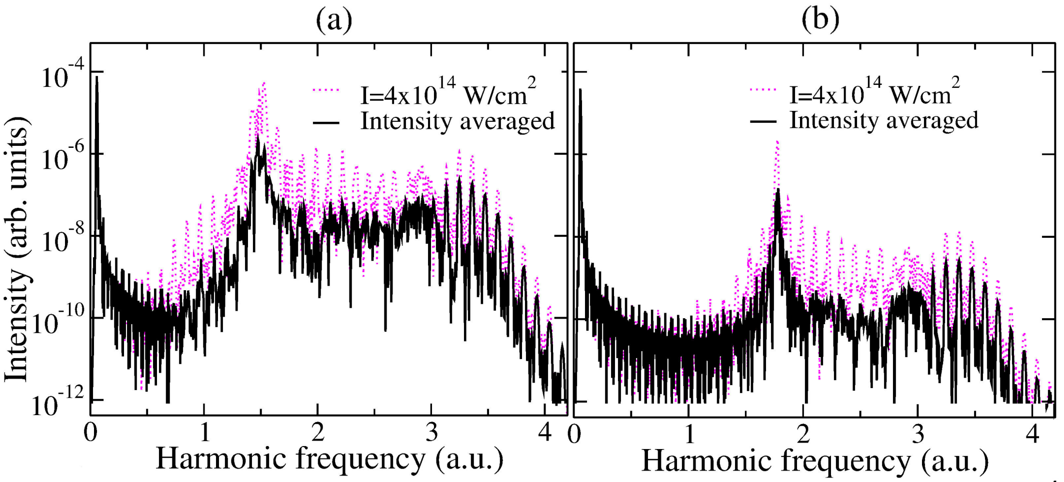

Figure 3.7: HHG spectra for a single atom (dashed curve) and after coherent summation over intensities (solid curve). (a) V_0^1. (b) V_0^2.

can potentially be increased every half cycle.

3.4.2 Phase matching

To further develop the resonant HHG model, we discuss macroscopic high harmonic generation. We simulate the effect of the spatial intensity distribution in the laser beam by coherent summation over an intensity interval (see Section 3.3). We use 31 intensities in the range from 3.85×10^{14} to $4.15 \times 10^{14}\,\mathrm{W/cm^2}$. We compare the single-atom response spectra and the intensity-averaged HHG spectra in Figure 3.7. Due to the previously discussed phase mismatch between different intensities, the intensity-averaging leads to a substantial suppression of the spectrum in the plateau region. Despite the harmonic suppression, significant enhancement in the resonant region is preserved for both considered potentials, thus indicating that the phase matching of the resonance is similar as in normal HHG from long and short trajectories. To explain the suppression and the survival of different regions of the spectra we investigate the phase matching in detail. For a fixed laser intensity we calculate the phase of the Gabor transform $G(\omega, t)$ from Equation (2.14). Knowing the phase for different intensities, we can then calculate the phase difference $\delta\phi$ of the same harmonic generated by two different laser pulses with slightly different intensities I_1 and I_2, $\delta\phi=|\phi_{I_1} - \phi_{I_2}|$. Small $\delta\phi$ implies good phase matching while large $\delta\phi$ leads to phase mismatch. The result for $I_1 = 4.14 \times 10^{14}\,\mathrm{W/cm^2}$ and $I_2 = 4.15 \times 10^{14}\,\mathrm{W/cm^2}$ is shown in Figure 3.8. The shown time interval covers about one half cycle of the laser field. One can see that the phase matching for the short trajectory (roughly the left half of the diagrams)

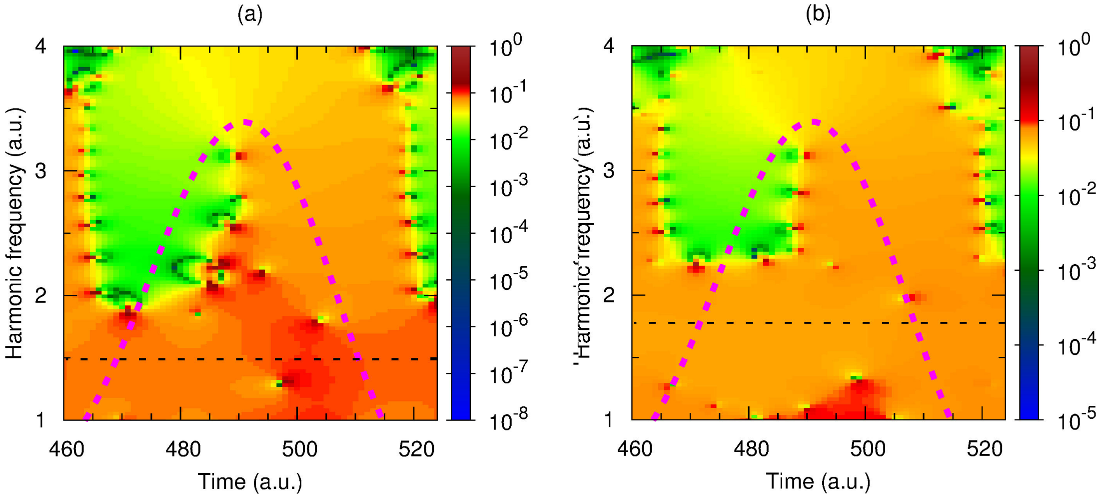

Figure 3.8: Time-frequency analysis of the harmonic phase difference between the intensities $I_1 = 4.14 \times 10^{14}\,\mathrm{W/cm^2}$ and $I_2 = 4.15 \times 10^{14}\,\mathrm{W/cm^2}$. (a) V_0^1. (b) V_0^2. The thick dashed purple curves show classical trajectories at I=4.15×10^{14} W/cm^2. The black dashed lines show the positions of the resonances.

in the plateau is better than the phase matching for the long trajectory (right half of the diagrams). We made the same test for other intensities in the range used for the intensity averaging and confirmed the conclusion holds for them as well. We thus expect that the intensity averaging favors the short trajectories and suppresses the long trajectories. In the region of the resonance, we find a large phase difference comparable to the long-trajectory phase difference. However, it is likely that a contribution from the resonance with better phase matching is not visible in these plots. This is because the calculated emission is dominated by the population of the resonance due to the long-trajectory returns. If the resonance is populated by trapping of a returning electron, we expect that the phase of the emission is locked to the phase of the returning electron. In fact, we clearly see in Figure 3.8 that the phase difference varies smoothly as the long-trajectory branch merges into the resonance around the time 510 a.u. Similarly, if an electron returns on the short trajectory and gets trapped in the resonance, the emission should be well phase matched as it is the case for the normal short-trajectory radiation.

Figure 3.9 shows the Gabor analysis for the harmonic intensity after summation over intensities. As expected, the intensity averaging effectively selects the contributions with good phase matching. Short-trajectory branches after the summation show much more intense emission than the long-trajectory branches. The signature of the resonance remains significant for both potentials.

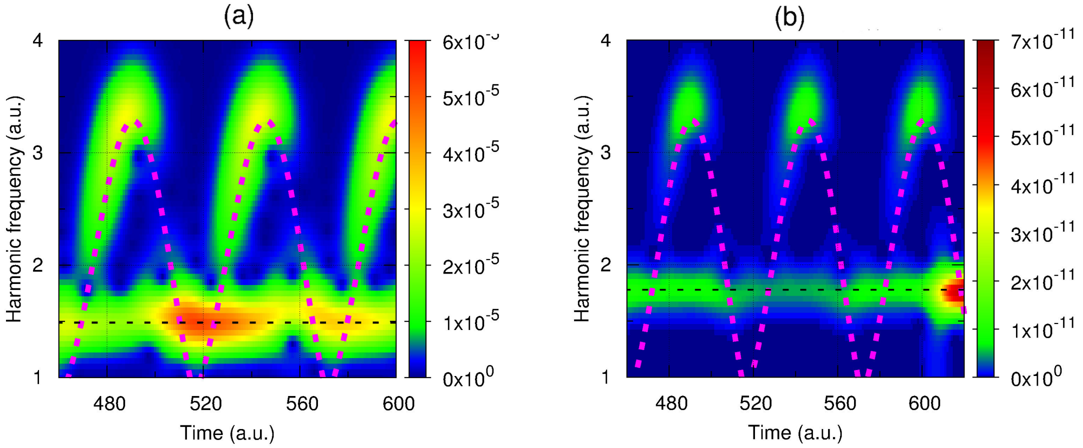

Figure 3.9: Time-frequency distribution of the harmonic radiation after intensity averaging. (a) V_0^1. (b) V_0^2. The thick dashed purple curves show classical trajectories. The black dashed lines show the positions of the resonances.

The lifetime of the resonance qualitatively changes the emission of the resonant energy as a function of time. For V_0^2, the resonance survives longer than the optical half-cycle lasts, thus the addition of the newly trapped population to the already existing population can be constructive or destructive depending on the relative phase. For example, Figure 3.9(b) shows the case where the electron return leads to a population reduction, see the decrease of harmonic emission at the time 510 a.u. Apparently, XUV radiation with very interesting step-like temporal profiles can be generated in this way. The short-lived resonance (V_0^1) decays substantially before the next return of an electron, and therefore Figure 3.9(a) does not show such a cancellation effect.

3.4.3 Resonant HHG in two dimensions

The main motivation for the 2D-calculation was to test whether HHG signal decreases as we introduce a non-zero laser ellipticity. If the emission at the resonance frequency is indeed associated with the electron recombination into the excited state, the resonant peak will decrease in the same way as HHG harmonics. The ellipticity dependence is caused by the fact that electrons miss the core due to the curved trajectory in the elliptically polarized field.

The electric field vector in this calculation is

$$\mathbf{E}(x,y,t) = f(t)\begin{pmatrix} E_x(t) \\ E_y(t) \end{pmatrix} = f(t)\begin{pmatrix} \frac{1}{\sqrt{1+\epsilon^2}}E_0\sin(\omega_0 t) \\ \frac{\epsilon}{\sqrt{1+\epsilon^2}}E_0\cos(\omega_0 t) \end{pmatrix}, \tag{3.5}$$

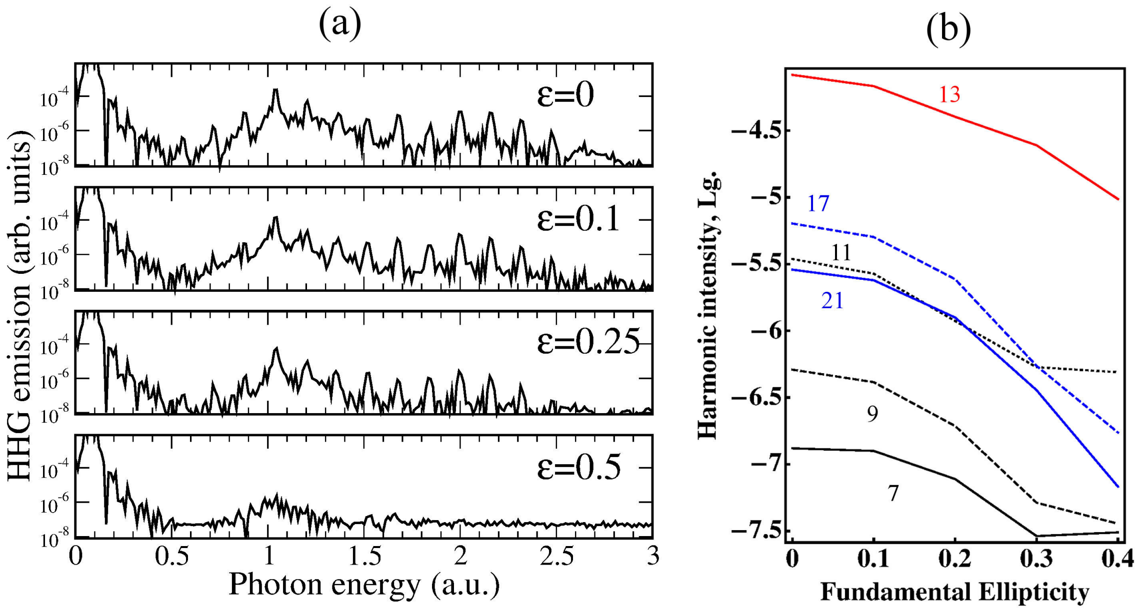

Figure 3.10: (a) HHG spectra in the 2D model for various field ellipticities, ϵ, (b) harmonic intensity dependence as a function of ellipticity: black curves - below the resonance; blue curves - in the plateau above the resonance; red curve - the resonant 13th harmonic. The numbers in panel (b) indicate the harmonic order.

with the ellipticity parameter ϵ and the pulse envelope $f(t)$. HHG spectra as a function of the driving field ellipticity ϵ are shown in the Figure 3.10(a). As it reaches ϵ=0.5, the harmonics basically disappear and the overall intensity of the emission drops by about two orders of magnitude.

The right panel, Figure 3.10(b), shows the ellipticity dependence of individual harmonics. The behavior of the resonant 13th harmonic is similar to the other harmonics in the plateau, below or above the resonance, which is in line with the suggested recollision mechanism of the resonance formation.

3.5 High harmonic generation in manganese plasma

In this section, we demonstrate that our model successfully reproduces certain features of high harmonic generation experiments. The section is based on the data obtained by the Quantum Optics and Laser Science team at Imperial College London. The experiments have been prepared and carried out by Prof. Ganeev. The results and conclusions of the collaboration are presented in our paper[68] .

In the past, significant work has been done by Rashid Ganeev to study HHG in transition metal plasmas, which are famous for having “giant” resonances,[57,114,127] for

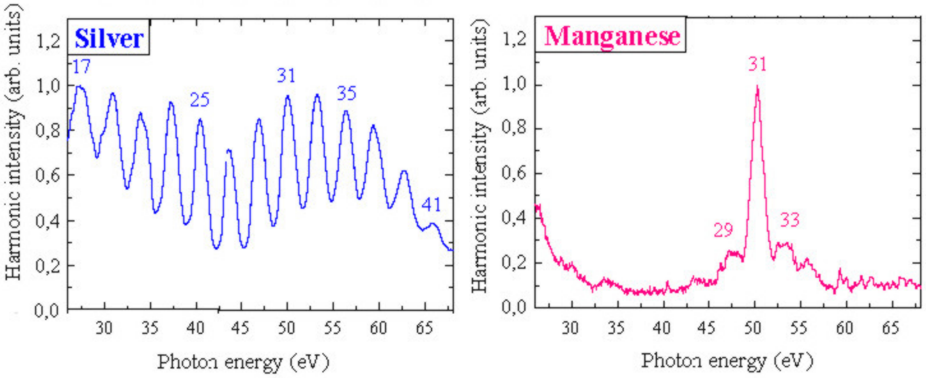

Figure 3.11: Experiment: harmonic spectra from the silver plasma (upper curve) and manganese plasma (bottom curve). From Ganeev *et al.*[68] .

instance, In, Cr, Mn[65] [62,66] .

It has been shown that manganese plasma shows the highest harmonic cut-off energy observed in plasma plumes (101st harmonic[65]) which makes it an especially interesting medium.

Below, we study HHG from an Mn plasma. Manganese is famous for the giant 3p → 3d resonance in its photoionization cross section around 50 eV (≈ 40 Mb)[40,93,94] . Since recombination is the inverse process of photorecombination, it is expected to see the resonance in the harmonic spectrum as well. Indeed, enhancement of harmonics around 50 eV has been measured in manganese plasmas for 30 fs[62] and 140 fs[63] pulses. Compared to other transition metal plasmas, only manganese allowed single harmonic enhancement, see the experimental results for HHG in Ag and Mn plasma, Figure 3.11. For Mn, the 31st harmonic was a few times higher than the neighboring harmonic orders, see Figure 3.11(b).

We focus on comparing HHG spectra by Mn from two types of laser pulses, one being an ultrashort few-cycle sub-4-fs pulse and the other one being a long 40 fs pulse. We show that the experiment is in agreement with the main features of the numerical simulation.

3.5.1 Experiment

The experiment is described in detail in our joint experimental/theoretical paper mentioned above[68] . First, a Ti:sapphire laser was used to create relatively long femotosecond pulses with energies up to 0.8 mJ. A part of the uncompressed radiation from the laser with central wavelength 800 nm was split from the beam line stage in order to create the manganese plasma plume (Figure 3.12). With some delay relative to the

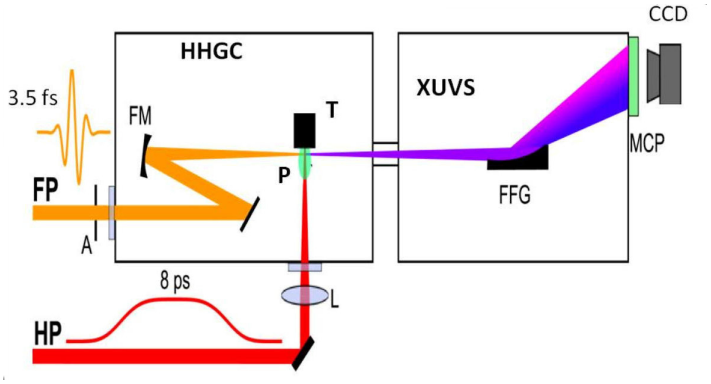

Figure 3.12: From Ganeev *et al.*[68] : experimental setup for harmonic generation in plasma plumes. FP: femtosecond harmonic drive pulse, HP: picosecond heating pulse, A: aperture, HHGC: high-order harmonic generation chamber, FM: focusing mirror, L: focusing lens, T: target, P: plasma, XUVS: extreme ultraviolet spectrometer, FFG: flat field grating, MCP: microchannel plate and phosphor screen detector, CCD: CCD camera.

heating pulse, few-cycle pulses of the Ti:sapphire laser with the FWHM 3.5 fs, wavelength 760 nm and energy 0.2 mJ were obtained in the system. After the compression, laser pulses were characterized spatially and temporally to high precision. The focus of the harmonics generating femtosecond pulse with respect to the plasma area was chosen to maximize the harmonic signal, and the intensity at the plasma area was estimated to be 6×10^{14} W/cm^2. At this step, harmonic generation occurred, and the HHG emission was analyzed with an XUV spectrometer. The harmonic spectra were spatially resolved and detected by a CCD camera[67] . Pulses with random CEP are used. A typical HHG spectrum in Mn plasma in case of ultra-short pulses is shown in Figure 3.13(b). The main effect observed in the experiment is a single broadband (2.5 eV) peak at the resonant energy exceeding the two weak neighboring harmonics by an order of magnitude.

As a second stage of the experiment, longer infrared pulse with similar intensity (4×10^{14} W/cm^2) from another Ti:sapphire laser was used. The pulse duration was 40 fs and no CEP stabilization was used. The raw image of harmonic generation with this pulse is presented in Figure 3.13(a). The plot shows a few enhanced harmonic peaks above the 31st harmonic followed by a plateau extended above the 71st harmonic. The cutoff extension can be attributed to the involvement of Mn^{2+} having high ionization potential as was already shown before[65] . Both 40 fs and 3.5 fs pulses distinctively show the involvement of Mn resonances centered around $50 - 51$ eV.

Analysis of the laser polarization dependence showed that the emission at the resonance abruptly disappeared as the polarization changes from linear to circular. As

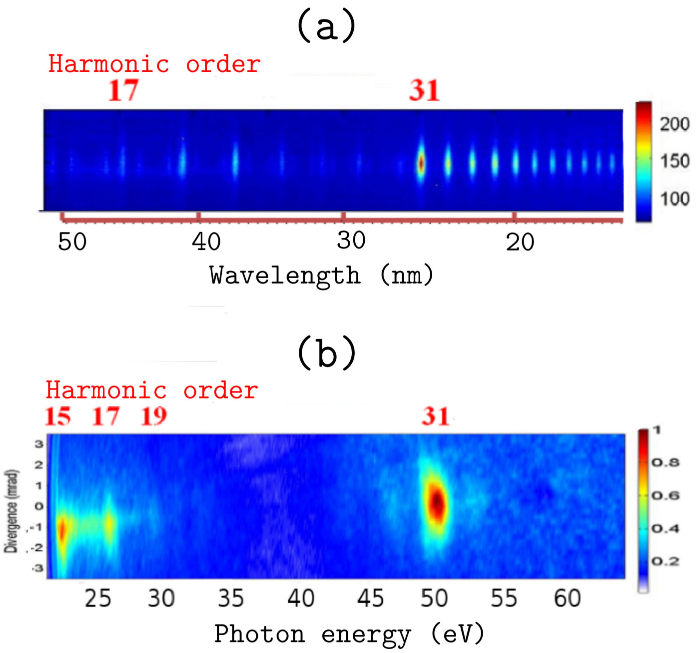

Figure 3.13: From Ganeev *et al.*[68] : experimental results, raw images of harmonic spectra from manganese plasma in the case of (a) 40 fs and (b) 3.5 fs probe pulses at the same intensity.

it was discussed before in the theoretical part describing 2D calculations, Section 3.4, this dependence indicates the recollision nature of the resonant emission.

Changing the pressure affects the pulse bandwidth and duration[115,129] . The pressure of neon in the hollow fiber system was varied to see the effect on the resonant emission. One can see in the Figure 3.14 that as the pressure increased from 1 to 2.3 bar, the intensity of the resonant emission grows from zero to the highest value. A blue shift of the peak is observed. Further increase of the pressure to 3 bar did not affect the harmonic distribution.

In addition to experiments involving pulses with random carrier envelope phase, CEP-stabilized HHG experiments were carried out in Mn plasma. With defined CEP, the spectral shape in the 30-40 eV region changes when the CEP is varied, see Figure 3.15. Two additional peaks corresponding to the 19th and the 21th harmonics appear as the CEP changes from 0 to $\pi/2$. The structure of the enhanced spectral windows around the resonant harmonic modifies its shape and the shoulder shifts from the left to the right side of the main peak. The overall envelope remains qualitatively similar.

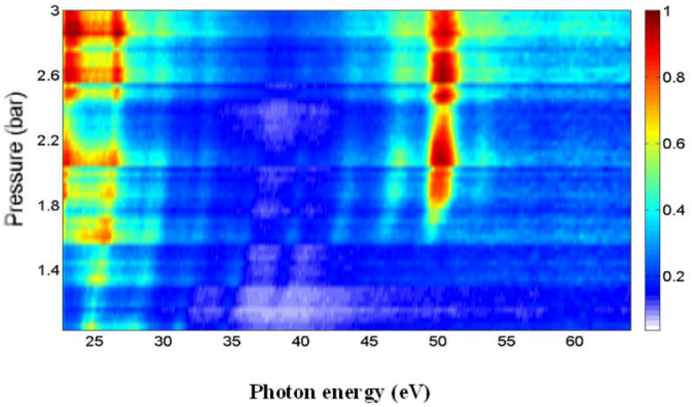

Figure 3.14: From Ganeev *et al.*:[68] experimental results, raw images of harmonic spectra from Mn plasma at different pressures of neon in the hollow fiber obtained at the same energy of probe laser pulses.

Table 3.3: Mn ion model potential parameters

param. / potential	α_1	α_2	α_3	α_4	α_5	$\mathcal{E}_{\rm g}$	$\mathcal{E}_{\rm res}$	Γ
V_0^1	1.672	1.16	0.216	8.95	1.4	-0.57 a.u.	1.33 a.u.	0.054 a.u.

3.5.2 Theory and the result of simulation

The effect observed experimentally can be seen already in the simulation for a single atom. Since the ionization potential of Mn^{2+} (33.7 eV) is almost twice as high as the ionization potential of Mn^{+} (15.6 eV) and would not correspond to the observed cutoff, we assume that the main contribution to the effect comes from singly ionized manganese. To qualitatively describe the potential of the Mn ion, we use a model potential containing a shape resonance and described by Equation (3.1). We perform the simulations in one dimension. Parameters α_i are chosen to resemble the experimental data[94] on (i) ground-state energy (ii) excited-state energy (iii) excited-state lifetime. The parameters are listed in the Table 3.3 and the shape of the potential is shown in the Figure 3.16. The resonance is 51.8 eV above the ground state. The laser field is as in Equation (2.10) and zero CEP means that the maximum of the envelope corresponds to a local maximum of $\sin(\omega_0 t)$. The central wavelength is $\lambda = 760$ nm. The laser intensity is $I_0 = 4 \times 10^{14}$ W/cm^2. We calculate HHG spectra for pulse shapes with different lengths to match the experimental FWHM and for different values of the CEP, ϕ_0. A $\sin^2$ envelope with a total length of 4 full cycles was used to model the 3.5 fs pulse, while an envelope with 4 cycles $\sin^2$ switch-on/off, 13 cycles of constant

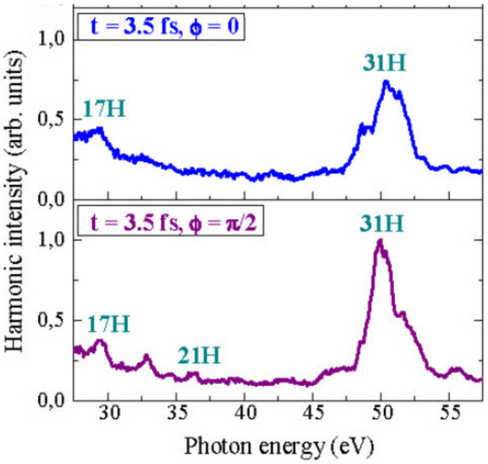

Figure 3.15: From Ganeev *et al.*:[68] experimentally detected harmonic spectra generated from manganese plasma in the case of fixed CEP, duration 3.5 fs, 3 bar pressure
top panel: $\phi_0 = 0$
bottom panel: $\phi_0 = \pi/2$.

intensity and 21 cycles total duration was used to model the 40 fs case.

The long pulse leads to a HHG spectrum that shows well defined peaks at the odd harmonic orders. The spectrum is very weakly dependent on the CEP, see Figure 3.17(a). The peak of the resonance turns out to be in between two odd harmonics, but the overall enhancement in the resonant region can be clearly observed.

Figure 3.17(b) shows the dependence of the harmonic spectrum on the CEP in the case of the short, few-cycle pulse. In all cases, the resonance dominates the spectrum. The shape of the spectrum is CEP dependent. Figure 3.17(b) compares the results for $\phi_0 = 0, \pi/4, \pi/2$. We note that the CEP dependence is stronger outside of the resonant region and the case of $\phi_0 = \pi/4$ appears to be special since a dip due to trajectory interference seems to coincide with the resonance peak. The CEP-dependence of the spectral shape suggests that for random CEP the substructure of the spectrum will

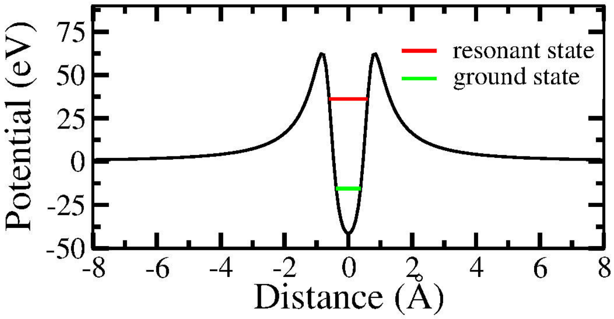

Figure 3.16: Model potential for Mn^+.

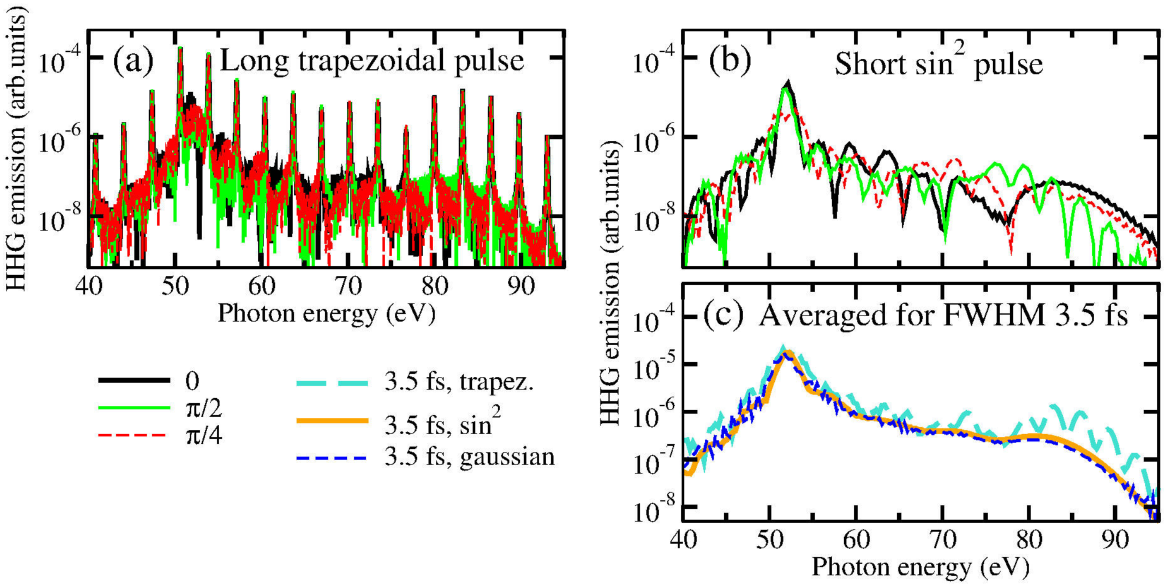

Figure 3.17: HHG spectra at different CEP from: (a) the long pulse, (b) the short pulse, (c) averaged for short pulses with FWHM 3.5 fs over 20 different values of CEP from the range $\{0; 19\pi/20\}$.

average out. Figure 3.17(c) shows the result of summation over 20 different CEPs in the range from 0 to $19\pi/20$ (the CEP difference is $\pi/20$) for different shapes of the laser pulse envelope, but similar duration (full width at half maximum, FWHM=3.5 fs). One can see that regardless of which envelope is chosen, the harmonic peaks are not clearly identifiable and only the resonance is observed.

In order to investigate temporal characteristics of the harmonic emission numerically we perform a Gabor transformation, see Equation (2.14). The temporal intensity profile of the XUV emission is calculated as the square of the time-dependent dipole acceleration after filtering out the photon energies below 1.2 a.u. (corresponding to 32.7 eV). In fact, the emission profile is not strongly affected by the filtering since the spectrum is strongly dominated by the resonance. The results are shown in Figure 3.18. One can see that in the long-pulse regime (Figure 3.18(a)) the resonance is repopulated and decaying each half cycle of the multi-cycle pulse. In the short-pulse regime (Figure 3.18(b-d)) emission of the resonance occurs at the end of the few-cycle pulse. For the short pulse, the emission takes the form of a short burst confined to one or two half cycles of the driving laser field, thus the enhanced recombination associated with the resonance is largely confined to this last cycle. While the shape of the attosecond pulse changes with CEP, the emission time with respect to the IR driving pulse changes within a few femtosecond as the maximum of the sinusoidal function of the laser field shifts.

The fact that the experimental CEP dependence was weaker than predicted theoretically for the short pulse can be attributed to the presence of a significant density of free electrons in the manganese plasma, which might diminish the difference between the HHG spectra recorded for different values of experimental CEP. The same can be said about other HHG experiments using silver and brass plasmas[64] , which did not show significant differences in harmonic spectra when comparing few-cycle pulses with fixed and random CEP.

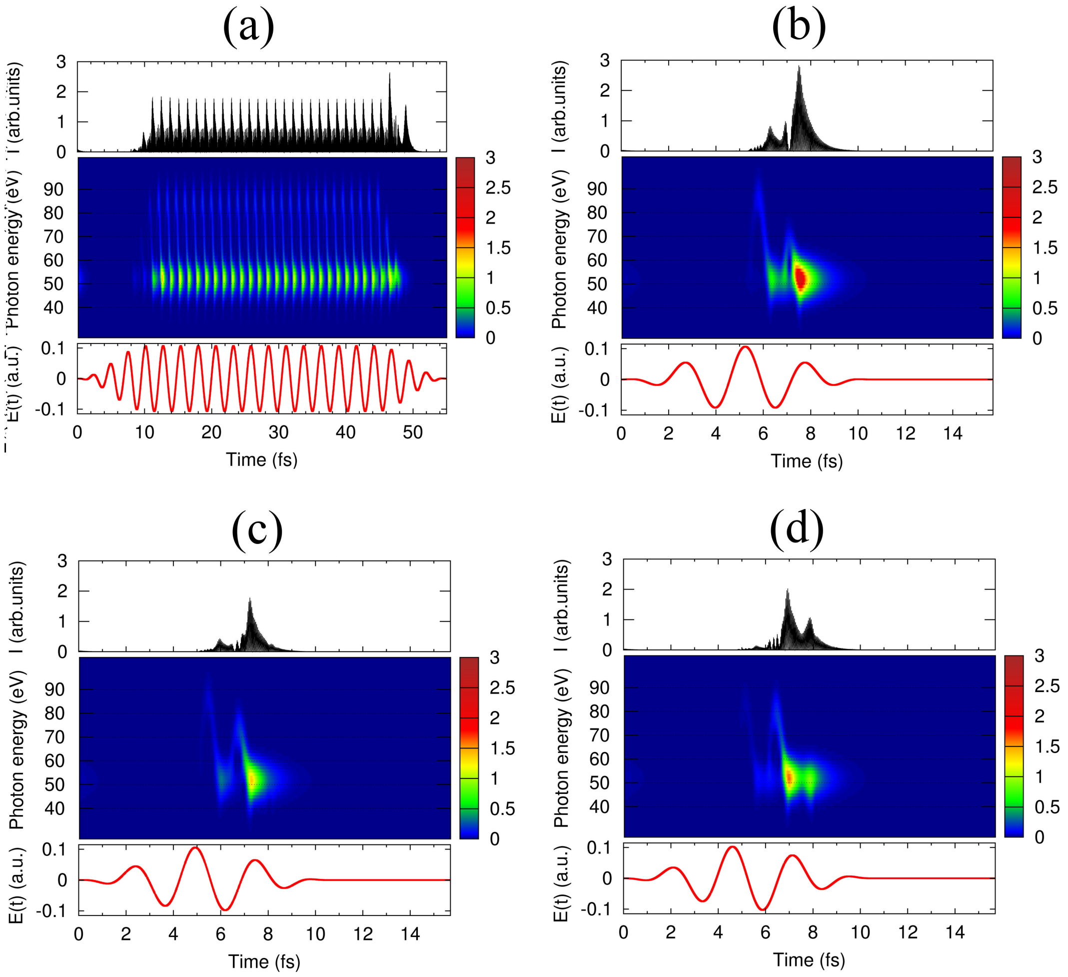

Figure 3.18: HHG driven by (a) a long 40 fs pulse with CEP $\phi_0 = \pi/4$
and few-cycle pulses with CEPs of
(b) $\phi_0 = 0$,
(c) $\phi_0 = \pi/4$,
(d)$\phi_0 = \pi/2$.
The top panels show the HHG temporal intensity profile obtained as the square of the time-dependent dipole acceleration after high pass filtering above 32.7 eV. The middle panels show the time-frequency diagrams. The red curves in the bottom panels show the time dependence of the electric field of the driving laser pulse.

3.6 Discussion

In conclusion, the potential with a barrier described by Equation (3.1) can be used to describe characteristics of experimental HHG spectra produced by a target with a resonance. The specific features that can be found in the numerical simulation are, for instance, the magnitude of the resonant enhancement and the dependence of the resonance emission intensity on the pulse length.

We have simulated the time dependence of the emission and shown that the mechanism of the resonant emission is consistent with the four-step model, according to which the recombination process consists of two steps: capture of the returning electron into the resonance and subsequent radiative transition to the ground state.

As in the experiment for HHG in Mn plasma, we found a dependence on the carrier envelope phase in case of few-cycle driving pulses. The theory has confirmed the existence of an isolated harmonic. Various applications where coherent, short pulse XUV radiation is required, could potentially use this property of the resonant emission without the losses induced by spectral dispersion or filtering. The model also suggests that the emission constitutes an isolated sub-femtosecond pulse.

Chapter 4

High harmonic generation by combined infrared and extreme ultraviolet fields in a two-level system

It is sufficient to take into account only one bound state while considering high-order harmonic generation if one is interested to understand the nature of the process or if the system excited states are not occupied. However, the approach is not suitable for real systems containing more than one bound electronic state, which can be preoccupied or excited during interaction with the laser field and may contribute to the HHG output. At commonly used laser parameters (wavelength about 800 nm and intensity of the order $10^{13} - 10^{14}$ W/cm^2) for rare gases and molecules with high ionization potential, the IR beam is not expected to lift significant population into bound excited states; in this case HHG arises mostly from transitions between continuum states and the ground state.

In the following, we consider combining the HHG-inducing IR field with an extreme ultraviolet source as a way to modify bound state populations. If the additional UV frequency is approximately in the resonance with the transition energy between the ground and an excited state, so called Rabi oscillations[33,123] become possible. In the examples considered below, the frequency of the second beam is in the extreme ultraviolet (XUV) region, i.e. in the range of electronic transitions. We expect that redistribution of electrons drastically affects the efficiency of harmonic generation.

We are interested not only in investigating the response of a two-level system to the combined effect of infrared and extreme ultraviolet fields, but also to consider significance of the excited state lifetime. It is not the absolute lifetime that matters, but the relative lifetime compared to the pulse duration. In the study, we keep the infrared field duration constant, while varying the extreme ultraviolet field duration and the potential parameters. We consider the following cases:

- extreme ultraviolet pulse duration ≈ Rabi period < resonance lifetime
- extreme ultraviolet pulse duration > Rabi period < resonance lifetime
- extreme ultraviolet pulse duration ≈ Rabi period > resonance lifetime
- extreme ultraviolet pulse duration > Rabi period > resonance lifetime.

In all cases we consider the possibility to induce Rabi oscillations.

We treat the problem by considering a single electron in a model potential. We focus on two types of model potentials. First, we study the situation when the Hamiltonian supports only two bound eigenstates. We will denote the corresponding potential with V_0^{2l}. The second type of potential has a non-stable (which we also refer as resonant, quasi-bound, autoionizing or metastable) excited state. Similarly to the previous chapter, we choose a potential containing a shape resonance described with Equation (3.1) to model the metastable state. This type of potential is denoted as V_0^{res}.

The chapter is based on our paper published previously[146] .

4.1 Previous work

The possible contribution of excited bound and quasi-bound states in high-order harmonic generation has been considered since interest to HHG first arose[12,97] . The importance of excited states and influence of bound-bound transitions at relatively low harmonic orders was discussed in 1998 by Figueira de Morisson Faria *et al.*[47] . In later papers[49,50] , it was shown that there is a link between the simple man's model and the behavior of two-level atom in strong fields since both models can be described as a three-step process. In case of a two-level system, there is population transfer between field-dressed states making it very similar to the three steps of the simple man's model. The authors found that in case of a system with two bound states and continuum states, electron transfer from the ground to the excited state and back, producing harmonics, i.e. a field-dressed bound state instead of a continuum state, plays the main role in the process.

HHG enhancement from H_2^+ by initial state preparation was discussed by Gupta and Neuhauser in 1998[73] . Ivanov and Kheifets considered HHG enhancement from excited 2p state of atomic lithium and superposition of the ground and excited states[85] .

HHG from infrared irradiation supported by additional fields affecting the excited state population has been studied experimentally and theoretically as well. It has been suggested to use attosecond pulses obtained by HHG from a secondary source as an auxiliary XUV field to enhance HHG[9,80] . Experimentally, a mixture of Xe and He was used to observe dramatic enhancement of harmonic generation in He boosted by the harmonic field produced by Xe[141,142] . Another experiment showed enhancement by one order of magnitude in He using attosecond pulse trains from a Xe-filled capillary[14] . A dual-gas-cell setup has been investigated in the paper by Brizuela *et al.*[16] . Propagation effects have been simulated in detail.[60,132] Fleischer *et al.*[53] studied HHG by a superposition of a powerful IR pulse and a weak XUV pulse leading to the cutoff extension as a single-atom effect. The authors used Floquet theory and classical recollision model. Popruzhenko *et al.*[120] modified the Lewenstein model upon the addition of weak UV field. It was concluded that the HHG yield can be significantly increased. Buth *et al.*[18,19] coupled the two-electron problem with the problem of XUV-assisted HHG generation in gases such as Ne and Kr, considering conditions as at the free electron laser FLASH in Hamburg. The authors have developed a theoretical formalism and discovered a second plateau in the HHG spectrum as a result of electron recombination with a core hole. Finally, it was suggested that the second longer-wave laser can be efficiently used to assist HHG by alkali metals due to the strong coupling between the ground state and the first excited state[134] . In this case, HHG is generated by intense mid-infrared laser, and the coupling is induced by a laser working in the visible or UV range. A numerical model for HHG from rubidium vapor was considered by Hadas and Bahabad[74] showing that the population control can be extremely useful for macroscopic control. In addition, numerical simulation of third harmonic generation by alkali atoms, performed by Ciappina *et al.*,[27] showed the signature of Rabi flopping if the laser pulse is in tune with the 4s - 4p transition of K atom.

This work presents a theoretical numerical investigation of HHG driven by two fields, where different types of XUV pulses are considered.

4.2 Calculation methods and parameters

4.2.1 Methods

In this chapter, the TDSE, see Equation (1.5), is solved in 1D with the use of the SOM (see Chapter 1). The potential parameters α_i, $i \in \{1, ..5\}$ are chosen depending on the desired properties of the ground and excited states.

We make sure that the potential indeed supports only one excited state to avoid undesirable effects from higher excited states. In this chapter, not only the ground-state wave function, but also the excited-state wave function is required for the calculations (for instance, to calculate Rabi frequency). We solve the Schrödinger equation for the unperturbed Hamiltonian in the interval from $x_{\min}$ to $x_{\max}$ using *Mathematica*. We use $x_{\mathrm{min}} = -x_{\mathrm{min}} = 50$ a.u. For the ground state, the required asymptotic behavior is that the wave function decays exponentially in the classically forbidden region. For the metastable excited state, the wave function exhibits periodic oscillations outside of the potential barrier. We require that resulting wave function is either symmetric or antisymmetric depending on the quantum number. For the bound excited state and for the ground state, the wave function is normalized to unity. If the potential has a metastable excited state, the wave function of such a state has sinusoidal tails outside of the core region. We normalized the wave function by unity by integrating the wave function modulus squared inside of the region {-5 a.u. ... 5 a.u.}. The wave function decays inside of the potential barrier. The limits are chosen such that the wave function amplitude becomes exponentially small at the edge of the integration region compared to its maximum value. The metastable state energy value and width are obtained by propagating a randomly chosen wave function orthogonal to the ground state without the field as described above in Chapter 1 and Chapter 3.

4.2.2 Potentials

We employ the model potential described in Chapter 3 with Equation (3.1) for both systems (with a stable or a metastable excited state). The parameters α_i, $i \in \{1, ..5\}$, are real and non-negative. By varying the height and the width of the potential barrier, i.e. the parameters α_4 and α_5, we can change the excited state energy, its width Γ and the lifetime $T_{\mathrm{decay}} = 1/\Gamma$.

The first type of potential, $V_0^{2\mathrm{l}}$, depicted in Figure 4.1(a), supports two bound electronic states. Parameters α_4 and α_5 are set to zero such that the potential is a simple potential well. For the second type of potential, referred to as V_0^{res} and containing a metastable (a resonant) state, we set α_4 and α_5 to be greater than zero. The potential is shown in Figure 4.1 (b). We use the following notation: $\mathcal{E}_{\mathrm{g}}$ is the ground state energy, $\mathcal{E}_{\mathrm{e}}$ and $\mathcal{E}_{\mathrm{res}}$ are the bound excited and the resonant excited state energies, Δ the energy gap between the ground and the excited states, Γ for the metastable state width. For both potentials, the parameters are listed in Table 4.1.

All parameters α_i for both types of potentials are listed in the table 4.1.

4.2.3 Fields

All employed external fields are as in Equation (2.10). To investigate the influence of the excited-state lifetime, we use two types of XUV pulses: an ultrashort XUV pulse, lasting less than half an IR period, and a long XUV pulse, which has a duration

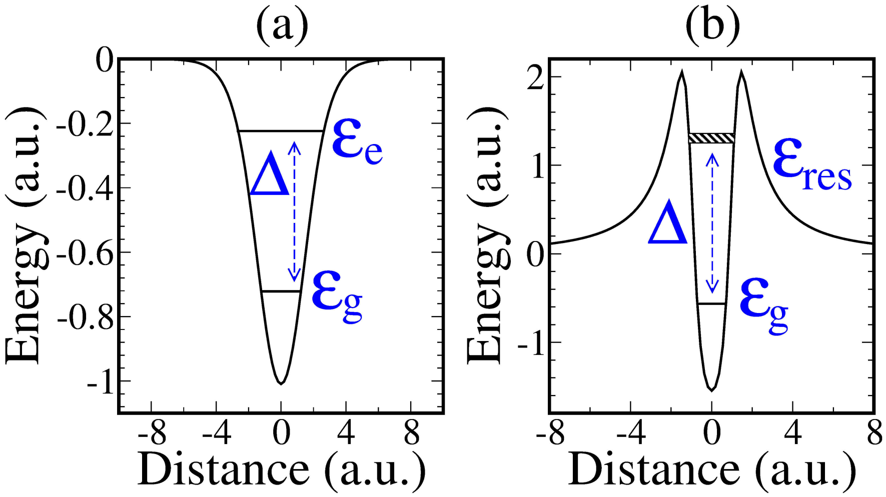

Figure 4.1: Model potentials (a) with two bound states, (b) with a shape resonance. The potential parameters are listed in table 4.1.

Table 4.1: Parameters, ground and excited-state energies and the metastable state width for the potentials depicted in Figure 4.1.

param. potential	α_1	α_2	α_3	α_4	α_5	$\mathcal{E}_{\mathrm{g}}$	$\mathcal{E}_{\mathrm{e,res}}$	Γ
V_0^{2l}	1.52	1.28	0.8	0	0	-0.72 a.u.	-0.24 a.u.	-
V_0^{res}	1.66	1.07	0.2	7.3	0.7	-0.57 a.u.	1.33 a.u.	0.1 a.u.

comparable with the IR pulse length. In the following, we refer to the “short” and “long” pulses as XUV$_s$ and XUV$_l$, respectively. The short pulse is used to simulate a single attosecond pulse. The wavelength of the infrared field is 765 nm (corresponding to ω_0=0.06 a.u.) and the duration of the IR pulse is 1465.3 a.u. (which corresponds to 14 optical cycles). In case of the two-bound-level system with potential V_0^{2l}, we consider a near resonant XUV field with frequency 0.51 a.u. For V_0^{res}, the used XUV field has the frequency 1.88 a.u. We choose a trapezoidal envelope and duration of about 985 a.u. for XUV$_l$. The ramps and the plateau lengths are 10+60+10 XUV cycles for the 0.51 a.u. field and 37+221+37 in the case of the 1.88 a.u. field. The duration of XUV$_s$ is about 37 a.u., corresponding to three optical cycles of the 0.51 a.u. field and 11 optical cycles of the 1.88 a.u. field. The XUV$_s$ envelope has a $\sin^2$ shape. The short pulse can be viewed as a single attosecond pulse produced by HHG from a different target, as suggested previously in the papers by Ishikawa, Takahashi *et al.*[82,141] The long pulse models an XUV field produced by, for example, FLASH with a duration of 10-50 fs (FWHM).

4.3 Population oscillations in a two-level system by XUV driving

Before discussing the specific features of HHG in combined XUV and IR fields, we discuss what effect extreme ultraviolet fields or infrared fields have on a two-state system when applied independently. We give a brief theoretical overview and explanation of Rabi oscillations and show numerically obtained photoemission spectra for the considered potentials. More detailed theory can be found, for example, in the textbook of Meystre and Sargent III[112] .

In a two-state system, we denote the ground state and the excited state as $\mathcal{E}_{\mathrm{g}}$ and $\mathcal{E}_{\mathrm{e}}$, respectively. The energy difference between the two levels lying in XUV region is

$$\Delta = \mathcal{E}_{\mathrm{e}} - \mathcal{E}_{\mathrm{g}}. \tag{4.1}$$

$\mathcal{E}_{\mathrm{g,e}}$ are eigenstates of the unperturbed Hamiltonian H_0. In a sufficiently strong near-resonant linearly polarized electric field, induced transitions between the states occur such that the electron oscillates between the ground and the excited state with comparable probabilities amplitudes. The field detuning is defined as

$$\delta = \omega_{\mathrm{XUV}} - \Delta, \tag{4.2}$$

and we consider in the following $|\delta| \ll \Delta$. The resulting wave function of the system, Ψ_{2level}, can be written as a superposition of the wave functions of the ground and excited states:

$$\Psi_{\mathrm{2level}}(\mathbf{r}, t) = C_g(t)\Psi_g(\mathbf{r})\mathrm{e}^{-i\mathcal{E}_{\mathrm{g}}t} + C_e(t)\Psi_e(\mathbf{r})\mathrm{e}^{-i\mathcal{E}_{\mathrm{e}}t}. \tag{4.3}$$

The atom-field coupling is introduced by adding the term $H'(t) = \mathbf{r} \cdot \mathbf{E}(t)$ to the unperturbed Hamiltonian, H_0, as described in Chapter 1 (see Section 1.1). Substituting Ψ_{2level} into the TDSE, Equation (1.1), we obtain

$$C_g H' \Psi_g \mathrm{e}^{-i\mathcal{E}_{\mathrm{g}}t} + C_e H' \Psi_e \mathrm{e}^{-i\mathcal{E}_{\mathrm{e}}t} = i\dot{C}_g \Psi_g \mathrm{e}^{-i\mathcal{E}_{\mathrm{g}}t} + i\dot{C}_e \Psi_e \mathrm{e}^{-i\mathcal{E}_{\mathrm{e}}t}. \tag{4.4}$$

The eigenfunctions are orthonormal. With this in mind, we multiply Equation (4.4) either by $\Psi_g^*(\mathbf{r})$ or $\Psi_e^*(\mathbf{r})$. After integrating over space, we obtain

$$\dot{C}_g(t) = -i\left[C_g(t)H'_{gg} + C_e(t)H'_{ge}\mathrm{e}^{-i\Delta t}\right], \tag{4.5}$$

$$\dot{C}_e(t) = -i\left[C_g(t)H'_{eg}\mathrm{e}^{i\Delta t} + C_e(t)H'_{ee}\right], \tag{4.6}$$

where H'_{ij} is the matrix element $\langle\Psi_i|\, H'\,|\Psi_j\rangle$, $i,j = g,e$. We choose the electric field to be parallel to the z-axis, $\mathbf{E}(t) \equiv \mathbf{E}_z(t)$. For a monochromatic field in the XUV region, we have

$$E_z(t) = E_{\mathrm{XUV}}\cos(\omega_{\mathrm{XUV}}t) = E_{\mathrm{XUV}}\frac{\mathrm{e}^{i\omega_{\mathrm{XUV}}t} + \mathrm{e}^{-i\omega_{\mathrm{XUV}}t}}{2} \tag{4.7}$$

After introducing the dipole matrix element, $\mu_{ij} = -\langle\Psi_i|\, z\,|\Psi_j\rangle\,,\ \ i,j = g,e$ we can write

$$H'_{ij} = -E_{\mathrm{XUV}}\frac{\mathrm{e}^{i\omega_{\mathrm{XUV}}t} + \mathrm{e}^{-i\omega_{\mathrm{XUV}}t}}{2}\mu_{ij}. \tag{4.8}$$

Due to the symmetry properties of the wave functions, $\mu_{gg} = \mu_{ee} = 0$ and $\mu_{ge} = \mu_{eg}^* = \mu$. We can now rewrite Equation (4.5) and Equation (4.6) for the wave function expansion coefficients. We denote

$$d_E = \mu E_{\mathrm{XUV}}. \tag{4.9}$$

In the case of two bound states, d_E is real. We rewrite Equation (4.5), Equation (4.6) as

$$\dot{C}_g(t) = id_E\frac{\mathrm{e}^{i(\omega_{\mathrm{XUV}}-\Delta)t} + \mathrm{e}^{-i(\omega_{\mathrm{XUV}}+\Delta)t}}{2}C_e(t), \tag{4.10a}$$

$$\dot{C}_e(t) = id_E\frac{\mathrm{e}^{-i(\omega_{\mathrm{XUV}}-\Delta)t} + \mathrm{e}^{i(\omega_{\mathrm{XUV}}+\Delta)t}}{2}C_g(t). \tag{4.10b}$$

We take into account $\omega_{\mathrm{XUV}} \approx \Delta$ and thus $\mathrm{e}^{i(\omega_{\mathrm{XUV}}+\Delta)t} \approx \mathrm{e}^{i2\omega_{\mathrm{XUV}}t}$. Therefore, we can neglect the rapidly oscillating terms since they average out to approximately zero. We then transform the equations to the rotating frame of reference. This approach is called rotating wave approximation (RWA)[112] . In the rotating frame of reference, $C_g(t) = \tilde{C}_g(t)\mathrm{e}^{i\delta t/2}$, $C_e(t) = \tilde{C}_e(t)\mathrm{e}^{-i\delta t/2}$, and

$$\dot{\tilde{C}}_g(t) = \frac{i}{2}\left[-\delta\tilde{C}_g(t) + d_E\tilde{C}_e(t)\right], \tag{4.11a}$$

$$\dot{\tilde{C}}_e(t) = \frac{i}{2}\left[\delta\tilde{C}_e(t) + d_E\tilde{C}_g(t)\right]. \tag{4.11b}$$

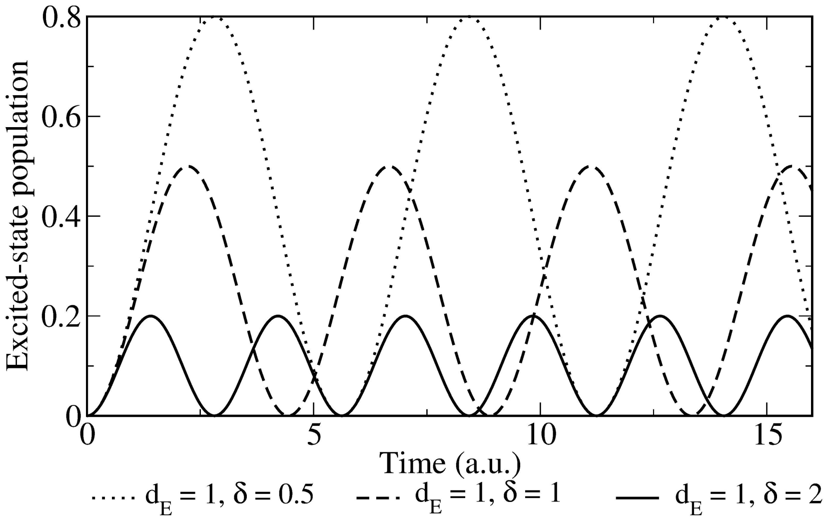

Figure 4.2: Population of the excited state of a two-level system. Dashed, dotted and solid curves correspond to different detuning values, and d_E=1.

Introducing the vector $\tilde{\mathbf{C}} = \begin{pmatrix} \tilde{C}_g(t) \\ \tilde{C}_e(t) \end{pmatrix}$ and the matrix $\mathbf{R} = \begin{pmatrix} -\delta & d_E \\ d_E & \delta \end{pmatrix}$, we rewrite in matrix form

$$\dot{\tilde{\mathbf{C}}}(t) = \frac{i}{2}\mathbf{R} \cdot \tilde{\mathbf{C}}(t). \tag{4.12}$$

Finally, we get

$$\tilde{\mathbf{C}}(t) = \begin{pmatrix} \cos\frac{\Omega_R t}{2} - \frac{i\delta}{\Omega_R}\sin\frac{\Omega_R t}{2} & \frac{id_E}{\Omega_R}\sin\frac{\Omega_R t}{2} \\ \frac{id_E}{\Omega_R}\sin\frac{\Omega_R t}{2} & \cos\frac{\Omega_R t}{2} + \frac{i\delta}{\Omega_R}\sin\frac{\Omega_R t}{2} \end{pmatrix} \tilde{\mathbf{C}}(0) \tag{4.13}$$

where Ω_R is the Rabi frequency,

$$\Omega_R = \sqrt{{d_E}^2 + \delta^2}. \tag{4.14}$$

We assume that in the beginning only the ground state is populated,

$$C_g(0) = 1, \tag{4.15a}$$

$$C_e(0) = 0. \tag{4.15b}$$

Substituting $\tilde{C}_{e,g}(0)$ into Equation (4.15), we derive for the bound-state populations

$$|C_g(t)|^2 = \cos^2\left(\frac{\Omega_R\, t}{2}\right) + \frac{\delta^2}{\Omega_R^2}\sin^2\left(\frac{\Omega_R\, t}{2}\right), \tag{4.16a}$$

$$|C_e(t)|^2 = \frac{{d_E}^2}{\Omega_R^2}\sin^2\left(\frac{\Omega_R\, t}{2}\right). \tag{4.16b}$$

Figure 4.2 shows excited-state population dynamics for different ratios $\mathrm{d_E}/\delta$.

If the excited state is metastable with the width Γ, d_E is complex, and the matrix $\mathbf{R}$ in Equation (4.12) becomes $\mathbf{R}^\Gamma = \begin{pmatrix} -\delta & d_E \\ d_E^* & \delta + i\Gamma \end{pmatrix}$ and the generalized Rabi frequency becomes complex:

$$\Omega_R^\Gamma = \sqrt{{d_E}^2 + (\delta + i\Gamma/2)^2}. \tag{4.17}$$

The solution in the rotating frame system is[112]

$$\tilde{\mathbf{C}}(t) = \begin{pmatrix} \cos\frac{\Omega_R^\Gamma t}{2} - \frac{i\delta - \Gamma/2}{\Omega_R^\Gamma}\sin\frac{\Omega_R^\Gamma t}{2} & \frac{id_E}{\Omega_R^\Gamma}\sin\frac{\Omega_R^\Gamma t}{2} \\ \frac{id_E^*}{\Omega_R^\Gamma}\sin\frac{\Omega_R^\Gamma t}{2} & \cos\frac{\Omega_R^\Gamma t}{2} + \frac{i\delta - \Gamma/2}{\Omega_R^\Gamma}\sin\frac{\Omega_R^\Gamma t}{2} \end{pmatrix} \mathrm{e}^{-\Gamma t/4}\tilde{\mathbf{C}}(0) \tag{4.18}$$

With the initial conditions from Equation (4.15), we find that the population oscillations are damped with the decay rate $\Gamma/2$:

$$|C_g(t)|^2 = \left|\cos\frac{\Omega_R^\Gamma t}{2} - \frac{i\delta - \Gamma/2}{\Omega_R^\Gamma}\sin\frac{\Omega_R^\Gamma t}{2}\right|^2 \mathrm{e}^{-\Gamma t/2} \tag{4.19a}$$

$$|C_e(t)|^2 = \left|\frac{d_E}{\Omega_R^\Gamma}\right|^2 \left|\sin\left(\frac{\Omega_R^\Gamma\, t}{2}\right)\right|^2 \mathrm{e}^{-\Gamma t/2}. \tag{4.19b}$$

4.4 High-order harmonic generation results for combined infrared and extreme ultraviolet fields

4.4.1 Response to XUV field only and IR field only

In order to understand the mixed-field effect on two-level systems, it has to be compared with the effect of infrared and extreme ultraviolet fields, applied independently. In this section, we investigate numerically the response of the quantum system supporting one bound and one either bound or metastable state to the XUV field only and the IR laser field only.

The duration of the XUV and IR pulses is described in Section 4.2.3 and shown in Figure 4.3. A powerful IR beam can also produce population oscillations. We eliminate this possibility by choosing the fields relative intensity such that the IR-induced oscillations are negligible compared to the ones driven by the XUV field. (We note, however, that the relative weakness of the population oscillations by the IR field is not a necessary condition for the effect observed below.) We take the following parameters into consideration: the transition energy between the ground and the excited state is larger for V_0^{res} than for V_0^{2l}, which necessitates a greater difference between the field intensities in the first case.

The ground and the excited state energies are shifted due to the IR-induced Stark effect related to the dynamic polarizability, α. In a two-level model, the Stark shift is the same for the ground state and for the excited state, except for the sign. In order to estimate the magnitude of the effect, we neglect the contribution of the transitions to the continuum and take into account low field frequency. With the condition

$$\mu E_0 \ll |\omega_0 - \Delta|, \tag{4.20}$$

perturbation theory can be used. Again, Δ is the energy gap between the ground and the excited states, $\mu_{\mathrm{g,e/res}}$ is the dipole matrix element corresponding to the transition between the ground and excited states, and $|\mu_{g,e/res}| \equiv \mu$. Knowing the wave functions, we calculate numerically μ_{2l}=1 a.u. and μ_{res}=0.47 a.u. for the potentials V_{2l} and V_{res}, respectively, so that Equation (4.20) is satisfied. The Stark shift is then[15,36]

$$\delta\mathcal{E} = \pm\frac{\alpha E_0^2}{4} = \pm\frac{E_0^2}{2}\frac{\Delta\mu^2}{\Delta^2 - \omega_0^2} \approx \pm\frac{E_0^2}{2}\frac{\mu^2}{\Delta}. \tag{4.21}$$

The ground state shift is negative while the excited state shift is positive. The field frequency is negligible in comparison with the transition frequency[15,36] . At the considered field intensities, the IR-induced Stark shift is of the order 10^{-3} a.u. and is negligible in comparison with $\mathcal{E}_{\mathrm{g}}$, $\mathcal{E}_{\mathrm{e/res}}$, Δ and the frequency of the XUV-induced Rabi oscillations, Ω_R.

The coupling induced by the XUV field for both potentials at the given intensities is negligible compared to the detuning and the frequency of the oscillations is

$$\Omega_R \approx |\omega_{\mathrm{XUV}} - \Delta|. \tag{4.22}$$

The left-hand side of Figure 4.3 applies to the system with two bound states and the right-hand side applies to the system with a shape resonance. The bottom panels show the XUV and IR fields used in the calculation. The top panels show the corresponding time-dependent population of the field-free ground state when exposed to the XUV field

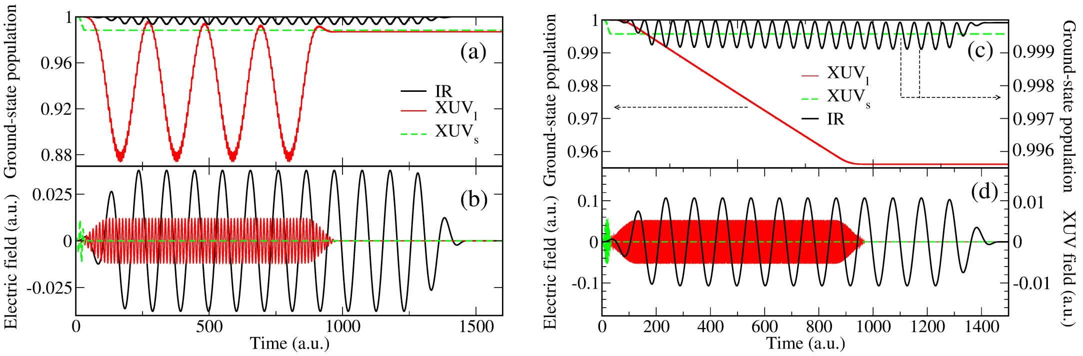

Figure 4.3: Left: Results for the two-bound-level system. Right: Results for the shape resonance. (a), (c) Population of the ground state when the system is driven by the XUV field only or by the IR field only. (b) The IR field and the XUV field used in the case of the two-bound-level system; the intensities of the IR and XUV fields are $5 \times 10^{13}\,\mathrm{W/cm^2}$ and $5 \times 10^{12}\,\mathrm{W/cm^2}$, respectively; the XUV$_l$ and XUV$_s$ pulses consist of 10+60+10 and 3 optical cycles, respectively; the XUV frequency is 0.51 a.u. (d) The IR field and the XUV field for the system with a shape resonance; the intensities of the IR and XUV fields are $4 \times 10^{14}\,\mathrm{W/cm^2}$ and $10^{12}\,\mathrm{W/cm^2}$, respectively; the XUV$_l$ and XUV$_s$ pulses consist of 37+221+37 and 11 optical cycles, respectively; the XUV frequency is 1.88 a.u.

only or IR field only (not combined). Figure 4.3(a) shows that the long XUV pulse causes Rabi oscillations in the ground-state population of the two-level system. The corresponding oscillations of the excited-state population (not shown) are in antiphase to the ground-state oscillations. In contrast, the short XUV pulse is shorter than the Rabi period, and its main effect is a quick transfer of a small population to the excited state without Rabi oscillations. For V_0^{res} (Figure 4.3, right hand side), no Rabi oscillations can be observed even when the XUV pulse is sufficiently long. This is due to the fast decay of the resonance state.

In the IR field, the population oscillates with a period equal to half of the IR period for both $V_0^{2\mathrm{l}}$ and V_0^{res}. This can be understood as a consequence of an instantaneous IR-dressed ground state that differs from the ground state. The overlap with the field-free state is thus less than one and oscillates with the IR field.

Figure 4.4 shows the probability to find an electron outside of the core for the two potentials, (a) for $V_0^{2\mathrm{l}}$ and (b) V_0^{res}. The black curve shows the ionization probability due to IR field only and the red curve illustrates the effect of XUV$_l$ only. One observes that the ionization by the XUV field is dominant. Figure 4.5 shows the spectrum of $|\tilde{a}(\omega)|^2$, where $\tilde{a}(\omega)$ is the Fourier transformed dipole acceleration. Only the first order peaks, and not the higher order peaks, exist due to the high field frequency and the relatively low intensity. Top and bottom panels apply to the two different

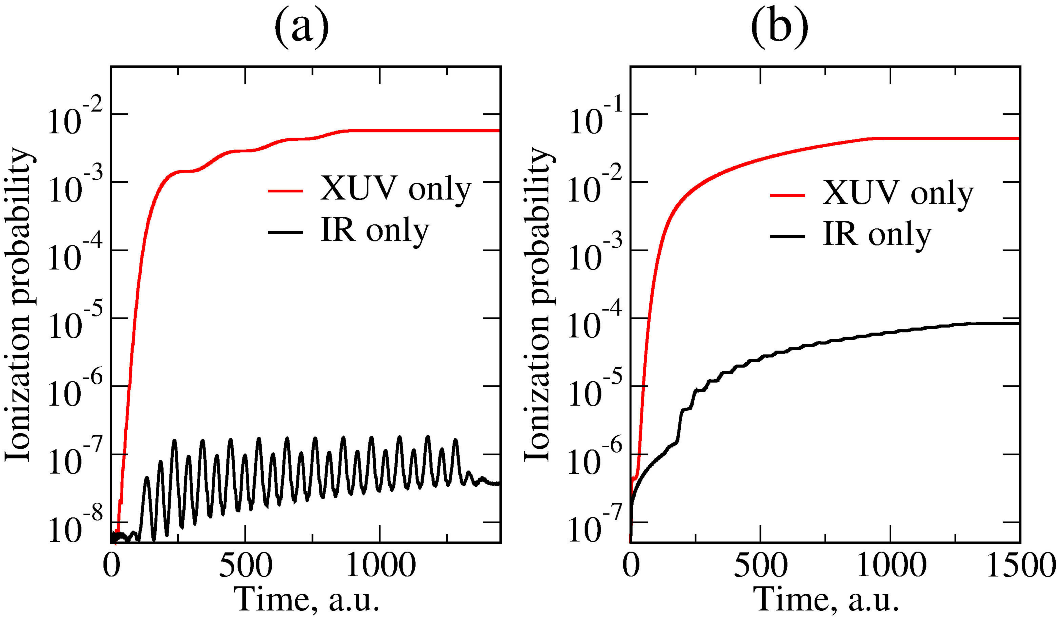

Figure 4.4: Probability of ionization of (a) the two-bound-level system, (b) the system with a shape resonance. The parameters of the fields are the same as in the Figure 4.3 depending on the potential. Black and red curves correspond to the effect of the IR pulse only and “long” XUV pulse only, respectively.

potentials. Figure 4.5(a) shows the results for the two-level system V_0^{2l}, Figure 4.5(b) for the system with a metastable state. The green curve describes the effect of the “short” XUV$_s$ pulse. For both potentials, the spectra have a peak at the energy corresponding to the transition between the ground and the excited state Δ. In the case that the excited state is stable (Figure 4.5(a)), the spectrum exhibits a clear peak at the transition energy 0.51 a.u. The spectrum generated by XUV$_l$ shows that the long XUV pulse causes a Rabi splitting of the peak, analogous to the Autler-Townes effect in absorption lines[6] and photoelectron spectra[153] . In case of the quickly decaying resonance, Figure 4.5(b), no splitting of the main peak at Δ=1.9 a.u. is observed since no population oscillations take place.

4.4.2 System with two bound states

In this section, we consider a system with two bound electronic states, using the potential we previously denoted as V_0^{2l}, see Figure 4.1(a). The field parameters are as stated in Section 4.2.3 and Section 4.4.1 and as shown in Figure 4.3 (b). The IR field with intensity $I = 5 \times 10^{13}\,\mathrm{W/cm^2}$ corresponds to the ponderomotive potential $U_p = E_0^2/(4\omega_0^2)$=0.10 a.u., and the cutoff in the HHG spectrum by the IR field only is expected at $3.17U_p + I_p$=1.03 a.u. (≈ 17th harmonic of the IR field).

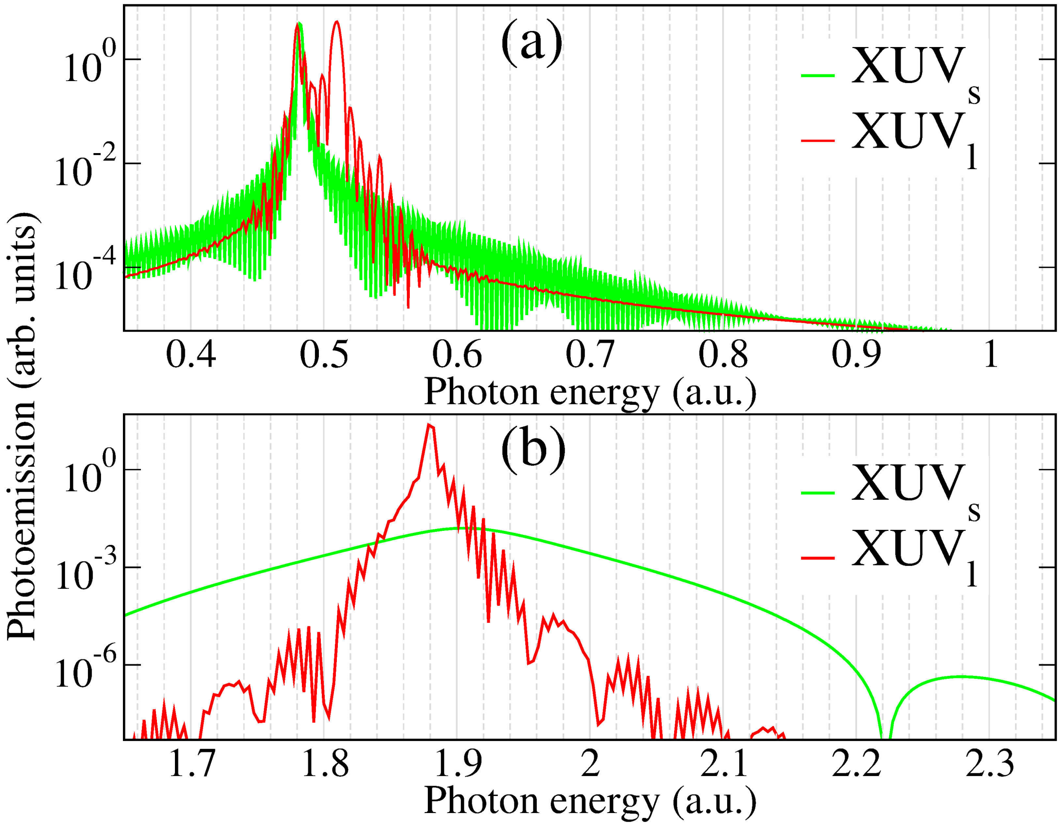

Figure 4.5: Photon emission spectra using the XUV field only. (a) the system with two bound states (b) the system with a shape resonance. The parameters of the fields are the same as in the Figure 4.3.

Dependence of the population oscillations on the XUV field intensity

First, we explore the Rabi oscillations caused by the combination of the long XUV pulse (XUV_l) and the IR field. Figure 4.6 shows that excited-state population oscillations are observed at any of the considered XUV intensities, from 5×10^{12} to 5×10^{14} W/cm^2. As the XUV field intensity grows, the amplitude and the frequency of the oscillations (black curve) and the ionization probability (red curve) increase. The amplitude of the oscillations decays with time, even when the XUV intensity is low, in contrast to the case where the system is driven by the XUV field only, see Figure 4.3(a). For high XUV intensity, the decay of the oscillations is due to the strong ionization. For low XUV intensity, the decay is apparently due to the presence of the IR field. For the upper state, the IR field can be considered adiabatic, and the ionization occurs in the tunneling regime[37] , thus effectively introducing the finite lifetime of the excited state, as it was discussed in Section 4.4.1.

Figure 4.7 compares frequency and amplitude of the excited-state population

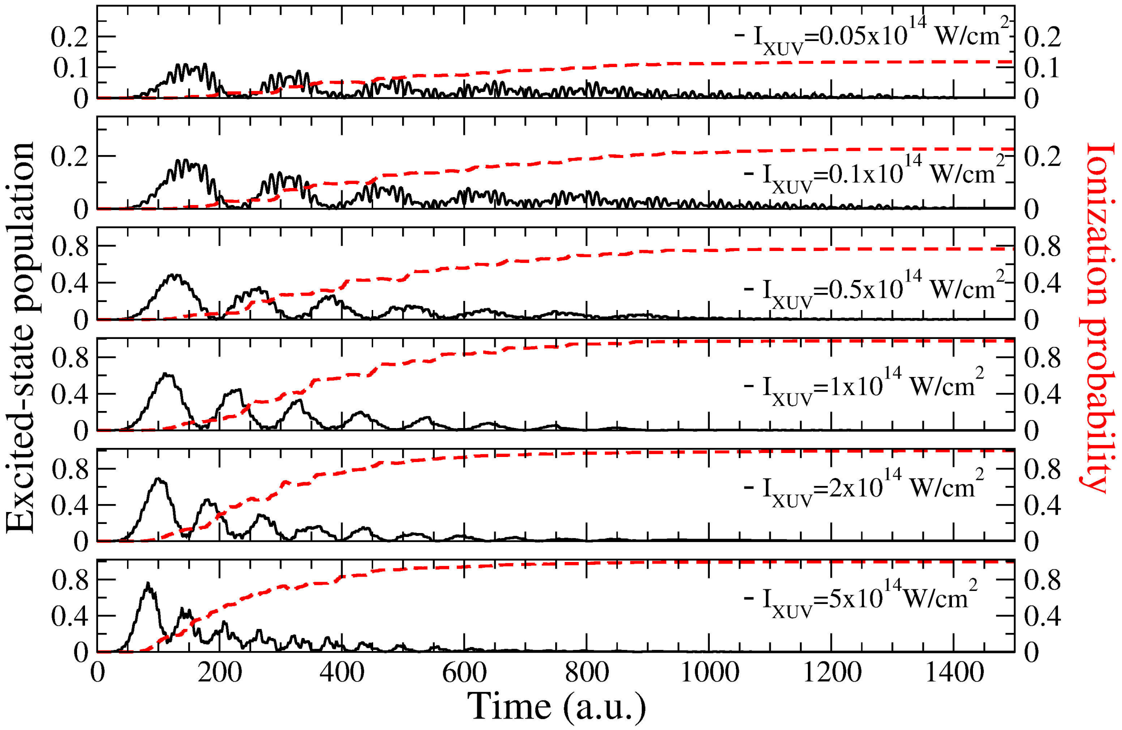

Figure 4.6: Population of the excited state (black solid curve) and the ionization probability (red dashed curve) of the system driven by combination of the IR and the XUV for various XUV pulse intensities. Parameters of the XUV fields are the following: ω_{XUV}=0.51 a.u., 80 optical cycles. IR field parameters are as described in the text.

oscillations observed in the numerical experiment with the theoretical prediction. We make the prediction using the ground-state wave function obtained by imaginary-time propagation (see Section 2.1) and the excited-state wave function found as explained in Section 4.2. With the use of the wave functions and Equation (4.14) - Equation (4.16b), we find the system parameters, such as the detuning, the transition energy Δ, the oscillation amplitude and frequency. Both values follow the theory for the XUV pulse pretty closely at low intensities of the XUV field which proves the assumption that the IR field does not strongly contribute to the Rabi frequency magnitude. The discrepancy at high XUV intensities can be explained by the Stark shift due to XUV field affecting the states position and the oscillation parameters. The theoretical curve does not take this shift into account.

HHG by combination of IR and near resonant XUV fields

Now, we investigate high harmonic generation with the XUV field ("short" or "long" pulses, see Section 4.2.3) and the IR field ($I = 5 \times 10^{13}$ W/cm^2) applied simultaneously.

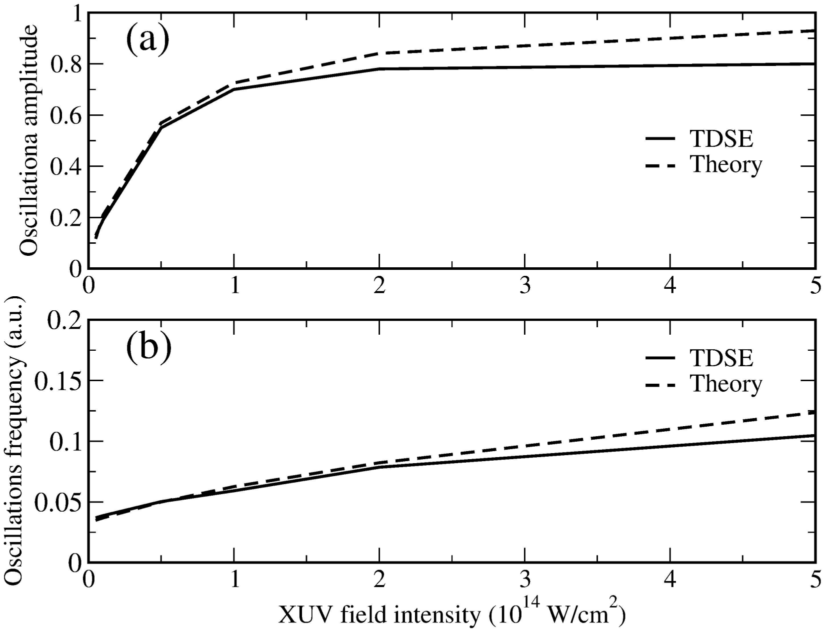

Figure 4.7: a) Amplitude and b) frequency of the Rabi oscillations in the system driven by combination of the IR and the XUV fields as a function of the XUV pulse intensity. Parameters of the XUV fields are the following: ω_{XUV}=0.51 a.u., 80 optical cycles. IR field parameters are as described in the text.

The IR field at the chosen parameters does not significantly affect the Rabi frequency. According to Equation (4.22), the Rabi frequency is $\Omega_R \approx 0.035$ a.u. and the Rabi period is $2\pi/\Omega_R \approx 180$ a.u. As it was already mentioned in Section 4.4.1, XUV$_s$ does not induce any oscillations due to its insufficient duration.

The bottom panels of Figure 4.8 show the time-resolved HHG spectra, see Equation (2.14) for the time resolution formula. The HHG spectra are obtained from the IR field assisted by the XUV pulse in case of (a) presence of the Rabi oscillations induced by XUV$_l$ and (b) decay of the excited state populated by irradiation of XUV$_s$. For comparison, the top panels illustrate the ground state population. One can see that maximum emission corresponds in time to the minima of the ground state population. The parabola-like structures of the long and short trajectories of the returning electrons are much less intense than the XUV - induced state-to-state transitions as expected.

Finally, we consider the effect of the excited-state population on the HHG spectrum. Figure 4.9 shows the HHG spectra produced by the IR field alone (black curve), XUV$_l$ alone (dotted purple curve) and in case of simultaneous irradiation of the IR and XUV fields, both for the XUV$_s$ pulse (green curve) and the XUV$_l$ pulse (red curve). We find that compared to the XUV-only case, adding the IR field helps to efficiently produce high-order harmonics in the cutoff region. The emission enhancement is more

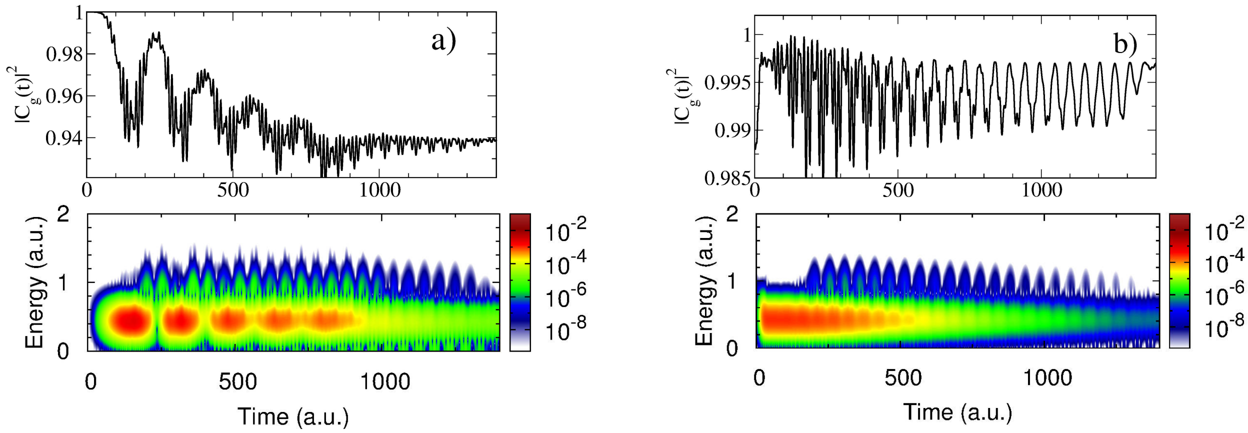

Figure 4.8: (a) Rabi oscillations driven by the "long" XUV pulse, (b) emission caused by the "short" XUV pulse.
Top: ground state population probability. Bottom: time resolved HHG spectra. Field parameters are the same as in the Figure 4.3 (a).

than 2 orders of magnitude in the peaks for the XUV$_l$ case. Compared to the IR-only case (black curve), HHG is increased by about 6-8 orders of magnitude when additionally driven by the XUV field, both for XUV$_l$ and XUV$_s$. The increase of the emission occurs due to population of the excited state by the XUV pulse and thus due to the increased probability of ionization as the first step of the three-step model. The inset of Figure 4.9 is a magnified view of the spectra, showing the exact positions of the peaks. While still being separated by $2\omega_0$, where ω_0 is the IR frequency, the peaks are found to be shifted compared to the usual odd orders (2n+1)ω_0 of the IR laser frequency.

For the short XUV pulse (green curve in Figure 4.9), relatively broad peaks are found at energies

$$\omega_n^{\text{short}} = \Delta + 2n\omega_0. \tag{4.23}$$

The XUV$_s$ pulse initially creates a superposition of ground and excited states, so that IR-driven HHG can start from the excited state and finish in the ground state, leading to peaks shifted by Δ. In order to confirm that the main effect of XUV$_s$ is the initial population of the excited state followed by ionization in the IR field, we calculate the HHG spectrum by the infrared pulse only, but in case if the initial state is the combination of the ground and excited states and the ground state contribution is like in Figure 4.3(a). Specifically, at t=0 the electron density distribution ratio between the ground and the excited states is 0.988/0.012. In Figure 4.10, the green curve corresponds to this situation. The blue curve depicts HHG by XUV$_s$ (as in Figure 4.9). One can see that the peaks positions coincide, thus one can conclude that

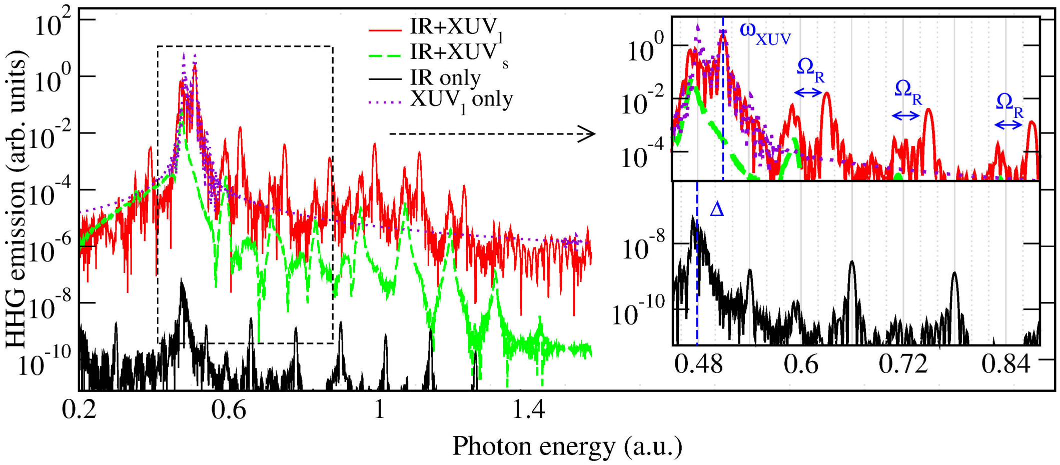

Figure 4.9: HHG spectra in the system with two bound states, produced with the IR field alone (black curve) and the combinations of the IR field with the short XUV (green curve) and long XUV (red curve) pulses. The following field parameters are used: IR: $\omega_{\mathrm{IR}} = 0.06$ a.u., $I_{\mathrm{IR}} = 5 \times 10^{13}$ W/cm^2. XUV$_l$: $\omega_{\mathrm{XUV}} = 0.51$ a.u., 80 optical cycles, $I_{\mathrm{XUV}} = 5 \times 10^{12}$ W/cm^2. XUV$_s$: $\omega_{\mathrm{XUV}} = 0.51$ a.u., 3 optical cycles, $I_{\mathrm{XUV}} = 5 \times 10^{12}$ W/cm^2. The insets show enlarged regions of the spectra.

the simulation reproduces the effect of XUV$_s$ used before the HHG-driving infrared pulse.

If the long XUV pulse is used (red curve in Figure 4.9), the dominating peaks are situated at (cf.[52,53])

$$\omega_n^{\mathrm{long}} = \omega_{\mathrm{XUV}} + 2n\omega_0 \tag{4.24}$$

as a result of converting the energy of one XUV photon and $2n$ IR photons into the energy of the emitted photon. Another effect of combining the IR field with the "long" XUV pulse is that not only the peak at ω_{XUV}, but also all the higher energy peaks are split: in addition to the dominating emission at ω_n^{long}, secondary peaks at $\omega_n^{\mathrm{long}} - \Omega_R$ are observed. The reason is the periodicity of the XUV-induced Rabi oscillations, similar as in the Autler-Townes effect.

To provide an additional proof that the splitting is indeed caused by the Rabi oscillations between the states, we calculate the HHG spectra from a potential well $\mathrm{V}_{\mathrm{1level}}$ with only one bound state. We replace α_1 and use $\alpha_1 = 0.5$ (see Table 4.1) such that the eigenstate is at -0.18 a.u and the cutoff is at 0.5 a.u. as shown in Figure 4.11. One can see that in this case the HHG peaks are situated at odd orders of the IR field frequency and are not split. If only one eigenstate exists, the presence of the weak XUV pulse does not significantly affect the HHG spectra except the additional

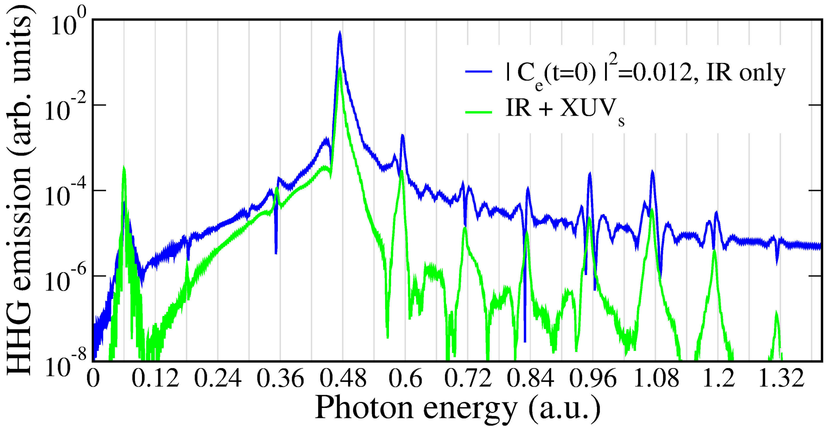

Figure 4.10: HHG spectrum in case of prepopulation of the excited state using $|C_e|^2 = 0.012$ and $|C_g|^2 = 0.988$ compared to spectrum from combined IR and XUV$_s$ fields.

emission in the region around the XUV field frequency. The spectrum resulting from the combination of XUV and IR fields resembles the sum of spectra from each of the fields.

Near resonant XUV field - influence of the pulse length

Above, we have examined two different durations of the XUV pulse: either extremely short or comparable with the IR field pulse length. Next, we explore the heights of the two peaks around 0.48 a.u. and 0.51 a.u. (Δ and ω_{XUV} for the corresponding potential) at intermediate lengths of the XUV pulse. The peak positions are chosen to investigate the splitting observed above, see, for instance, Figure 4.9. The intensity of the XUV field is $5{\times}10^{12}$ W/cm^2. The minimal considered pulse duration is longer than the Rabi oscillations period. The ratio of the peak heights for different number of optical cycles per pulse is shown in Figure 4.12. The figure shows exponential growth of the peak at 0.48 a.u. compared to the peak at 0.51 a.u. as the XUV pulse becomes longer. This is because of the number of full Rabi cycles increases, thus making the splitting more observable.

Near resonant XUV field - above threshold ionization

Here, we study the energy distribution of outgoing electrons from ionization of the system. For the infrared pulse intensity $I = 5 \times 10^{13}$ W/cm^2, the first cutoff in the above threshold ionization (ATI) spectrum is at $2U_p$=0.2 a.u. corresponding to the third harmonic of the IR field. The IR-induced Stark shift of the bound states is of

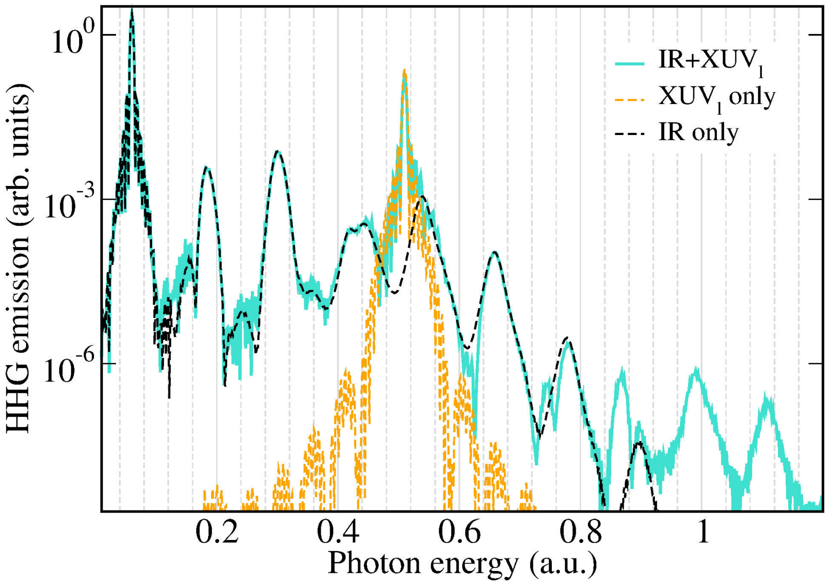

Figure 4.11: HHG spectra from a one-state system produced by the IR field (black curve) and the 80-cycles XUV pulse (orange curve) and their combination (light blue curve). The frequencies and intensities of the IR and XUV fields are as above.

the order μE_0^2 and can be considered negligible. The peaks of an ATI spectrum are at

$$E_{\mathrm{ATI}} = \mathrm{n}\omega_0 - (I_p + U_p), \tag{4.25}$$

where $\mathrm{n} \geqslant \mathrm{n}_0$, $\{\mathrm{n}, \mathrm{n}_0\} \in \mathbb{N}$ and n_0 is minimal number of photons sufficient for ionization.

Figure 4.13 shows photoelectron distribution produced by the XUV and IR pulses. If only the XUV pulse is applied, no ATI-like spectrum can be obtained due to the low intensity of the XUV field. Short XUV pulse leads to the system excitation followed by the excited state decay into the ground state. The black curve in the bottom panel of the figure corresponds to the photoelectron spectrum from the IR field only. If both XUV and IR fields are applied together, the result changes drastically. Due to the population of the excited state and following ionization from the excited state, the ATI spectrum is 5-6 orders of magnitude more intense, and the peaks are observed above the cutoff. The red and the green curves correspond to IR+XUV$_l$ and IR+XUV$_s$ as before. In both cases, free electrons outcome increases and high-order ATI peaks above the cutoff are present.

In the same figure, the solid purple curve shows the ATI spectrum from the one-state system (bound state at -0.18 a.u.) when the combined IR + XUV$_l$ field is used. The result is practically identical with the ATI spectrum from IR field only for this potential (not shown). Thus, the increase of the electron emission in the case of the

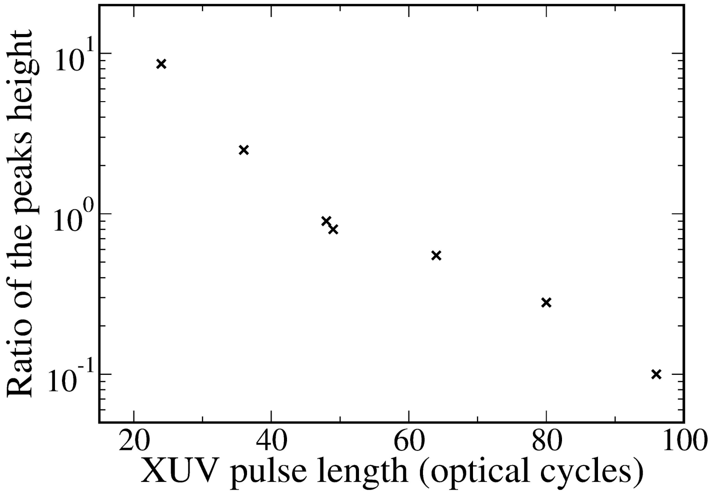

Figure 4.12: The ratio of peak heights at photon energies 0.51 a.u. and 0.48 a.u.

two-level system is associated with the population of the excited state.

The peak positions in the spectra produced by the IR field only and when assisted by XUV$_s$ or XUV$_l$ are slightly different. The origin of the difference is the state energies shift due to the AC-Stark effect.[15,36] We have discussed in the Section 4.4.1 that the infrared field does not lead to significant energy shifts. Near-resonant XUV pulse can affect the position of the states[6,36] . Condition Equation (4.20) is met despite the fact that the XUV frequency lies close to the transition frequency. From Equation (4.21) for the two-level system with the condition $|\delta| \ll \Delta$, the magnitude of the XUV-induced Stark shift is

$$|\delta\mathcal{E}_{\mathrm{XUV}}| = \left|\frac{\mu_{21}^2 E_0^2 \Delta}{2(\Delta - \omega_{\mathrm{XUV}})(\Delta + \omega_{\mathrm{XUV}})}\right| \approx \frac{\Omega_R^2 - \delta^2}{4|\delta|} \tag{4.26}$$

where the Rabi frequency is defined in Equation (4.14). The sign of the shift is defined by the sign of the detuning. Since the energy of the XUV-photon is larger than Δ, the ground state is shifted up and the excited state is shifted down[15,36] . Thus, the energy gap is increased by $\mu_{21}^2 E_0^2/(2|\delta|) = 0.002$ a.u. The peak splitting in the spectrum of XUV$_l$-assisted ATI is due to Rabi oscillations. The ATI plateau region is extended up to about 1.5 a.u. corresponding to the second ATI cutoff due to the IR field plus the energy of the XUV photon.

High-order harmonic generation at other XUV frequencies

In the literature[80–82] , it was proposed that the high-order harmonics generated by an infrared laser field can be used as an XUV source to assist the HHG process in

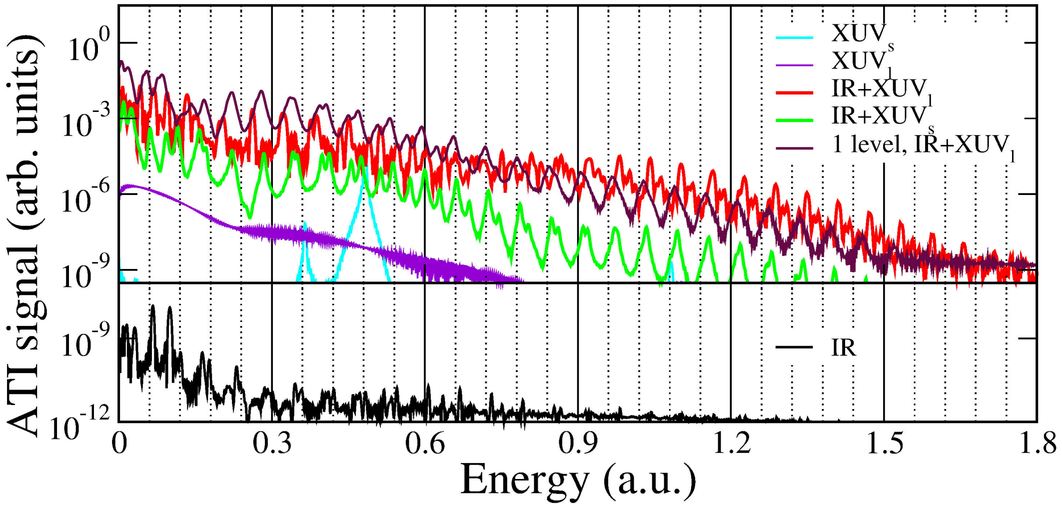

Figure 4.13: Above threshold ionization spectra. The pulse durations and field frequencies are as in Figure 4.9

the same IR beam. We investigate the HHG peak splitting for the case that the IR field is combined with a non-resonant XUV pulse. The frequencies are ω'_{XUV}=0.3 a.u. (below Δ) and ω''_{XUV}=0.66 a.u. (above Δ). ω'_{XUV} and ω''_{XUV} are the 5th and the 11th harmonics of the fundamental IR field, respectively. The condition $|\delta| \ll \Delta$ is not met and the amplitudes of the Rabi oscillations induced by the XUV field are negligible compared to the near-resonant case described above. One-photon ionization from the ground state is still not possible since

$$\omega'_{XUV}, \omega''_{XUV} < |\mathcal{E}_g| \tag{4.27}$$

The envelope of the pulse for both frequencies is trapezoidal and the duration of the XUV pulses is approximately the same as considered previously (see the methods description, Section 4.2.3). The ramps and the plateau are 6+35+6 and 13+78+13 XUV cycles for ω'_{XUV}=0.3 a.u. and ω''_{XUV}=0.66 a.u., respectively. Figure 4.14 shows the non-resonant XUV pulse assisted HHG. The emission is enhanced compared to the IR-only case despite the fact that the XUV photon is not resonant. Again, the emission growth is due to the $\mathcal{E}_g \rightarrow \mathcal{E}_e$ transition. In the off-resonant case the emission of the harmonics is 1-2 orders of magnitude weaker compared to the near-resonant HHG described above. The field intensities are the same as in Figure 4.9.

Since the frequencies of the XUV field are far from the transition energy Δ, the amplitude of Rabi oscillations is rather small. No Rabi splitting of the peaks is observed. In case of XUV_s the dominating peak is at 0.48 a.u. similarly to the case of

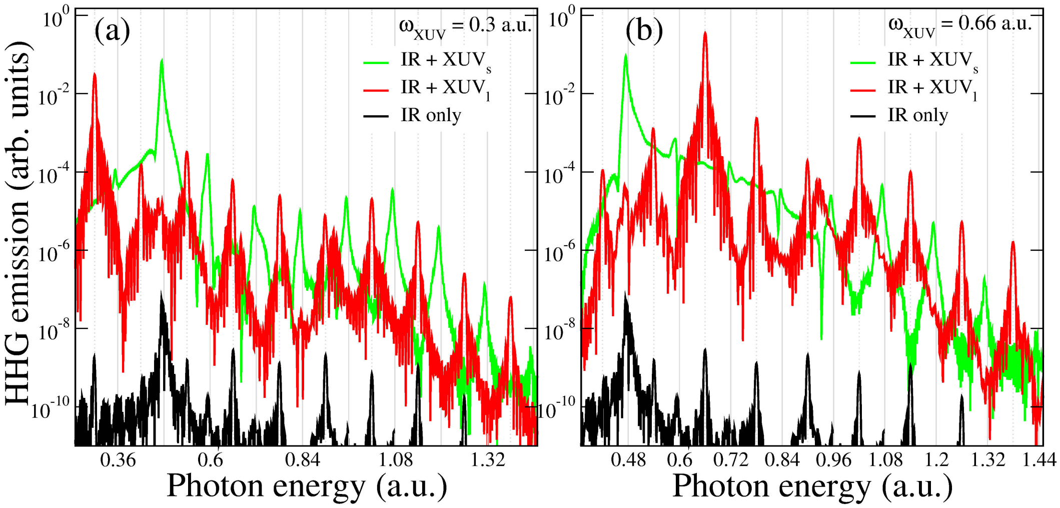

Figure 4.14: HHG spectra by a two-state system produced with the IR field only (black curve) and by combinations of the IR and the XUV fields. The XUV field frequencies are (a) the 5th and (b) the 11th harmonic orders of the IR field. The other IR field parameters and XUV field intensity are is in Figure 4.9

the resonant XUV photon described above and peaks of other orders are shifted by Δ relative to IR-only driven HHG. For XUV$_l$, the peak positions are at odd multiples of the IR laser field frequency as in case of the ordinary HHG process.

4.4.3 System with a shape resonance

In Section 4.4.2 of the current chapter we have reported the results on the enhancement of the high harmonic emission in a system with two bound states. In this section, we investigate high harmonic generation in the case that the upper state is a shape resonance. We are using the potential denoted in Section 4.2.2 as V_0^{res} and used above in Section 4.4.1. The field durations and frequencies are as described in 4.2.3 for V_0^{res}. The cutoff in the HHG spectrum at the IR field intensity 4×10^{14} W/cm^2 is expected at ≈ 3.1 a.u., i.e. above the transition energy $\Delta = 1.9$ a.u.

Influence of the XUV pulse intensity

As in the previous section, we first show the excited-state population and ionization dynamics for various XUV intensities of the long XUV pulse, see Figure 4.15. One can observe noisy oscillations, which apparently are not Rabi oscillations, because the upper state decays quickly into an ion and a free electron. The frequency of the oscillation envelope equals twice the IR frequency and does not depend on the intensity of the XUV field. Rather, the oscillations are caused by dressing of the electronic states by the

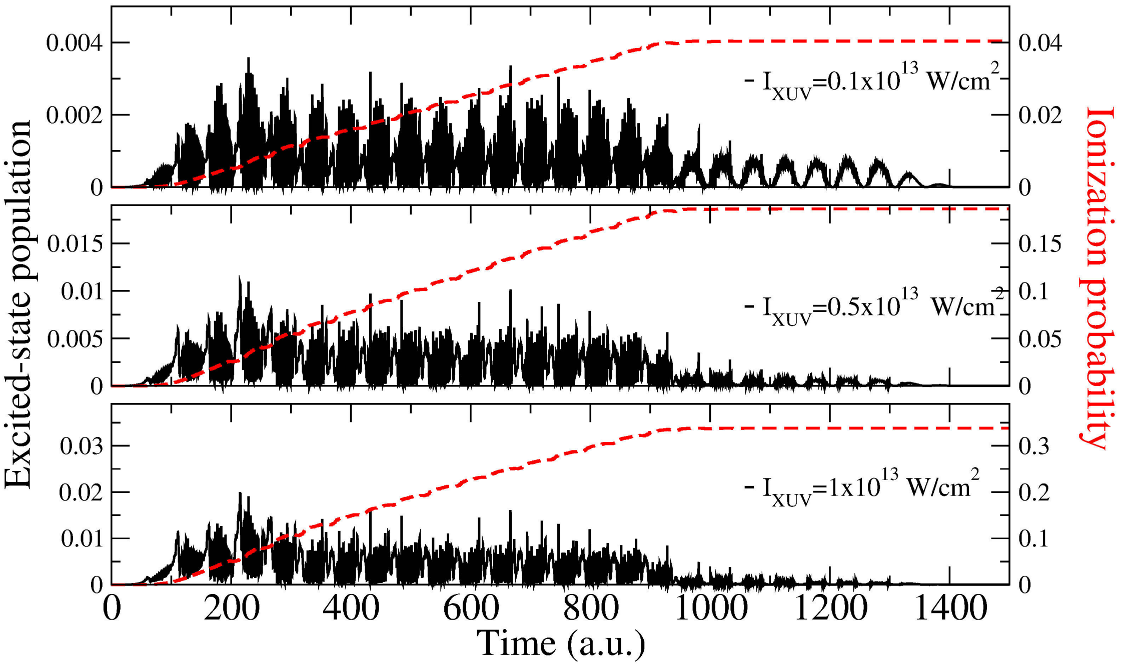

Figure 4.15: Population of the excited state (black solid curve) and the ionization probability (red dashed curve) of the system driven by combination of the IR and the XUV fields as a function of the XUV pulse intensity. Parameters of the XUV fields are the following: ω_{XUV}=0.51 a.u., 80 optical cycles. IR field parameters are as described in the text.

applied instantaneous field. From comparing the ionization probabilities in Figure 4.15, bottom panel, and Figure 4.4(b), we conclude that when the infrared field is added the ionization probability does not increase significantly, and thus the ionization is almost entirely caused by the XUV-induced excitation followed by decay of the metastable state.

IR + near resonant XUV field - HHG spectra

Here and below, we consider the intensity of the XUV field 10^{12} W/cm^2. Let us look at the time dependence of the ground-state population (top panels) and emission by the system (bottom panels) in Figure 4.16. The left and the right hand side plots correspond to the effect of XUV$_l$ and XUV$_s$, respectively. The figure proves that there are no Rabi oscillations for both field durations of the XUV pulse. In case of XUV$_l$, the main observed effect is the decay of the ground state at a constant rate. For XUV$_s$, after the XUV pulse is over, one can observe the standard picture of long and short trajectories for the system with a resonance (see Chapter 3). Figure 4.17 shows the result of the numerical simulation of high harmonic generation at the XUV intensity

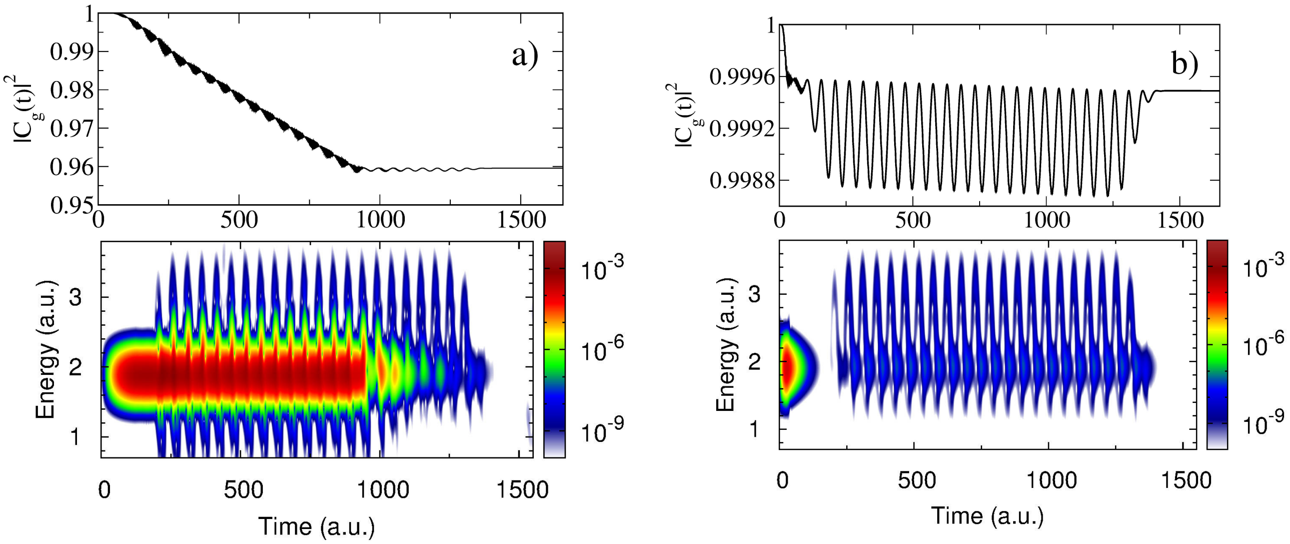

Figure 4.16: (a) Effect of the "long" XUV pulse, (b) "short" XUV pulse.
Top: ground-state population probability. Bottom: time resolved HHG spectra. Field parameters are the same as in the Figure 4.3(b).

of 10^{12} W/cm^2. The black curve is the HHG spectrum from the IR field only. The emission is in the form of odd orders of the IR frequency and it is strongest around the resonant energy $\Delta = 1.9$ a.u. When the XUV field is added, we observe the following effect. If the XUV pulse is short (XUV$_s$ case), only the resonant region emission is enhanced compared to the IR-only case. We observe a broad peak at the energy $\Delta = 1.9$ a.u. Since the metastable state decays with the lifetime 10 a.u. after it has been initially populated by the XUV$_s$ pulse, the electron emission from the excited state is not periodic, and no harmonic structure is observed. At frequencies above the resonance, the signal coincides with the IR-only HHG spectrum. If the XUV pulse is long (XUV$_l$), it causes continuous repopulation of the metastable state. The intensity of the HHG emission exceeds the IR-only spectrum by about 2-3 orders of magnitude. The peak positions are consistent with equation (4.24). There is, however, no Rabi splitting of the peaks since the lifetime of the resonance is shorter than the Rabi period.

Above Threshold Ionization

Spectra of above threshold ionization from V_0^{res} by IR and XUV fields are shown in Figure 4.18. First, we observe that applying a XUV pulse causes emission around the excited state energy due spontaneous electron emission from the metastable state. The long XUV pulse causes a narrow and high peak (purple curve); the short XUV pulse leads to a wide peak at the corresponding energy. In the ATI by the IR pulse (black

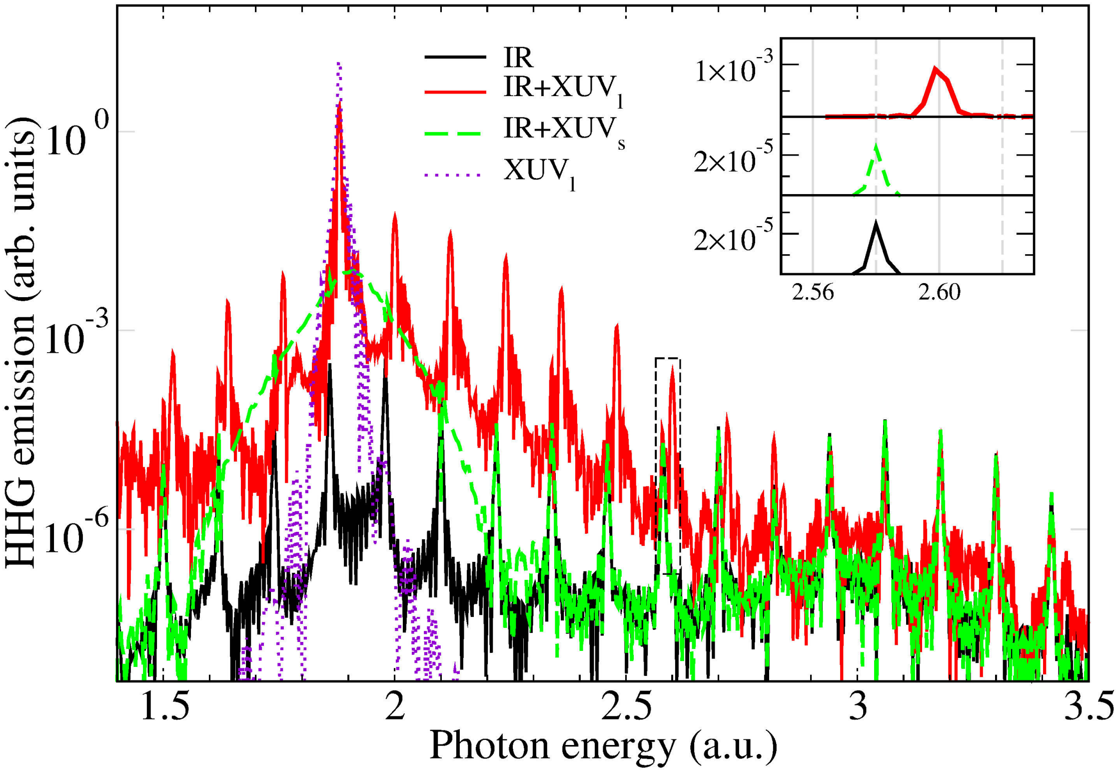

Figure 4.17: HHG spectra in a system with a shape resonance produced with the IR field alone (black curve) and the combinations IR + XUV$_l$ and IR + XUV$_s$ (see text for notation). The insets show enlarged fragments of the spectra. The field parameters are the following:
IR: ω_0 = 0.06 a.u., 14 optical cycles, I=4x10^{14} a.u.
XUV$_l$: ω_{XUV} = 1.88 a.u., 295 optical cycles, I=10^{12} a.u.
XUV$_s$: ω_{XUV} = 1.88 a.u., 11 optical cycles, I=10^{12} a.u.

curve in the figure), the two ATI cutoffs are at $2U_p$=1.6 a.u. and $10U_p$=7.9 a.u. as expected. Applying a short XUV pulse had no effect outside of the resonant region (the ATI spectrum basically coincides with the ATI spectrum by the IR field) and increased the emission around $\mathcal{E}_{\text{res}}$, again, because of the resonance decay. Using the long XUV pulse allowed to increase the output by 2-3 orders of magnitude due to the above threshold ionization of the resonant state occurring with higher probability. The peak around $\mathcal{E}_{\text{res}}$ is missing and thus ATI is the dominant process as to compare to electron emission from $\mathcal{E}_{\text{res}}$ through the potential barrier.

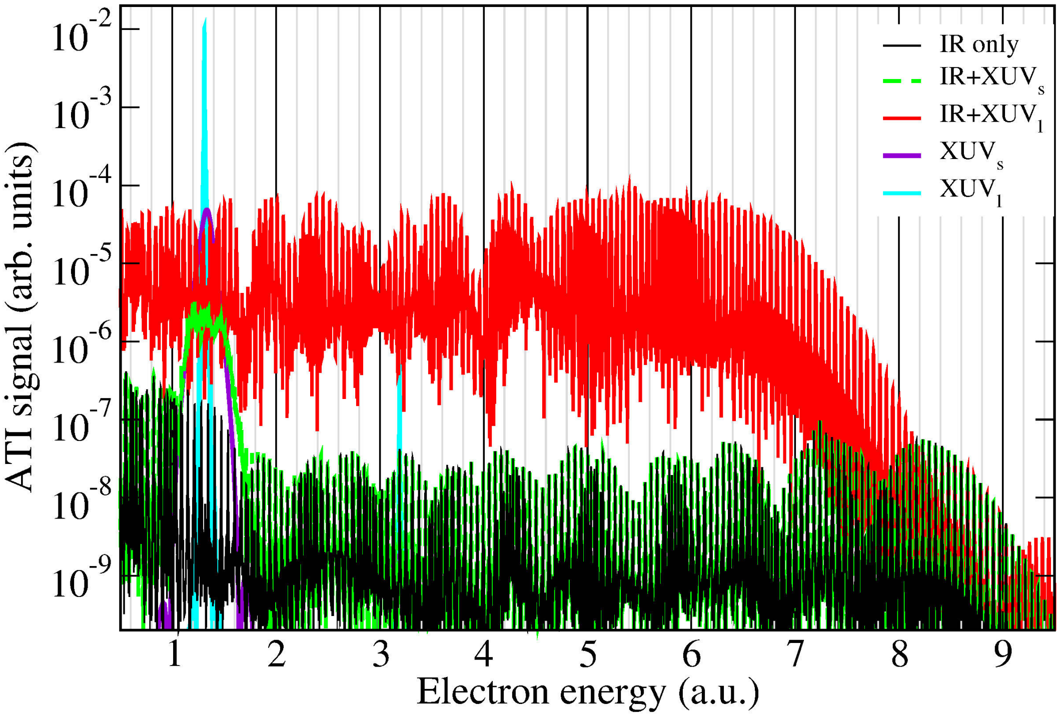

Figure 4.18: Above threshold ionization spectra from the combination of the IR and the XUV fields. The parameters of the fields and the notation are as in the Figure 4.17.

4.5 Discussion

In conclusion to this chapter, we have investigated the generation of high harmonics and, additionally, above threshold ionization driven by an infrared field when assisted by an extreme ultraviolet field. We have shown that in a quantum system with a bound or metastable excited electronic state, adding a moderate near-resonant XUV pulse can lead to enormous enhancement of the HHG and ATI emission due to XUV-induced population of the excited state, from which the IR field can drive HHG more easily than from the ground state. The resulting radiation exceeds both the signal from IR-only and from XUV-only fields. In the harmonic generation process, the positions of the peaks are shifted away from odd orders of the IR frequency. The details of the resulting HHG spectrum depend on the lifetime of the excited state. If the XUV pulse is sufficiently long and the excited-state lifetime is longer than the corresponding Rabi period, Rabi splitting of the harmonic peaks is observed in the HHG spectrum.

Chapter 5

Extreme ultraviolet frequency combs

One of the most promising methods of laser-based high-precision spectroscopy is a spectral “ruler”, namely frequency combs. It is a reliable and relatively inexpensive tool which allows to resolve frequencies with incredible accuracy. The essential idea of a frequency comb (FQ) is the following: using a train of laser pulses that are identical except for a slip in the carrier-envelope phase leads to a set of narrow peaks in the energy domain centered around the laser frequency. According to the properties of the Fourier transform, the time shift between the pulses defines the interval between the peaks in the energy domain, thus providing a link between different frequency regions, for instance, between microwave and optical frequencies. Peaks are separated by the repetition frequency $\omega_r = 2\pi(\text{repetition period})^{-1}$. Typically, the repetition frequency is of the order $10^2 - 10^3$ MHz. While the “ruler” itself has to be rather wide, every tooth should be an extremely narrow line to be of use in spectrometry.

For precision spectroscopy of transitions in the XUV range in atoms and molecules narrow bandwidth radiation is desirable. Currently existing systems do not meet the requirement of having a narrow bandwidth for each mode. Transferring frequency-laser fields comb to the extreme ultraviolet via intra-cavity HHG is a possible key to the problem of direct frequency comb spectroscopy. A train of mode-locked pulses can be applied to a gas medium to generate high harmonics, each being a frequency comb. For the comb to be useful, the positions of the teeth should be predictable. In this chapter, we discuss the results of numerical simulation of XUV frequency combs generation by pulse trains. It turns out that the duration of a pulse is crucial and defines the comb modes. In case of few-cycle pulse producing overlapping harmonics in the HHG spectrum, the properties of the comb change. The structure of such combs and in particular the spacing between the teeth is investigated below.

5.1 Previous work

Theodor W. Hänsch and John L. Hall shared the Nobel Prize in Physics in 2005 for their work that started in the end of the 1970s that led to remarkable results in the late 1990s (see, for example, the papers of Salomon, Hills, Hall[131] and Eckstein, Ferguson, Hänsch[41]) , where the authors showed to achieve the desirable stability by locking the laser frequency to sharp interference fringes[144] . Frequency combs are used in such applications as, for example, spectroscopic calibration[38] , atomic clocks[20,39,143] or measuring frequencies of the transitions in atoms and molecules[1] .

Despite the simplicity of the idea of frequency combs, experimentally it has been a challenge to obtain them and detect the field parameters. The first positive results are reported in the end of the 1990s - beginning of the 2000s[31,39,79,147] . Even though the pulses in the pulse train of a mode-locked laser were not identical, physicists were able with the help of Kerr lens to stabilize the carrier envelope phase (CEP)[32] , thus reaching the goal of creating a comb. Traditionally, Ti:sapphire, Yb:fiber and Er:fiber laser systems are used in the experiments. In an optical cavity, light bounces between the mirrors, such that the geometry of the system defines the repetition rate. Currently existing technologies allow to produce frequency combs with broad bandwidth as they use laser pulses as short as a few femtoseconds[126] . Pulses within the train are nearly identical, except that the carrier envelope phase changes from pulse to pulse by so called offset phase. While detecting the repetition frequency is not problematic, measuring the offset is more difficult. For detecting the offset phases, the self-referencing technique was invented. In this method, a tooth from the low-frequency side of the spectrum is doubled with the use of second harmonic generation. In order to identify the CEP, beating between the resulting tooth and a tooth from the high-frequency side of the spectrum is considered. Such a technique is possible because the comb bandwidth is as broad as an octave of the spectrum[87] .

Taking the comb to the XUV region by generation of high harmonics would be essential for molecular spectroscopy[108] since other existing XUV sources do not have sufficiently narrow peaks at each mode. Also, the necessary source power must be a few orders of magnitude higher for a XUV laser than for a laser in a visible spectral range. It can be explained, for instance, with the scaling argument stating that the spontaneous emission must occur with lower rate than the excitation[156] . It is not possible to create a frequency comb with the existing sources XUV radiation because highly reflective mirrors in this wave range are not available[71] . High intensities required in HHG traditionally are achieved by reducing the repetition rate and thus number of pulses per train. The repetition rate turns out to be too low to produce a useful comb, and the teeth are too close to each other. The so called enhancement-cavity-assisted HHG was proposed to advance the XUV frequency comb[88] . A coherent XUV frequency comb obtained by means of intra-cavity HHG at a repetition frequency exceeding 100 MHz was reported by Gohle *et al.*[70,71] . The coherence was tested in a beat experiment between certain harmonics from the enhancement cavity and mode-locked laser. Further progress led to direct frequency comb spectroscopy measurement in neutral argon[156] . An alternative way of generation a quasi-comb in the XUV region was proposed by Raith *et al.*[125] . Instead of using a pulse train the authors propose to apply so called split-spectrum pulse control. A single broadband laser pulse was spectrally resolved and then divided into two parts and coherently shaped by introducing a time delay between the two sections. Thus, two attosecond HHG spectra were obtained and then interfered leading to formation of a quasi-comb.

When analyzing the resulting XUV FQ, it is important to determine temporal coherence of the spectrum. In order test the temporal coherence, traditionally, the beating between two light sources is measured. In case of ordinary high harmonic emission from a single pulse, two copies of the same HHG pulse are produced with certain time delay and beating between them is measured[13] .

In case of XUV frequency combs through HHG, significant progress was reported in 2012 by Cingös *et al.*[28] . The intensity enhancement was achieved by coupling IR frequency combs with a robust femtosecond enhancement cavity. The authors reported that the resulting combs were sufficient to observe single-photon spectroscopy signals for transitions in argon and neon and that they have determined the absolute frequency of the argon transition by direct FQ spectroscopy.

Despite rather intense study of the topic and significant advancement in the last years, few theoretical papers have been dedicated to the problem. Numerical simulations of XUV frequency combs and calculations of teeth phases, ionization probabilities and the dependence on the number of pulses have been reported by Carrera *et al.*[22] . In the study, the results were found by numerical solution of the TDSE. The authors found that each of the harmonics contains a comb-like structure originating from quantum interferences among induced dipole pulses. The same group employed time-dependent density-functional theory to calculate XUV frequency combs from helium atoms[21] . It was shown that for super-intense pulses significant and uneven ionization between pulses can ruin the frequency comb coherence in the single-atom regime and affect phase matching[21] , while the effect does not take place for pulses with moderate intensity. In a recent paper, Zhao *et al.* used the many-mode Floquet theory treating the situation as a non-Hermitian generalized Floquet matrix eigenvalue problem and employed it for the calculation of HHG and MPI by atomic hydrogen[157] .

5.2 Methods

The approach to the numerical solution of the TDSE was discussed before in Chapter 1 (see Section 2). Here, we used a consider one-dimensional model and employ the 1D soft-core potential

$$V_0(x) = -1/\sqrt{x^2+\xi^2}, \tag{5.1}$$

with ξ=1.175 such that the ground state is at -0.58 a.u. (which corresponds to the ionization potential of argon).

Below, the field of each pulse has a trapezoidal or $\sin^2$ envelope, intensity 2×10^4 W/cm^2 and optical frequency ω_0=0.06 a.u. We did not use realistic parameters for the repetition rate since it is not important for our conclusions, and the majority of the plots are shown in units of the repetition frequency, ω_r. Instead, the repetition period is in the range $\tau_r < 100T_0$, where T_0 is the optical cycle. To obtain the comb, we calculate the dipole acceleration $a_m(t)$ independently for each pulse number, m, and each CEP. Let us say that each pulse consists of N optical cycles. We propagate the wave function for $N+2$ cycles and assume the dipole acceleration to be zero from $(N+2)T_0$ to τ_r,

$$a_m(t) = \begin{cases} a_m^{\mathrm{TDSE}}(t), & t \in [0,(N+2)T_0] \\ 0, & t \in [(N+2)T_0, \tau_r]. \end{cases}$$

The final dipole acceleration is calculated as the sum over all M pulses:

$$a(t) = \sum_{m=0}^{M-1} a_m(t - m\tau_r). \tag{5.2}$$

As usual, the spectrum is found as the square of the absolute value of the dipole acceleration Fourier transform.

5.3 The concept of frequency combs

5.3.1 Frequency combs by a pulse train

In real systems, the pulses in the train cannot be exactly identical since their carrier-envelope phase (CEP) is difficult to adjust to be the same due to the intra-cavity dispersion. The carrier envelope phase can be stabilized so that it changes from pulse to pulse in a predictable way. The pulse offset phase $\delta\phi$ is associated with the offset frequency, ω_{off}, as

$$\omega_{\text{off}} = \omega_r \frac{\delta\phi}{2\pi} = \frac{\delta\phi}{\tau_r}, \tag{5.3}$$

where τ_r is the repetition period. Let $\phi_m = \phi_0 + m\delta\phi$ be the phase shift of the m^{th} pulse in the mode-locked pulse train and $t_m = m\tau_r$ is the time when the m^{th} pulse begins. We use Equation (5.3) and assume that ϕ_0=0. The field of the m^{th} pulse is

$$E_m(t) = f(t)\mathrm{e}^{-i(\omega_0 t+\phi_m)} = f(t)\mathrm{e}^{-i(\omega_0 t+m\omega_{\text{off}}\tau_r)} + c.c. \tag{5.4}$$

The resulting electric field written as a sum of the contributions from M pulses is

$$E_T(t) = \sum_{m=0}^{M-1} E_m(t-t_m) = \sum_{m=0}^{M-1} f(t-t_m)e^{-i(\omega_0 t-\omega_0 t_m+\phi_m)} + c.c., \tag{5.5}$$

where ω_0 is the optical laser frequency and $f(t)$ is the pulse envelope. Due to the complex conjugate term, the Fourier transform of the field contains terms for positive and negative frequencies. Only the term for positive frequencies is physical. We denote it $\tilde{E}_T(\omega)$ and substitute the integration variable $\tau = t - m\tau_r$, so that

$$\tilde{E}_T(\omega) = \sum_{m=0}^{M-1} \int dt\, e^{i\omega t} f(t-m\tau_r)e^{i(-\omega_0 t+m\omega_0\tau_r-m\omega_{\text{off}}\tau_r)} = \tag{5.6a}$$

$$= \sum_{m=0}^{M-1} e^{im(\omega-\omega_{\text{off}})\tau_r} \int d\tau\, e^{i(\omega-\omega_0)\tau} f(\tau) = \tag{5.6b}$$

$$= \tilde{f}(\omega-\omega_0) \sum_{m=0}^{M-1} e^{im(\omega-\omega_{\text{off}})\tau_r}, \tag{5.6c}$$

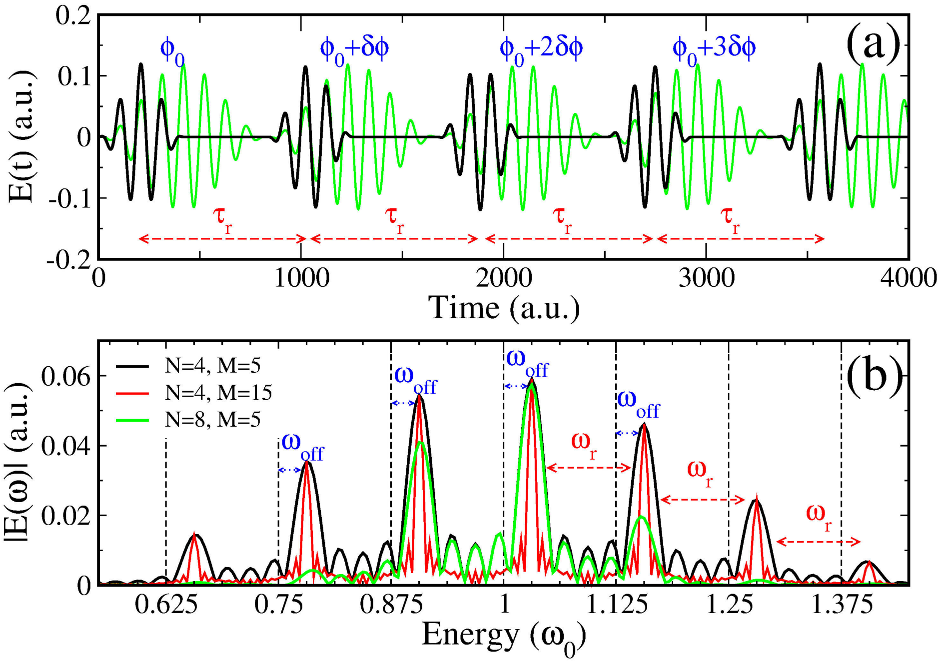

Figure 5.1: Examples of (a) pulse trains fragments and (b) the corresponding frequency combs in the energy domain. N - number of optical cycles per pulse, M - number of pulses in a pulse train, the envelope has $\sin^2$ shape, τ_r=8 T_0, where T_0 is the optical cycle. The integration time period is 256 T_0. The phase shift $\delta\phi = \pi/2$, $\phi_0 = \pi/2$.

where $\tilde{f}(\omega)$ is the Fourier transform of $f(t)$. After calculating the geometric sum in Equation (5.6c), we have

$$\tilde{E}_T(\omega) = \tilde{f}(\omega-\omega_0)\frac{1-\mathrm{e}^{i(\omega-\omega_{\text{off}})M\tau_r}}{1-\mathrm{e}^{i(\omega-\omega_{\text{off}})\tau_r}} = \tag{5.7a}$$

$$= \tilde{f}(\omega-\omega_0)\frac{\sin[(\omega-\omega_{\text{off}})M\tau_r/2]}{\sin[(\omega-\omega_{\text{off}})\tau_r/2]}\mathrm{e}^{i(\omega-\omega_{\text{off}})(M-1)\tau_r/2}. \tag{5.7b}$$

The final expression for the field spectrum is

$$P(\omega) = |\tilde{E}_T(\omega)|^2 = |\tilde{f}(\omega-\omega_0)|^2\frac{1-\cos[(\omega-\omega_{\text{off}})M\tau_r]}{1-\cos[(\omega-\omega_{\text{off}})\tau_r]}, \tag{5.8}$$

Figure 5.1 shows pulse train examples and the corresponding frequency combs. In the energy domain, we normalized the envelope function by dividing by the overall number of optical cycles of non-zero field. Increasing the number of pulses per train leads to more narrow peaks, while increasing the number of optical cycles per pulse constricts the envelope bandwidth. The pulse spectrum envelope is centered around ω_0. $P(\omega)$ has a comb structure, and the local maxima, i.e. comb teeth, are at frequencies ω_k

with

$$\omega_k = \omega_{\text{off}} + k\omega_r, \quad k \in \mathbb{Z}, \tag{5.9}$$

One can say that the pulse train spectrum consists of infinite number of spectral contributions corresponding to Equation (5.9). This statement means that we can write Equation (5.7) as

$$\tilde{E}_T(\omega) = \tilde{f}(\omega - \omega_0) \sum_k \tilde{W}_k(\omega), \quad k \in \mathbb{Z},, \tag{5.10a}$$

where $\tilde{W}_k(\omega) = \tilde{W}(\omega - \omega_k)$ is a function that covers only the region around he maximum at $\omega = \omega_k$. After the reverse Fourier transform the functions product turns into their reverse Fourier transform convolution, $F^{-1}(\tilde{f}(\omega - \omega_0)) \propto \mathrm{e}^{-i\omega_0 t}$ and $F^{-1}(\tilde{W}(\omega - k\omega_r - \omega_{\text{off}})) \propto \mathrm{e}^{-i(k\omega_r + \omega_{\text{off}})t}$. Thus, in the time domain, the k^{th} component of the field of a pulse train is proportional to the convolution of two oscillating functions with different frequencies and envelopes, and

$$E_k(t) \propto f(t)\mathrm{e}^{-i\omega_0 t} * W(t)\mathrm{e}^{-i\omega_{\text{off}} t}\mathrm{e}^{-ik\omega_r t},\ \ k \in \mathbb{Z}. \tag{5.11}$$

5.3.2 Frequency combs in the extreme ultraviolet spectral range

By exposing atoms to an intense pulse train, it is possible to produce an XUV frequency comb by means of high harmonic generation.

Let as first consider HHG by a single pulse. The field frequency is ω' and the pulse envelope is $g(t)$, high harmonics are emitted periodically. The period of an optical cycle is $T' = 2\pi/\omega'$ and an attosecond pulse is produced with a period $T'/2$, once during the positive half-cycle and then during the next half-cycle when the field is negative. We assume that the shapes of the individual attosecond pulses emitted during each half-cycle of the driving field are identical. This assumption does not hold in a general case, but can be made for long pulses. The function describing the shape of an individual attosecond pulse is $\alpha_0(t)$. The resulting emission is

$$E_{\text{HHG}}(t) = \sum_{n=0}^{N-1} (\alpha_0(t - nT') - \alpha_0(t - nT' - T'/2)),\ n \in \mathbb{N}, \tag{5.12}$$

where we take into account that the driving field as well as the emitted pulses change

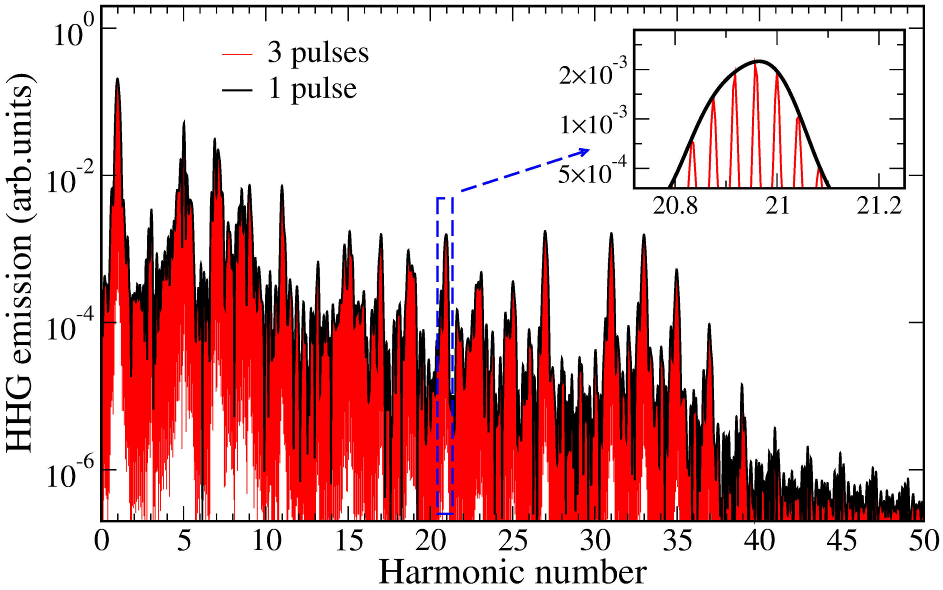

Figure 5.2: Numerical simulation: I = 2 × 10^{14} W/cm^2, τ_r=8 T_0, ϕ_0=0, $\delta\phi = 0$. The red and black curves describe HHG from a single pulse and a train of three pulses.

the sign within each half-cycle $T'/2$. Performing the Fourier transform, taking into account the convolution theorem and using the properties of the geometric sum we get for the HHG spectrum

$$S(\omega)_{\mathrm{HHG}} = |\tilde{E}_{HHG}(\omega)|^2 = \tag{5.13a}$$

$$= \left| \tilde{\alpha}_0(\omega)(1 - e^{i\omega T'/2}) \sum_{n=0}^{N-1} \mathrm{e}^{i\omega n T'} \right|^2 = \tag{5.13b}$$

$$= \left| \tilde{\alpha}_0(\omega) \frac{1 - \mathrm{e}^{i\omega N T'}}{1 - \mathrm{e}^{i\omega T'}} (1 - e^{i\omega T'/2}) \right|^2 . \tag{5.13c}$$

The spectrum contains local maxima at odd orders of the driving frequency,

$$\Omega_{\mathrm{HHG},\omega'} = (2\nu + 1)\omega', \nu \in \mathbb{N}, \tag{5.14}$$

i.e. the position of the HHG peaks is the result of the driving field periodicity. The doubled frequency spacing appears due to the term $T'/2$ in the sum in Equation (5.13).

If the field is a pulse train, the k^{th} spectral term from Equation (5.10) contributes to the HHG spectrum, $\omega' = \omega'(k) = \omega_{\mathrm{off}} + k\omega_r$. In high harmonic generation by a pulse train, the teeth are harmonics of $\omega'(k)$, where k goes over all range of possible values. Due to nonlinearity of the process, the final HHG spectrum is not just a sum of contribution from each field peak. For harmonic number $2\nu + 1$, the teeth turn

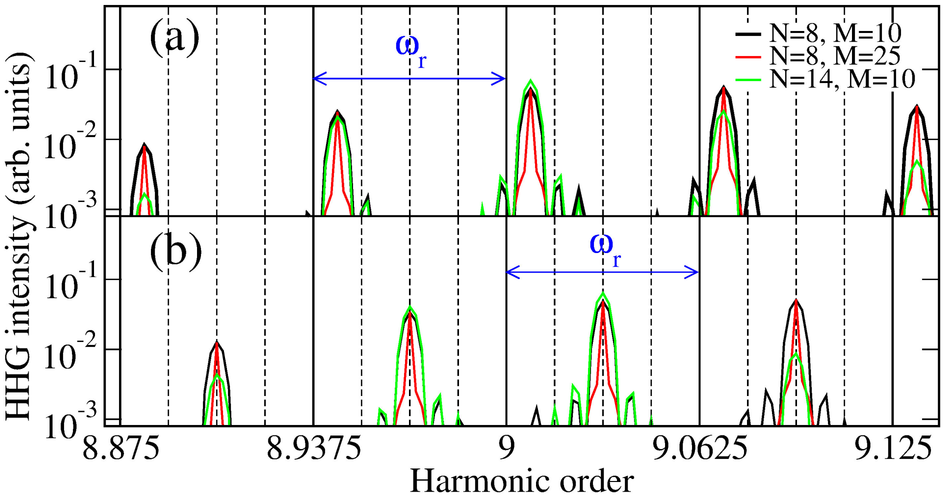

Figure 5.3: XUV frequency comb via HHG. N - number of optical cycles per pulse, M - number of pulses in a pulse train. Each pulse has a trapezoidal envelope, ramp length is T_0, the pulse duration is equal to the repetition period, $\tau_r = 16T_0$. (a) $\delta\phi = \pi/4$, (b) $\delta\phi = \pi/3$. The emission amplitude is divided by the overall number of optical cycles of non-zero field

out to have an offset shift $(2\nu + 1)\omega_{\mathrm{off}}$. The teeth positions are given by the following expression

$$\Omega_q^{2\nu+1} = (2\nu + 1)\omega_{\mathrm{off}} + q\,\omega_r, \;\; \nu \in \mathbb{N},\; q \in \mathbb{Z}. \tag{5.15}$$

The envelope of the spectrum is defined by the atomic high harmonic generation process and has peaks at odd multiples of the driving frequency, ω_0, as normally. In case of zero offset, the resulting spectrum envelope coincides with the HHG spectrum from a single pulse as shown in the Figure 5.2.

Figure 5.3 shows HHG spectra around the 9^{th} harmonic from a pulse train for two different carrier envelope offset phases and $\tau_r = 16T_0$. Combining Equation (5.3) and Equation (5.15) and considering $q\omega_r = 144\omega_r + q'\omega_r = 9\omega_0 + q'\omega_r$ with $q, q', q'' \in \mathbb{Z}$, we find the teeth positions:

$$\Omega_q^9 = \begin{cases} (\frac{9}{8} + q)\omega_r = 9\omega_0 + (\frac{1}{8} + q'')\omega_r, & \delta\phi = \pi/4 \\ (\frac{3}{2} + q)\omega_r = 9\omega_0 + (\frac{1}{2} + q'')\omega_r, & \delta\phi = \pi/3. \end{cases}$$

Figure 5.3 also shows that longer pulse trains lead to more narrow comb teeth. Increasing the number of optical cycles per pulse leads to a smaller envelope bandwidth of each harmonic order. Below, we will analyze numerical results of TDSE simulation in the case when the pulses are short and harmonics of different orders overlap.

5.4 XUV frequency combs as a function of the driving field parameters

Case of zero phase shift

If there is no phase shift between the pulses in the train, $\omega_{\text{off}}=0$, then in accordance to Equation (5.15),

$$\Omega_q^{2\nu+1} = q\omega_r. \tag{5.16}$$

Equation (5.16) means that regardless of the harmonic order, the teeth are at multiples of the repetition frequency, and all the teeth positions coincide for different ν. In such a case the comb structure is obviously preserved.

Figure 5.5 (a) is an example of HHG emission by a train with zero offset phase and shows the spectrum around the 23^{rd} harmonic. One observes a comb of equidistant teeth.

XUV frequency comb from a train of ultrashort pulses

We have previously concluded that if all high harmonic orders can be easily distinguished, the resulting structure can be considered as series of harmonic peak envelopes. The spectral function under the envelope curve has a comb structure corresponding to a specific harmonic order. If the laser pulse is very short, harmonic orders cannot be identified clearly. Instead, the spectrum tends to become a continuum and comb structures from harmonics of different orders overlap. If the CEP changes from pulse to pulse, the distance between closest teeth of the comb is no longer just ω_{r}. Because of the overlapping harmonics, intermediate teeth, originating from neighboring harmonics, should be expected. When considering a certain harmonic order, say, $2\nu+1$, we will refer to the teeth from $2\nu-1$ or $2\nu+3$ harmonic orders as "side teeth".

Let us consider harmonics of the orders $2\nu+1$ and $2\nu+3$. We assume that $\delta\phi \in (0,\pi]$ and that it can be represented as a fraction of π,

$$\delta\phi/\pi = (N_1/N_2),\ N_1, N_2 \in \mathbb{N}. \tag{5.17}$$

With Equation (5.15), the distance between teeth from the two harmonics is

$$\Delta\Omega^{2\nu+1,2\nu+3} = 2\omega_{\text{off}} + Z\omega_r = (N_1/N_2 + Z)\omega_r,\ N_1, N_2 \in \mathbb{N}, Z \in \mathbb{Z}. \tag{5.18}$$

The two closest of the teeth are separated by

$$|\Delta\Omega^{min}| = (N_1/N_2)\omega_r,\ \text{ if }\ \delta\phi < \pi/2, \tag{5.19a}$$

$$|\Delta\Omega^{min}| = (1 - N_1/N_2)\omega_r,\ \text{ if }\ \delta\phi \geq \pi/2. \tag{5.19b}$$

If $\delta\phi > \pi$, in the conclusion we should replace N_1/N_2 with the remainder $(N_1/N_2) - \lfloor N_1/N_2 \rfloor$, where $\lfloor\ \rfloor$ stands for the floor function.

If not only adjacent odd harmonics interfere, the conclusion can be generalized. In general,

$$|\Delta\Omega^{min}| = |(Z'N_1/N_2 + Z)\omega_r|^{min},\ N_1, N_2 \in \mathbb{N}; Z, Z' \in \mathbb{Z};\ Z \neq 0. \tag{5.20}$$

The absolute minimum is reached if can be found Z, Z' such that $Z'N_1 + ZN_2 = 1$. In this case the distance between the closest peaks will be $(1/N_2)\omega_r$.

The effect of overlapping peaks is shown in the Figure 5.4, where we compare XUV frequency combs via HHG from a train consisting of long pulses and a train consisting of few-cycle pulses. The horizontal axis represents an interval around $9\omega_0$. The distance between major ticks of the horizontal axis is $\omega_r = \omega_0/40$, the minor ticks divide it to N_2 segments, see notation in Equations (5.19), (5.20). The two trains have otherwise the same parameters (see figure caption). The long pulses produce dominating teeth separated by ω_r (red curves) and the 9-photon process significantly dominates over the contribution from other harmonics. The train of ultra-short pulses results with a more dense comb (black curves) where teeth from harmonics of different orders have the same height as teeth from the 9^{th} order. The black curves in panels (a)-(c) show the contribution from neighboring odd harmonic orders. In panels (a), (c) the CEP shift equals π divided by an integer and does not exceed $\pi/2$, so the teeth positions can be described described by Equation (5.19a). In panel (b), the phase shift is $\delta\phi_b = \pi - \delta\phi_a > \pi/2$ with $\delta\phi_a$ being the phase shift used in (a). Thus the distance between the teeth is the same as in (a) and described by Equation (5.19b). In panel (d), the phase shift is $\delta\phi_d = 2\pi/7$ and the closest peaks are separated by $\pi/7$ as described by Equation (5.20). This is possible, for example, $Z' = -3, Z = 1$, i.e. interference of at least four odd harmonics can be observed.

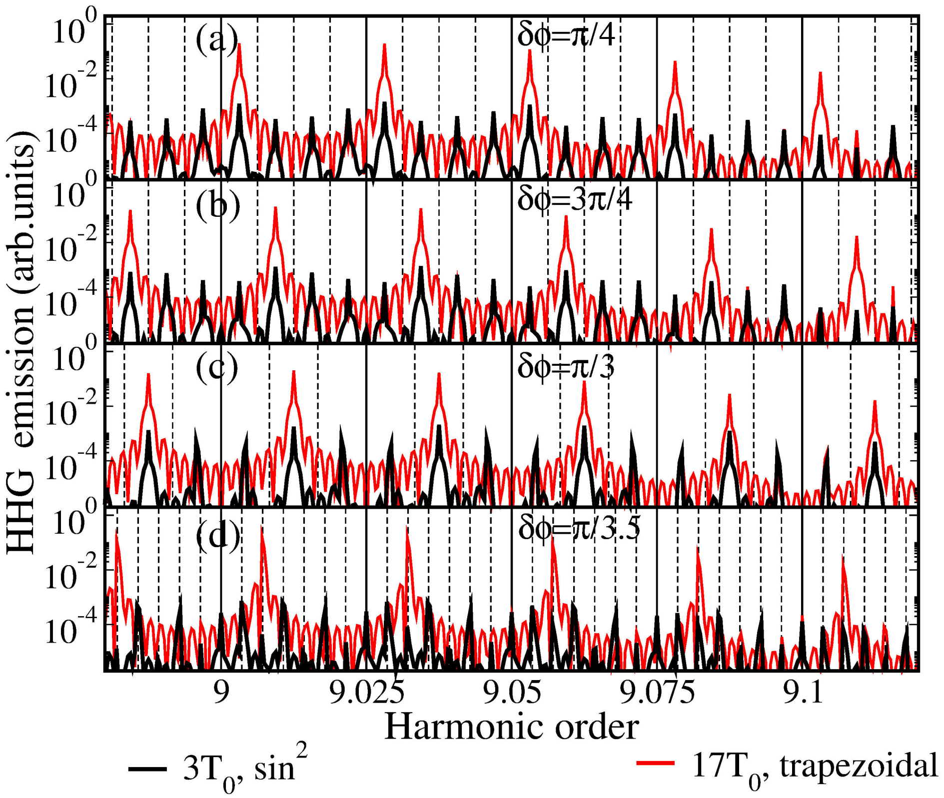

Figure 5.4: XUV frequency comb from HHG using trains of 50 long (red curve) or 50 short pulses (black curve). The long pulse has trapezoidal envelope (2+13+2 T_0 long); the short pulse has $\sin^2$ envelope (3 T_0 long) and τ_r=40 T_0. (a) $\delta\phi = \pi/4$, (b) $\delta\phi = 3\pi/4$, (c) $\delta\phi = \pi/3$, (d) $\delta\phi = \pi/3.5$. The spectra are normalized as in Figure 5.3

XUV frequency comb "transparency"

Another interesting feature of the HHG spectrum produced by the pulse train is its "transparent" structure. Since different harmonic orders consist of XUV frequency combs with different offset frequency, we should be able to see the overlap between orders when plotting the overall spectrum. Figure 5.5 illustrates the idea. In panel (b), the offset phase is π, thus the shift between teeth from harmonic orders $2\nu + 1$ and $2\nu + 3$ is ω_r and we cannot distinguish between different odd harmonic orders, although at the bottom of the spectrum we observe the negligible contribution from even harmonics (compare to panel (a), where pulses have zero offset phase and the HHG spectrum is just a comb of evenly spaced teeth). As pulse-to-pulse phase shift is varied, we see that the density of teeth increases. If $\delta\phi = \pi/2$, we can see the interference of combs from two odd harmonics, $2\nu + 1$ and $2\nu + 3$ (as well as two neighboring even harmonics at the bottom of the spectrum). If $\delta\phi = \pi/4$, we recognize overlapping of combs from harmonic $2\nu + 1$ up to $2\nu + 7$.

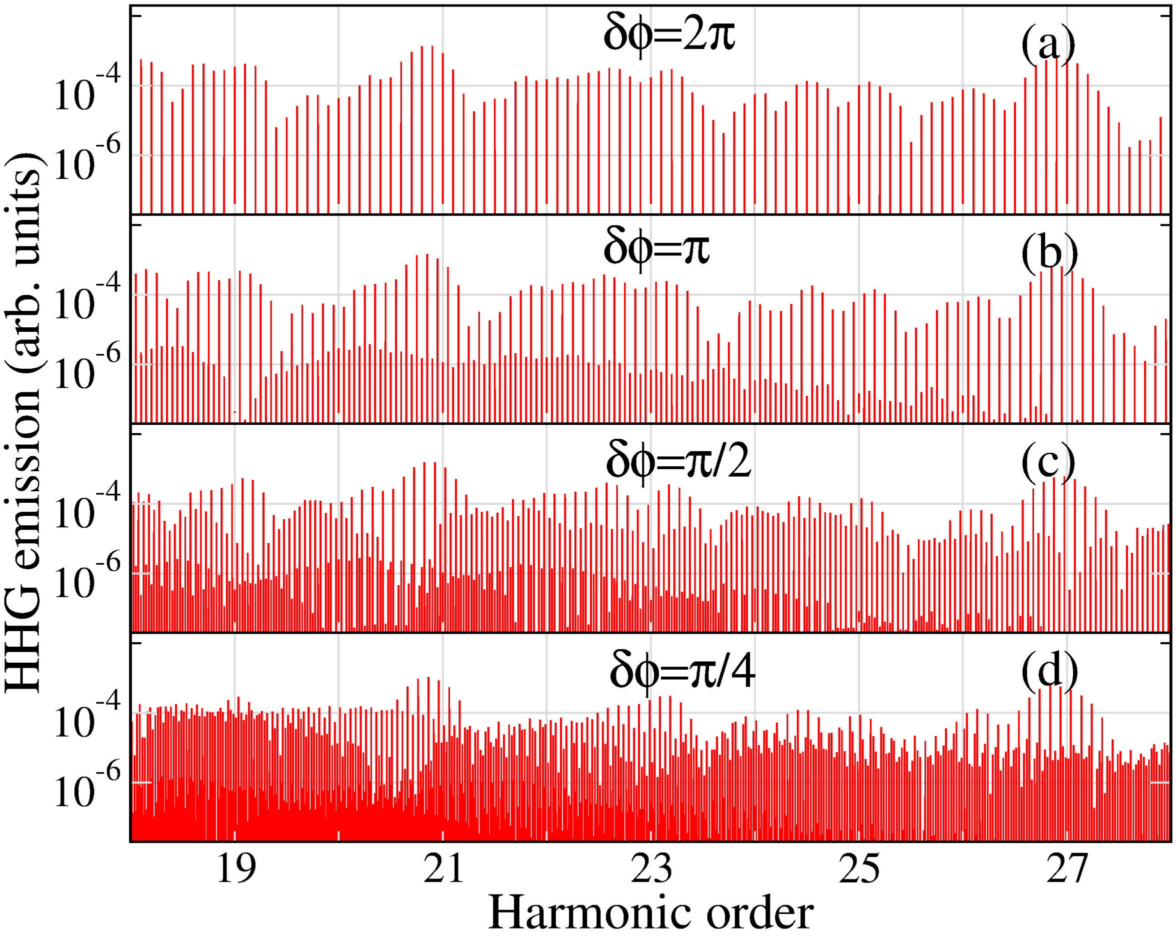

Figure 5.5: Structure of the XUV comb depending on the offset phase. The number of pulses is M=64. Each pulse has trapezoidal envelope. The length of the ramp is T_0, the plateau length is $2T_0$ and τ_r=$10T_0$.

Irrational CEP phase shift

If the offset frequency is an irrational multiple of the repetition frequency,

$$\omega_{\text{off}} = Q\omega_r, \;\; Q \in \mathbb{I}. \tag{5.21}$$

the XUV frequency comb is in general irregular. Since it is a problem to precisely stabilize the phase in an experiment, we investigate in the following whether it is possible to change the field properties to still be able to observe the XUV frequency comb even when $\delta\phi/\pi$ is an irrational number. In the following, the phase shift is $\delta\phi = \sqrt{2}/2$, so the offset frequency is

$$\omega_{\text{off}} = \sqrt{2}/(4\pi)\omega_r \approx 0.1125396\,\omega_r. \tag{5.22}$$

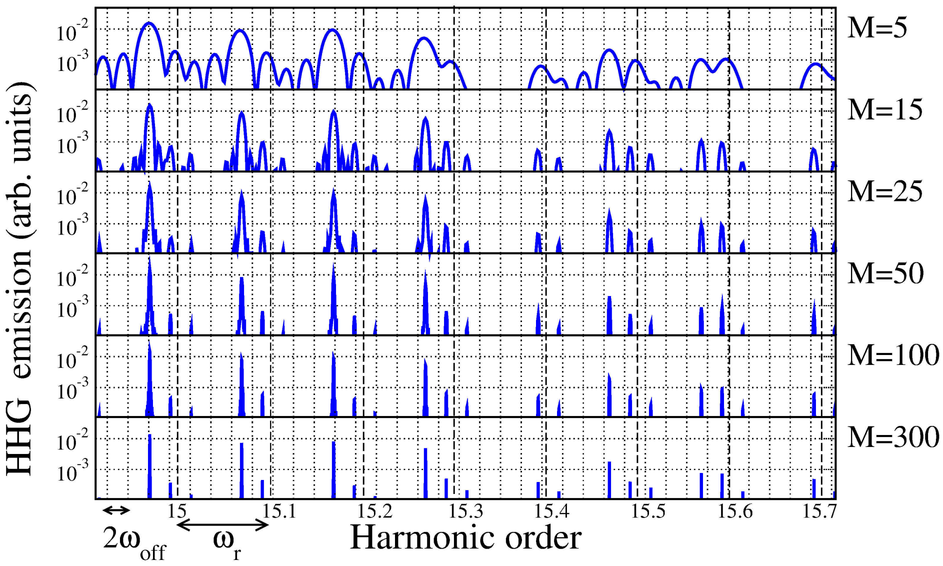

Figure 5.6: Structure of the XUV comb depending on number of pulses, M. The offset phase is $\delta\phi = \sqrt{2}/2$. Each pulse has a trapezoidal envelope consisting of 7 optical pulses; The length of the ramp is T_0, the plateau length is $5T_0$ and τ_r=$10T_0$.

We stress again that the offset frequency is dependent on the repetition frequency, which varies in the calculations below. Again, we vary two main parameters of the field: the pulse length and the train length.

HHG spectra from a pulse train of $M \in [5, 300]$ pulses is shown in Figure 5.6. One pulse has a trapezoidal envelope and consists of 7 optical pulses. The dashed (major) vertical grid lines are at frequencies $n\omega_r = 0.1n\omega_0$, the dotted (minor) grid lines are at multiples of $2\omega_{\text{off}} \approx 0.0225079\omega_0$. The positions of the two grid types lines never coincide. The plot shows the HHG spectra in a frequency range around the 15^{th} harmonic. From the top to the bottom, the train becomes longer. No regular comb structure is observed for a short pulse train ($M = 5$). As M increases, the teeth become narrower and more distinct. For M=300, we can see individual teeth in groups of three. The main teeth belonging to the 15^{th} harmonic order are separated by ω_r. Next to them at the distance $2\omega_{\text{off}}$, one can see minor teeth which can be attributed to odd harmonics of other orders. These are about ten times weaker than the main teeth near $\omega = 15\omega_0$ and become of the same order of magnitude for higher frequencies.

Figure 5.7 shows HHG spectra around the 11^{th} harmonic for the same irrational offset phase. In this case the train duration is kept constant, but the number of optical cycles per pulse, N, increases from the top to the bottom. In the top panel, the pulse has $\sin^2$ envelope, otherwise it is trapezoidal. The train is sufficiently long (200 pulses), such that all teeth are well distinguishable. Again, we show two types of grid lines:

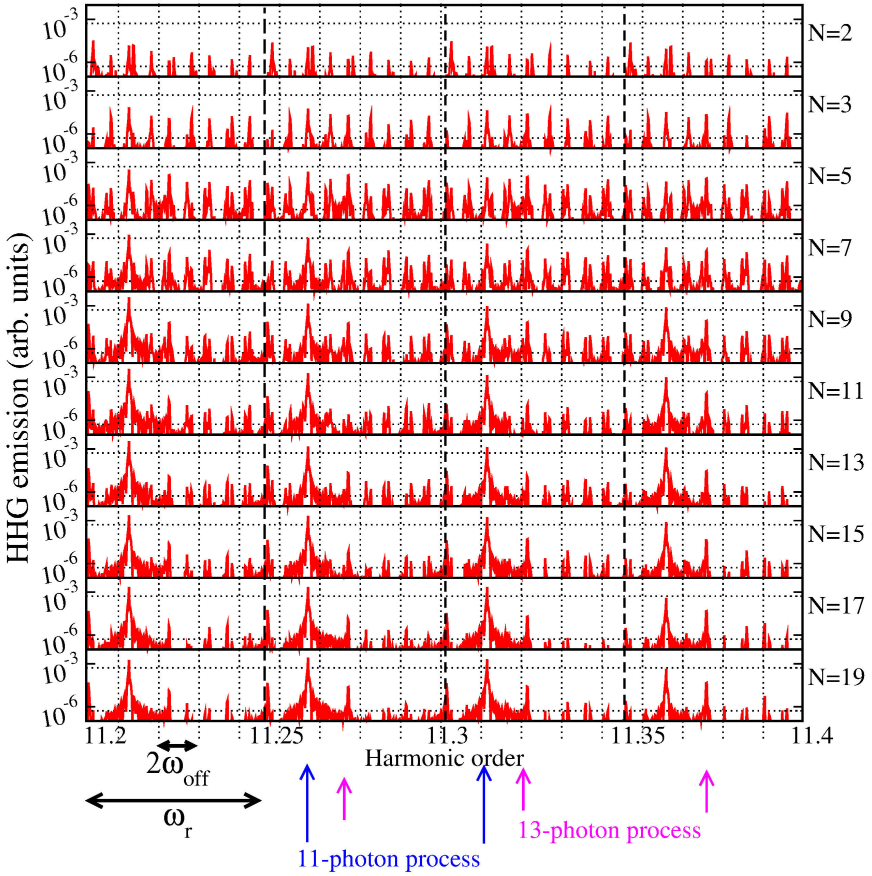

Figure 5.7: Structure of the XUV comb depending on the pulse length. N is the total number of optical cycles per pulse. The offset phase is $\delta\phi = \sqrt{2}/2$, τ_r=20T_0. The train consists of M=200 pulses. The length of the ramp is always T_0.

the dashed grid lines are at multiples of $\omega_r = 0.05\omega_0$ and the dotted grid lines are at multiples of $2\omega_{\text{off}} \approx 0.01125396\omega_0$. As the pulses become longer, the spectrum clears up and the teeth belonging to the 11^{th} harmonic dominate. Secondary teeth are due to the next odd harmonic. The main teeth are separated by ω_r. The minor teeth related to 13-photon absorption are separated from them by $2\omega_{\text{off}}$. Thus, we conclude that it is possible to observe an XUV frequency comb in the case when the offset phase of the driving field is an irrational fraction of π. The comb is regular in the case of a long train consisting of multi-cycle pulses.

5.5 Discussion

In this chapter, we have studied theoretically the possibility to generate XUV frequency combs by means of high-order harmonic generation. Our study confirmed the conclusion that interferences of different harmonic orders may lead to nested frequency combs. It would not be enough to provide the spectral resolution in the future experiments, but also the field parameters must be chosen appropriately to be able to distinguish the comb teeth. The is due to the fact that the pulse train is not infinitely long and thus the comb teeth curves are not δ-like and have finite width and specific shape; also, this is because in an experiment, the offset phase cannot be set by an observer equal to the desirable phase, but can rather be stabilized.

We have investigated the structure of such combs and in particular the spacing between the teeth as a function of laser pulse duration and pulse train length. Specifically, it was shown that in case that few-cycle pulses generating overlapping harmonics are used, the teeth density increases, requiring better spectral resolution, and the density depends on the offset frequency. On the other hand, the offset-frequency dependence of the spectrum allows us to see the "transparent" structure of the resulting HHG spectrum showing overlapping harmonics. XUV frequency comb generation makes it possible to represent the final HHG emission as a sum of components related to absorption of different number of photons.

For the first time, we have considered an offset frequency that is an irrational multiple of the repetition frequency since previous studies did not give an answer if a comb can be observed in such a case. We found that the comb can still be produced if the train is relatively long and consists of many-cycle pulses. In this case that the different harmonics do not overlap is met and the teeth are sufficiently narrow to be separated from each other. Following the recommendation of Carrera *et al.*,[21] the long pulse train should have moderate intensity in order to maintain carrier-envelope phase coherence.

Summary and future perspectives

In summary, we have investigated theoretically high harmonic generation from atoms in strong fields in situations that have received little attention previously.

We have investigated harmonic emission enhancement focusing on the laser target intrinsic properties and correlation between the target electronic spectrum and high harmonic generation spectrum. This approach differs from commonly pursued HHG enhancement by means of harmonic phase matching. The model developed in this Thesis was based on the single-active electron approximation.

We have shown that a single-atom simulation allows to observe a resonance in the high-harmonic spectrum when the system possesses a metastable state embedded to the continuum. By employing a model potential with a barrier, we have introduced a shape resonance in electron scattering in the course of high harmonic generation.

We have demonstrated that the excited state lifetime defines the time profile of the resonance emission. Our simulation showed that the signature of the resonance is a peak or group of peaks dominating over the rest of the HHG spectrum. The peak position does not depend on the field intensity. The relative enhancement and the peak width were determined by the shape of the potential barrier and electron-core recombination efficiency. Thereby, accurate analysis of prominent peaks in high harmonic generation spectrum may give a key to the target structure.

We have shown that the pulse duration does not affect the presence of the resonant peak in the HHG spectrum. Thus a few-cycle laser pulse with the possibility to vary the carrier-envelope phase can be used to observe the enhancement. The field ellipticity and temporal properties of the emission were investigated in order to test the mechanism of resonant harmonic enhancement. Our conclusions support the hypothesis that the returning electron recombines into the metastable excited state, and the emission at the resonant energy occurs due to the transition back to the ground state. Thus, high harmonic generation in presence of a shape resonance involves an additional step in comparison to the generalized simple mans model.

The positive potential barrier introduced in our model can be interpreted as a centrifugal barrier and screening effects of outer electron shells; further extension of the model to 3D is an opportunity to introduce these contributions separately. The study of the free electron angular distribution can provide additional information on properties of the resonance.

The model was tested by comparison with experimental results provided by the team of Prof. Ganeev for HHG in Mn plasma. The resonance observed by the team previously in the HHG spectrum was attributed to the giant $3p$ - $3d$ transition in Mn^+. Our calculations were in qualitative agreement with the experiment, proving that the model can be used to account for the resonance properties. We have explained the dominance of the resonant peak and disappearance of other harmonic orders observed in the experiment with an ultra-short laser pulse. It is an important conclusion of the simulation that the emission at the resonant energy in case of a few-cycle driving laser pulse has the form of a single subfemtosecond burst. We suggest that similar results can be obtained for other elements with similar properties. For instance, resonances in HHG from plasmas containing transition metals of the $3d$-block such as Fe, Co and Ni can be expected, as these elements are known for wide giant resonances in the range of 50-80 eV.

Information on the ratio of neutral atoms, singly and multiply charged ions would allow developing more accurate numerical models of HHG in plasmas, and cut-off and peak positions and heights could be predicted with better accuracy. Vice versa, HHG spectra for ultra-short laser pulses and the temporal profile of the emission can be used to extract information on the composition of the plasma.

In a medium, target atoms experience laser field intensity depending on their position. In order to consider macroscopic HHG, the transverse and longitudinal variation of the electric field due to laser beam intensity profile and the varying free-electron spatial distribution has to be taken into account. We have investigated the sensitivity of the resonance to the laser field intensity and used averaging over intensities to account for the transverse effects. We came to the conclusion that the resonance survives in a medium. In future studies, more accurate information can be extracted from the averaging procedure if the medium density distribution is taken into account and linked to the experimental beam intensity profile. Solving coupled Maxwell-Schrödinger equations is necessary to assess the intensity-averaging approximation and to incorporate longitudinal propagation effects.

The model allowed to dispense with time-consuming calculations and yet predict the behavior of the resonance in the HHG spectra as well as temporal characteristics of the emission. As it is experimentally challenging to measure attosecond pulses, one may suggest to generate harmonics in a medium containing alkali atoms. Since the alkali elements ionization potential is small, mid-infrared laser should be used. In this case, the produced harmonics are in the ultraviolet wavelength range, and the temporal characteristics can be resolved helping to understand the physics of the process. Alkali metal atoms are also convenient to test the suggested numerical model since they can be well described within single-electron approximation. The signature of the $s-p$ valence electron transition is expected to be in good agreement with the simulation results for a suitable effective potential.

Besides metastable states, we have considered high harmonic generation in the presence of an additional weak extreme ultraviolet beam leading to target excitation followed by tunnel ionization. We have shown that involvement of an excited state serves for more efficient high harmonic generation due to higher ionization rate. Time-frequency analysis of the spectrum showed periodic emission at the energy corresponding to the transition between the states, i.e. population transfer from the initial to the excited state and back. We varied the extreme ultraviolet field intensity and proved that the observed effect is attributed to Rabi oscillations. Manipulation of the model potential allowed us to explore the influence of the lifetime on the oscillation amplitude. To reach higher efficiency in the whole plateau region up to the cutoff, high harmonic generation must go through a bound excited state or a state with significant lifetime.

The dramatic increase of the harmonic generation efficiency was not the only effect of the laser-induced Rabi oscillations; the positions of the harmonics turned out to be shifted away from odd multiples of the laser frequency and split by the Rabi frequency. Existence of the splitting is determined by the extreme ultraviolet pulse duration and the excited state lifetime; for a relatively long XUV pulse duration, if the splitting is observed, changing the extreme ultraviolet (XUV) beam intensity can be used for fine tuning of the HHG peak positions. An admixture of easily ionized gas may be used as a source for a subfemtosecond XUV pulse in order to enhance the HHG emission without Rabi splitting.

We showed that the above threshold ionization probability can also be increased by orders of magnitude if a sufficiently long extreme ultraviolet pulse is applied.

The theoretical results are most applicable if the independent electron approach is a good approximation. The validity of the conclusions regarding the peaks shifts and splitting can be investigated, for instance, with the use of HHG from alkali atoms. It may be appropriate that the mid-infrared laser used to generate harmonics is accompanied by infrared laser. Strong coupling between the ground state and the first excited state in alkali atoms allows to manipulate the states population with high efficiency.

Another candidate, singly ionized helium, has $1s$ - $2p$ transition at 30.4 nm, and the $2p$ - state lifetime is about 100 ps, which makes it suitable for an experimental verification of the XUV-induced enhancement and Rabi splitting. Transition metals exhibiting giant resonances as mentioned above can also be used to enhance HHG emission by the presence of XUV.

The study can be extended to investigate high harmonic generation from molecules if the effective potential of the core and all-but-one electron exhibits a shape resonance.

The last part of the Thesis was dedicated to high harmonic generation used as a tool to create a frequency comb reaching the extreme ultraviolet. In our model, high harmonics were generated from argon atoms described with a soft-core potential driven by a pulse train with fixed pulse-to-pulse carrier envelope shift. We have found that using trains consisting of few-cycle laser pulses leads to an increased density of the comb. The nature of the effect is the overlap of structures attributed to different harmonic orders with different offset phase. The spectrum becomes "transparent": contribution of each harmonic order can be distinguished in the spectrum due to the comb structure.

The degree of overlap between different harmonic orders depends on the pulse duration and envelope, but not on the repetition frequency of the pulse train. This fact allowed us to use a model pulse train in order to save computation time. We considered the possibility to create a frequency comb if the offset is an irrational fraction of π. In general, such a phase shift destroys the comb structure and leads to an irregular spectrum. Nevertheless, in the simulation, as the pulse and the train became longer, peaks were better pronounced, and intermediate teeth due to the offset phase were less visible. We established the length of pulses and the train duration which that are necessary to observe a comb.

Since electron transitions in the target can affect harmonic peak positions, it also influences positions of comb teeth. We suggest that future studies focus on the effect that spectral properties of different target types have on the extreme ultraviolet frequency comb. Medium dispersion makes it important to consider in the future macroscopic propagation and its influence on the spacing of XUV frequency combs by a few-cycle laser pulse.

We believe that this work helps to understand fundamental properties and mechanisms of strong-field processes such as high harmonic generation and frequency comb creation, to set up related experiments and to further develop theoretical models.

Acknowledgements

I would like to express my gratitude to my scientific advisor Professor Dr. Manfred Lein and thank him for supervision, knowledge sharing, support, enthusiasm and patience. Also, I am grateful for the kind and relaxed work atmosphere, and I truly appreciated the company of all other group members. I would also like to thank my collaborators, the group of Prof. Ganeev, for their interest to my work, discussions and an opportunity to put our theoretical conclusions into practice.

References

[1] F. Adler, M.J. Thorpe, K.C. Cossel, and J. Ye. Cavity-Enhanced Direct Frequency Comb Spectroscopy: Technology and Applications. *Annual Review of Analytical Chemistry*, 3:175, 2010.

[2] C. Altucci, J.W.G. Tisch, and R. Velotta. Single attosecond light pulses from multi-cycle laser sources. *Mod. Opt.*, 58:1585, 2011.

[3] M. V. Ammosov, N. B. Delone, and V. P. Krainov. Tunnel ionization of complex atoms and of atomic ions in an alternating electromagnetic field. *JETP*, 64:1191, 1986.

[4] M. Ya. Amusia and J.-P. Connerade. The theory of collective motion probed by light. *Reports on Progress in Physics*, 63:41, 2000.

[5] P. Antoine, A. L'Huillier, and M. Lewenstein. Attosecond Pulse Trains Using High-Order Harmonics. *Phys. Rev. Lett.*, 77:1234, 1996.

[6] S.H. Autler and C.H. Townes. Stark Effect in Rapidly Varying Fields. *Phys. Rev.*, 100:703, 1955.

[7] N. Balakrishnan, C. Kalyanaraman, and N. Sathyamurthy. An Accurate and Efficient Scheme for Propagating the Time Dependent Schrödinger Equation. *Phys. Rep.*, 280:79, 1997.

[8] Ph. Balcou, P. Salières, A. L'Huillier, and M. Lewenstein. Generalized phase-matching conditions for high harmonics: The role of field-gradient forces. *Phys. Rev. A*, 55:3204, 1997.

[9] A.D. Bandrauk and N.H. Shon. Attosecond control of ionization and high-order harmonic generation in molecules. *Phys. Rev. A*, 66:031401, 2002.

[10] S. Batebi and M. Mohebbi. Two states hydrogenlike model for High-Order Harmonic Generation and enhanced XUV Generation from a coherent superposition of bound states. *ArXiv e-prints*, page arXiv:1104.3313, 2011.

[11] W. Becker, F. Grasbon, R. Kopold, D. B. Milošević, G. G. Paulus, and H. Walther. Above-threshold ionization: From classical features to quantum effects. *Advances In Atomic, Molecular, and Optical Physics Volume 48. Series: Advances In Atomic, Molecular, and Optical Physics*, 48:35, 2002.

[12] W. Becker, S. Long, and J.K. McIver. Modeling harmonic generation by a zero-range potential. *Phys. Rev. A*, 50:1540, 1994.

[13] M. Bellini, C. Lyngå, A. Tozzi, M. B. Gaarde, Hänsch, T. W., A. L'Huillier, and C.-G. Wahlström. Temporal coherence of ultrashort high-order harmonic pulses. *Phys. Rev. Lett.*, 81:297, 1998.

[14] J. Biegert, A. Heinrich, C.P. Hauri, W. Kornelis, P. Schlup, M.P. Anscombe, M.B. Gaarde, K. J. Schafer, and U. Keller. Control of high-order harmonic emission using attosecond pulse trains. *Journal of Modern Optics*, 53:87, 2006.

[15] A.M. Bonch-Bruevich and V.A. Khodovoi. Current methods for the study of the Stark effect in atoms. *Physics-Uspekhi*, 10:637, 1968.

[16] F. Brizuela, C.M. Heyl, P. Rudawski, D. Kroon, L. Rading, J.M. Dahlström, J. Mauritsson, P. Johnsson, C.L. Arnold, and A. L'Huillier. Efficient high-order harmonic generation boosted by below-threshold harmonics. *Sci. Rep.*, 3:1410, 2013.

[17] Rodíguez V.D. Barrachina R.O. Bustamante, M.G. Secondary peaks in the atomic ionization by a resonant laser pulse. *J. Phys.: Conf. Ser.*, 397:12014, 2012.

[18] C. Buth. High-order harmonic generation with resonant core excitation by ultraintense X-rays. *ArXiv e-prints*, page http://arxiv.org/abs/1303.1332, 2013.

[19] C. Buth, M. C. Kohler, J. Ullrich, and C. H. Keitel. High-order harmonic generation enhanced by XUV light. *Optics Letters*, 36:3530, 2011.

[20] C.J. Campbell, A.G. Radnaev, and A. Kuzmich. Wigner Crystals of ^{229}Th for Optical Excitation of the Nuclear Isomer. *Phys. Rev. Lett.*, 106:223001, 2011.

[21] J.J. Carrera and Sh.-I. Chu. *Ab initio* time-dependent density-functional-theory study of the frequency comb structure, coherence, and dephasing of multielectron systems in the vuv-xuv regimes via high-order harmonic generation. *Phys. Rev. A*, 79:063410, 2009.

[22] J.J. Carrera, S.-K. Son, and Sh.-I. Chu. *Ab initio* theoretical investigation of the frequency comb structure and coherence in the vuv-xuv regimes via high-order harmonic generation. *Phys. Rev. A*, 77:031401(R), 2008.

[23] C.C. Chirilă, I. Dreissigacker, E.V. van der Zwan, and M. Lein. Emission times in high-order harmonic generation. *Phys. Rev. A*, 81:033412, 2010.

[24] Xi Chu. Time-dependent density-functional-theory calculation of strong-field ionization rates of H_2. *Phys. Rev. A*, 82:023407, 2010.

[25] Xi Chu and G.C. Groenenboom. Time-dependent density-functional-theory calculation of high-order-harmonic generation of H_2. *Phys. Rev. A*, 85:053402, 2012.

[26] Xi Chu and G.C. Groenenboom. Role of resonance-enhanced multiphoton excitation in high-harmonic generation of N_2: A time-dependent density-functional-theory study. *Phys. Rev. A*, 87:013434, 2013.

[27] M.F. Ciappina, J.A. Pérez-Hernández, A.S. Landsman, T. Zimmermann, M. Lewenstein, L. Roso, and F. Krausz. Carrier-wave Rabi flopping signatures in high-order harmonic generation for alkali atoms. *ArXiv e-prints*, page http://arxiv.org/abs/1501.04021, 2015.

[28] A. Cingöz, D.C. Yost, Th.K. Allison, A. Ruehl, M.E. Fermann, I. Hartl, and J. Ye. Direct frequency comb spectroscopy in the extreme ultraviolet. *Nature*, 482:68, 2012.

[29] J.W. Cooper. Photoionization from Outer Atomic Subshells. A Model Study. *Phys. Rev.*, 128:681, 1962.

[30] P.B. Corkum. Plasma perspective on strong field multiphoton ionization. *Phys. Rev. Lett.*, 71:1994, 1993.

[31] S.T. Cundiff and J. Ye. *Colloquium* : Femtosecond optical frequency combs. *Rev. Mod. Phys.*, 75:325, 2003.

[32] S.T. Cundiff and J. Ye. Phase stabilization of mode-locked lasers. *J. Mod. Opt.*, 52:201, 2005.

[33] N. B. Delone. *Basics of Interaction of Laser Radiation with Matter.* Editions Frontieres, 1993.

[34] N. B. Delone. *Atom v silnom pole lazernogo izlucheniya (in Russian).* FIZMATLIT, 2002.

[35] N.B. Delone and V.P. Krainov. Tunneling and barrier-suppression ionization of atoms and ions in a laser radiation field. *Physics-Uspekhi*, 41:469, 1998.

[36] N.B. Delone and V.P. Krainov. AC Stark shift of atomic energy levels. *Physics-Uspekhi*, 42:669, 1999.

[37] N.B. Delone and V.P. Krainov. *Nelineinaya ionizaciya atomov lasernym izlucheniem (eng: Nonlinear ionization of atoms with laser radiation).* FIZMATLIT, 2001.

[38] J.-D. Deschênes and J. Genest. Calibrated low-noise frequency comb interference spectroscopy. In *Imaging and Applied Optics*, page FTu2D.1. Optical Society of America, 2013.

[39] S.A. Diddams, Th. Udem, J.C. Bergquist, E.A. Curtis, R. E. Drullinger, W.M. Itano L. Hollberg, W.D. Lee, C.W. Oates, K.R. Vogel, , and D.J. Wineland. An Optical Clock Based on a Single Trapped $^{199}\mathrm{Hg}^{+}$ Ion. *Science*, 293:825, 2001.

[40] V.K. Dolmatov. Characteristic features of the 3p absorption spectra of free iron-group elements due to the duplicity of the 'inner-valence' 3d electrons. *Journal of Physics B: Atomic, Molecular and Optical Physics*, 29:L687, 1996.

[41] J.N. Eckstein, A.I. Ferguson, and T.W. Hänsch. High-Resolution Two-Photon Spectroscopy with Picosecond Light Pulses. *Phys. Rev. Lett.*, 40:847, 1978.

[42] F.H.M. Faisal. Multiple absorption of laser photons by atoms. *J. Phys. B*, 6:L89, 1973.

[43] U. Fano. Effects of Configuration Interaction on Intensities and Phase Shifts. *Phys. Rev.*, 124:1866, 1961.

[44] M.V. Fedorov. *Interaction of Intense Laser Light with Free Electrons.* CRC Press, 1991.

[45] M.D. Feit, J.A. Fleck Jr., and A. Steiger. Solution of the schrödinger equation by a spectral method. *Journal of Computational Physics*, 47:412, 1982.

[46] M. Ferray, A. L'Huillier, X.F. Li, L.A. Lompre, G. Mainfray, and C. Manus. Multiple-harmonic conversion of 1064 nm radiation in rare gases. *Journal of Physics B: Atomic, Molecular and Optical Physics*, 21:L31, 1988.

[47] C. Figueira de Morisson Faria, M. Dörr, and W. Sandner. Importance of excited bound states in harmonic generation. *Phys. Rev.*, 58:2990, 1998.

[48] C. Figueira de Morisson Faria, R. Kopold, W. Becker, and J.M. Rost. Resonant enhancements of high-order harmonic generation. *Phys. Rev. A*, 65:023404, 2002.

[49] C. Figueira de Morisson Faria and I. Rotter. High-harmonic generation and periodic level crossings: time profile and control. *ArXiv e-prints*, page http://arxiv.org/abs/physics/0112076, 2001.

[50] C. Figueira de Morisson Faria and I. Rotter. High-Order Harmonic Generation in a Driven Two Level Atom: An Analogy with the Three-Step Model. *Laser Physics*, 13:985, 2003.

[51] Jr. Fleck, J.A., J.R. Morris, and M.D. Feit. Time-dependent propagation of high energy laser beams through the atmosphere. *Applied physics*, 10:129, 1976.

[52] A. Fleischer. Generation of higher-order harmonics upon the addition of high-frequency XUV radiation to IR radiation: Generalization of the three-step model. *Phys. Rev. A*, 78:053413, 2008.

[53] A. Fleischer and N. Moiseyev. Amplification of high-order harmonics using weak perturbative high-frequency radiation. *Phys. Rev. A*, 77:010102, 2008.

[54] A. Flettner, T. Pfeifer, D. Walter, C. Winterfeldt, C. Spielmann, and G. Gerber. High-harmonic generation and plasma radiation from water microdroplets. *Applied Physics B*, 77:747, 2003.

[55] H. Friedrich. *Theoretical Atomic Physics*. Springer-Verlag, 1991.

[56] M.V. Frolov and N.L. Manakov. Analytic theory of high-order-harmonic generation by an intense few-cycle laser pulse. *Phys. Rev. A*, 85:033416, 2012.

[57] M.V. Frolov, N.L. Manakov, and A.F. Starace. Potential barrier effects in high-order harmonic generation by transition-metal ions. *Phys. Rev. A*, 82:023424, 2010.

[58] M.B. Gaarde, Ph. Antoine, A. L'Huillier, K.J. Schafer, and K.C. Kulander. Macroscopic studies of short-pulse high-order harmonic generation using the time-dependent Schrödinger equation. *Phys. Rev. A*, 57:4553, 1998.

[59] M.B. Gaarde and K.J. Schafer. Enhancement of many high-order harmonics via a single multiphoton resonance. *Phys. Rev. A*, 64:013820, 2001.

[60] M.B. Gaarde, K.J. Schafer, A. Heinrich, J. Biegert, and U. Keller. Large enhancement of macroscopic yield in attosecond pulse train˘assisted harmonic generation. *Phys. Rev. A*, 72:013411, 2005.

[61] D Gabor. Theory of communication. part 1: The analysis of information. *J. Inst. Electr. Eng.*, 93:429, 1946.

[62] R. A. Ganeev, P. A. Naik, H. Singhal, J. A. Chakera, and P. D. Gupta. Strong enhancement and extinction of single harmonic intensity in the mid- and end-plateau regions of the high harmonics generated in weakly excited laser plasmas. *Opt. Lett.*, 32:65, 2007.

[63] R.A. Ganeev. Generation of high-order harmonics of high-power lasers in plasmas produced under irradiation of solid target surfaces by a prepulse. *Physics-Uspekhi*, 52:55, 2009.

[64] R.A. Ganeev. Generation of high-order harmonics of high-power lasers in plasmas produced under irradiation of solid target surfaces by a prepulse. *Phys. Usp.*, 52:55, 2009.

[65] R.A. Ganeev, L. Bom, J.-C. Kieffer, M. Suzuki, H. Kuroda, and T. Ozaki. Demonstration of the 101st harmonic generated from laser-produced manganese plasma. *Phys. Rev. A*, 76:023831, 2007.

[66] R.A. Ganeev, M. Suzuki, M. Baba, H. Kuroda, and T. Ozaki. Strong resonance enhancement of a single harmonic generated in the extreme ultraviolet range. *Opt. Lett.*, 31:1699, 2006.

[67] R.A. Ganeev, T. Witting, C. Hutchison, F. Frank, P.V. Redkin, W.A. Okell, D.Y. Lei, T. Roschuk, S.A. Maier, J.P. Marangos, and J.W.G. Tisch. Enhanced high-order harmonic generation in a carbon ablation plume. *Phys. Rev. A*, 85:015807, 2012.

[68] R.A. Ganeev, T. Witting, C. Hutchison, F. Frank, M. Tudorovskaya, M. Lein, W.A. Okell, A.Zaïr, J.P. Marangos, and J.W.G. Tisch. Isolated sub-fs xuv pulse generation in mn plasma ablation. *Opt. Express*, 20:25239, 2012.

[69] S. Ghimire, A.D. DiChiara, E. Sistrunk, P. Agostini, L. F. DiMauro, and D.A. Reis. Observation of high-order harmonic generation in a bulk crystal. *Nature Physics*, 7:138, 2011.

[70] C. Gohle, T. Udem, M. Herrmann, J. Rauschenberger, R. Holzwarth, H.A. Schuessler, F. Krausz, and T.W. Hänsch. A frequency comb in the extreme ultraviolet. *Nature*, 436:234, 2005.

[71] Ch. Gohle. *A Coherent Frequency Comb in the Extreme Ultraviolet*. PhD thesis, Ludwig Maximilians Universität München, 2006.

[72] A. Gordon, F. X. Kärtner, N. Rohringer, and R. Santra. Role of many-electron dynamics in high harmonic generation. *Phys. Rev. Lett*, 96:223902, 2006.

[73] A.K. Gupta and D. Neuhauser. Control of harmonic generation by initial-state preparation. *Chemical Physics Letters*, 290:543, 1998.

[74] I. Hadas and A. Bahabad. Macroscopic Manipulation of High-Order-Harmonic Generation Through Bound-State Coherent Control. *Phys. Rev. Lett.*, 113:253902, 2014.

[75] S. Haessler, J. Caillat, W. Boutu, C. Giovanetti-Teixeira, T. Ruchon, T. Auguste, Z. Diveki, P. Bregerand A. Maquet, B. Carré, R. Taïeb, and P. Salières. Attosecond imaging of molecular electronic wavepackets. *Nature Physics*, 6:200, 2010.

[76] S. Haessler, V. Strelkov, L. B. Elouga Bom, M. Khokhlova, O. Gobert, J.-F. Hergott, F. Lepetit, M. Perdrix, T. Ozaki, and P. Salières. Phase distortions of attosecond pulses produced by resonance-enhanced high harmonic generation. *New Journal of Physics*, 15:013051, 2013.

[77] B. Hemmerling. *Spectroscopy Using Quantum Logic*. PhD thesis, Leibniz Universität Hannover, 2011.

[78] M. Hentschel, R. Kienberger, C. Spielmann, G.A. Reider, N. Milosevic, T. Brabec, P.B. Corkum, U. Heinzmann, M. Drescher, and F. Krausz. Attosecond metrology. *Nature*, 414:509, 2001.

[79] R. Holzwarth, T. Udem, W.J. Wadsworth T.W. Hänsch, J.C. Knight, and P.S.J. Russell. Optical Frequency Synthesizer for Precision Spectroscopy. *Phys. Rev. Lett.*, 45:2264, 2000.

[80] K.L. Ishikawa. Photoemission and Ionization of He^+ under Simultaneous Irradiation of Fundamental Laser and High-Order Harmonic Pulses. *Phys. Rev. Lett.*, 91:043002, 2003.

[81] K.L. Ishikawa. Efficient photoemission and ionization of He^+ by a combined fundamental laser and high-order harmonic pulse. *Phys. Rev. A*, 70:013412, 2004.

[82] K.L. Ishikawa. High-Harmonic Generation. In Mikhail Grishin, editor, *Advances in Solid State Lasers Development and Applications*, chapter 19, page 439. InTech, Rijeka, 2010.

[83] J. Itatani, J. Levesque, H. Niikura D. Zeidler, H. Pépin, J.C. Kieffer, P.B. Corkum, and D.M. Villeneuve. Tomographic imaging of molecular orbitals. *Nature*, 432:867, 2004.

[84] I.A. Ivanov and A.S. Kheifets. High harmonics generation from excited states of atomic lithium. *Journal of Physics B: Atomic, Molecular and Optical Physics*, 41:115603, 2008.

[85] I.A. Ivanov and A.S. Kheifets. Resonant enhancement of generation of harmonics. *Phys. Rev. A*, 78:053406, 2008.

[86] C Jin, A.-T. Le, and C.D. Lin. Retrieval of target photorecombination cross sections from high-order harmonics generated in a macroscopic medium. *Phys. Rev. A*, 79:053413, 2009.

[87] D.J. Jones, S.A. Diddams, J.K. Ranka, A. Stentz, R.S. Windeler, J.L. Hall, and S.T. Cundiff. Carrier-Envelope Phase Control of Femtosecond Mode-Locked Lasers and Direct Optical Frequency Synthesis. *Science*, 288:635, 2000.

[88] R.J. Jones, K.D. Moll, M.J. Thorpe, and J. Ye. Phase-Coherent Frequency Combs in the Vacuum Ultraviolet via High-Harmonic Generation inside a Femtosecond Enhancement Cavity. *Phys. Rev. Lett.*, 94:193201, 2005.

[89] T. Kanai, Sh. Minemoto, and H. Sakai. Quantum interference during high-order harmonic generation from aligned molecules. *Nature*, 435:470, 2005.

[90] M. Kanno, T. Kato, H. Kono, Y. Fujimura, and F.H.M. Faisal. Incorporation of a wave-packet propagation method into the s-matrix framework: Investigation of the effects of excited state dynamics on intense-field ionization. *Phys. Rev. A*, 72:033418, 2005.

[91] L.V. Keldysh. Ionization in the field of a strong electromagnetic wave. *Zh. Eksp. Teor. Fiz.*, 47:1945, 1964.

[92] F. Keller and H. Lefebvre-Brion. Shape resonances in photoionization of diatomic molecules: An example in the inner shell ionization of the hydrogen halides. *Z. Phys. D*, 4:15, 1986.

[93] D. Kilbane, E.T. Kennedy, J.-P. Mosnier, P. van Kampen, and J.T. Costello. On the 3p-subshell photoabsorption spectra of iron-group ions: the case of Mn^{2+}. *Journal of Physics B: Atomic, Molecular and Optical Physics*, 38:L1, 2005.

[94] H. Kjeldsen, F. Folkmann, B. Kristensen, J.B. West, and J.E. Hansen. Absolute cross section for photoionization of Mn^+ in the 3p region. *Journal of Physics B: Atomic, Molecular and Optical Physics*, 37:1321, 2004.

[95] M.C. Kohler, T. Pfeifer, K.Z. Hatsagortsyan, and C.H. Keitel. Frontiers of Atomic High-Harmonic Generation. *Advances in Atomic Molecular and Optical Physics*, 61:159, 2012.

[96] R. Kosloff and H. Tal-Ezer. A direct relaxation method for calculating eigenfunctions and eigenvalues of the Schrödinger equation on a grid. *Chemical Physics Letters*, 127:223, 1986.

[97] J.L. Krause, K.J. Schafer, and K.C. Kulander. High-order harmonic generation from atoms and ions in the high intensity regime. *Phys. Rev. Lett.*, 68:3535, 1992.

[98] I.A. Kulagin and T. Usmanov. Efficient selection of single high-order harmonic caused by atomic autoionizing state influence. *Opt. Lett.*, 34:2616, 2009.

[99] L.D. Landau and E.M. Lifshits. *Quantum Mechanics (Non-relativistic Theory)*. Pergamon Press, Oxford, 1965.

[100] A.-T. Le, R.R. Lucchese, S. Tonzani, T. Morishita, and C.D. Lin. Quantitative rescattering theory for high-order harmonic generation from molecules. *Phys. Rev. A*, 80:013401, 2009.

[101] A.-T. Le, T. Morishita, and C.D. Lin. Extraction of the species-dependent dipole amplitude and phase from high-order harmonic spectra in rare-gas atoms. *Phys. Rev. A*, 78:023814, 2008.

[102] M. Lein, N. Hay, R. Velotta, J.P. Marangos, and P. L. Knight. Role of the intramolecular phase in high-harmonic generation. *Phys. Rev. Lett.*, 88:183903, 2002.

[103] M. Lewenstein, Ph. Balcou, M.Yu. Ivanov, A. L'Huillier, and P.B. Carré, Corkum. Theory of high-harmonic generation by low-frequency laser fields. *Phys. Rev. A*, 49:2117, 1994.

[104] Y. Liang, S. Augst, S.L. Chin, Y. Beaudoin, and M. Chaker. High harmonic generation in atomic and diatomic molecular gases using intense picosecond laser pulses-a comparison. *Journal of Physics B: Atomic, Molecular and Optical Physics*, 27:5119, 1994.

[105] C.D. Lin, A.-T. Le, Z. Chen, T. Morishita, and R. Lucchese. Strong-field rescattering physics - self-imaging of a molecule by its own electrons. *Journal of Physics B: Atomic, Molecular and Optical Physics*, 43:122001, 2010.

[106] Y. Mairesse, A. de Bohan, L.J. Frasinski, H. Merdji, L.C. Dinu, P. Monchicourt, P. Breger, M. Kovačev, R. Taïeb, B. Carré, H.G. Muller, P. Agostini, and P. Salières. Attosecond Synchronization of High-Harmonic Soft X-rays. *Science*, 302:1540, 2003.

[107] Y. Mairesse, J. Higuet, N. Dudovich, D. Shafir, B. Fabre, E. Mével, E. Constant, S. Patchkovskii, Z. Walters, M.Yu. Ivanov, and O. Smirnova. High harmonic spectroscopy of multichannel dynamics in strong-field ionization. *Phys. Rev. Lett.*, 104:213601, 2010.

[108] A. Marian, M.C. Stowe, J.R. Lawall, D. Felinto, and J. Ye. United Time-Frequency Spectroscopy for Dynamics and Global Structure. *Science*, 306:2063, 2004.

[109] B.K. McFarland, J.P. Farrell, Ph.H. Bucksbaum, and M. Gühr. High harmonic generation from multiple orbitals in N2. *Science*, 322:1232, 2008.

[110] A. McPherson, G. Gibson, H. Jara, U. Johann, T.S. Luk, I.A. McIntyre, K. Boyer, and C.K. Rhodes. Studies of multiphoton production of vacuum-ultraviolet radiation in the rare gases. *J. Opt. Soc. Am. B*, 4:595, 1987.

[111] M. Meyer, D. Cubaynes, P. O'Keeffe, H. Luna, P. Yeates, E. T. Kennedy, J. T. Costello, P. Orr, R. Taïeb, A. Maquet, S. Düsterer, P. Radcliffe, H. Redlin, A. Azima, E. Plönjes, and J. Feldhaus. Two-color photoionization in xuv free-electron and visible laser fields. *Phys. Rev. A*, 74:011401, 2006.

[112] P. Meystre and M. Sargent. *Elements of Quantum Optics*. Springer, 1999.

[113] D.B. Milošević. High-energy stimulated emission from plasma ablation pumped by resonant high-order harmonic generation. *Journal of Physics B: Atomic, Molecular and Optical Physics*, 40:3367, 2007.

[114] D.B. Milošević. Resonant high-order harmonic generation from plasma ablation: Laser intensity dependence of the harmonic intensity and phase. *Phys. Rev. A*, 81:023802, 2010.

[115] W. T. Mohamed, J. An, and D. E. Kim. *Generation of Few Cycle Femtosecond Pulses via Supercontinuum in a Gas-Filled Hollow-Core Fiber*, chapter 7, page 171. InTech, 2012.

[116] T. Morishita, A.-T. Le, Zh. Chen, and C.D. Lin. Accurate retrieval of structural information from laser-induced photoelectron and high-order harmonic spectra by few-cycle laser pulses. *Phys. Rev. Lett.*, 100:013903, 2008.

[117] H.G. Muller and F.C. Kooiman. Bunching and focusing of tunneling wave packets in enhancement of high-order above-threshold ionization. *Phys. Rev. Lett.*, 81:1207, 1998.

[118] A.M. Perelomov, V.S. Popov, and M.V. Terent'ev. Ionization of atoms in an alternating electric field. *Zh. Eksp. Teor. Fiz.*, 23:924, 1966.

[119] V.S. Popov. Tunnel and multiphoton ionization of atoms and ions in a strong laser field (Keldysh theory). *Physics-Uspekhi*, 47, 2004.

[120] S.V. Popruzhenko, D.F. Zaretsky, and W. Becker. High-order harmonic generation by an intense infrared laser pulse in the presence of a weak UV pulse. *Phys. Rev. A*, 81:063417, 2010.

[121] E. Priori, G. Cerullo, M. Nisoli, S. Stagira, and S. De Silvestri. Nonadiabatic three-dimensional model of high-order harmonic generation in the few-optical-cycle regime. *Phys. Rev. A*, 61:063801, 2000.

[122] M. Protopapas, C.H. Keitel, and Knight P.L. Atomic physics with super-high intensity lasers. *Rep. Progr. Phys.*, 60:389, 1997.

[123] I.I. Rabi. Space Quantization in a Gyrating Magnetic Field. *Phys. Rev.*, 51:652, 1937.

[124] G. Raşeev, B. Leyh, and H. Lefebvre-Brion. Autoionization in diatomic molecules: An example of electrostatic autoionization in CO. *Zeitschrift für Physik D Atoms, Molecules and Clusters*, 2:319, 1986.

[125] Ph. Raith, Ch. Ott, Ch.P. Anderson, A. Kaldun, K. Meyer, M. Laux, Y. Zhang, and Th. Pfeifer. Fractional high-order harmonic combs and energy tuning by attosecond-precision split-spectrum pulse control. *Appl. Phys. Lett.*, 100:121104, 2012.

[126] S. Rausch, T. Binhammer, A. Harth, F.X. Kärtner, and U. Morgner. Few-cycle femtosecond field synthesizer. *Opt. Express*, 16(22):17410, 2008.

[127] P.V. Redkin and R.A. Ganeev. Simulation of resonant high-order harmonic generation in a three-dimensional fullerenelike system by means of a multiconfigurational time-dependent hartree-fock approach. *Phys. Rev. A*, 81:063825, 2010.

[128] H.R. Reiss. Effect of an intense electromagnetic field on a weakly bound system. *Phys. Rev. A*, 22:1786, 1980.

[129] J.S. Robinson, C.A. Haworth, H. Teng, R.A. Smith, J.P. Marangos, and J.W.G. Tisch. The generation of intense, transform-limited laser pulses with tunable duration from 6 to 30 fs in a differentially pumped hollow fibre. *Appl. Phys. B*, 85:525, 2006.

[130] T. Brabec S. Patchkovskii, Z. Zhao and D.M. Villeneuve. High harmonic generation and molecular orbital tomography in multi-electrons systems: Beyond the single active electron approximation. *Phys. Rev. Lett*, 97:123003, 2006.

[131] Ch. Salomon, D. Hils, and J.L. Hall. Laser stabilization at the millihertz level. *J. Opt. Soc. Am. B*, 5:1576, 1988.

[132] K. Schiessl, E. Persson, A. Scrinzi, and J. Burgdörfer. Enhancement of high-order harmonic generation by a two-color field: Influence of propagation effects. *Phys. Rev. A*, 74:053412, 2006.

[133] C. Serrat and J. Biegert. Enhancement of HHG yield . *Nuclear Instruments and Methods in Physics Research Section A: Accelerators, Spectrometers, Detectors and Associated Equipment* , 653:134, 2011.

[134] B. Sheehy, J.D.D. Martin, L.F. DiMauro, P. Agostini, K.J. Schafer, M.B. Gaarde, and K.C. Kulander. High Harmonic Generation at Long Wavelengths. *Phys. Rev. Lett.*, 83:5270, 1999.

[135] A.D. Shiner, B.E. Schmidt, C. Trallero-Herrero, H.J. Worner, S. Patchkovskii, P.B. Corkum, J-C. Kieffer, F. Legare, and D. M. Villeneuve. Probing collective multi-electron dynamics in xenon with high-harmonic spectroscopy. *Nat. Phys*, 7:464, 2011.

[136] O. Smirnova, Y. Mairesse, S. Patchkovskii, N. Dudovich, D. Villeneuve, P. Corkum, and M.Y. Ivanov. High harmonic interferometry of multi-electron dynamics in molecules. *Nature*, 460:972, 2009.

[137] V. Strelkov. Role of autoionizing state in resonant high-order harmonic generation and attosecond pulse production. *Phys. Rev. Lett.*, 104:123901, 2010.

[138] V.V. Strelkov, M.A.Khokhlova, and N.Yu. Shubin. High-order harmonic generation and Fano resonances. *ArXiv e-prints*, pages http://arxiv–web3.library.cornell.edu/abs/1307.5241, 2013.

[139] T.R. Taha and M.I. Ablowitz. Analytical and numerical aspects of certain nonlinear evolution equations. II. Numerical, nonlinear Schrödinger equation. *Journal of Computational Physics*, 55:203, 1984.

[140] R. Taïeb, V. Véniard, J. Wassaf, and A. Maquet. Roles of resonances and recollisions in strong-field atomic phenomena. II. High-order harmonic generation. *Phys. Rev. A*, 68:033403, 2003.

[141] E.J. Takahashi, T. Kanai, K.L. Ishikawa, Y. Nabekawa, and K. Midorikawa. Dramatic Enhancement of High-Order Harmonic Generation. *Phys. Rev. Lett.*, 99:053904, 2007.

[142] E.J. Takahashi, Y. Nabekawa, H. Mashiko, Hirokazu Hasegawa, A. Suda, and K. Midorikawa. Generation of strong optical field in soft X-ray region by using high-order harmonics. *IEEE J. Sel. Top. Quant. Electron.*, 10:1315, 2004.

[143] M. Takamoto, F.-L. Hong, R. Higashi, and H. Katori. An optical lattice clock. *Nature*, 435:321, 2005.

[144] A. Trabesinger. Nobel Prize 2005: Glauber, Hall and Hänsch. *Nature Physics*, 1(2), 2005.

[145] M. Tudorovskaya and M. Lein. High-order harmonic generation in the presence of a resonance. *Phys. Rev. A*, 84:013430, 2011.

[146] M. Tudorovskaya and M. Lein. High-Harmonic Generation with Combined Infrared and Extreme Ultraviolet Fields. *J. Mod. Opt.*, 61:845, 2014.

[147] Th. Udem, R. Holzwarth, and T.W. Hänsch. Optical frequency metrology. *Nature*, 416:233, 2002.

[148] E.V. van der Zwan, C.C. Chirilă, and M. Lein. Molecular orbital tomography using short laser pulses. *Phys. Rev. A*, 78:033410, 2008.

[149] R. Velotta, N. Hay, M.B. Mason, M. Castillejo, and J.P. Marangos. High-order harmonic generation in aligned molecules. *Phys. Rev. Lett.*, 87:183901, 2001.

[150] C. Vozzi, F. Calegari, E. Benedetti, J.-P. Caumes, G. Sansone, S. Stagira, M. Nisoli, R. Torres, E. Heesel, N. Kajumba, J.P. Marangos, C. Altucci, and R. Velotta. Controlling two-center interference in molecular high harmonic generation. *Phys. Rev. Lett.*, 95:153902, 2005.

[151] T. Witting, F. Frank, C.A. Arrell, W.A. Okell, J.P. Marangos, and J.W.G. Tisch. Characterization of highintensity sub-4-fs laser pulses using spatially encoded spectral shearing interferometry. *Opt. Lett.*, 36:1680, 2011.

[152] T. Witting, F. Frank, W.A. Okell, C.A. Arrell, J.P. Marangos, and J.W.G. Tisch. Sub-4-fs laser pulse characterization by spatially resolved spectral shearing interferometry and attosecond streaking. *J. Phys. B*, 45:074014, 2012.

[153] M. Wollenhaupt, A. Assion, O. Bazhan, Ch. Horn, D. Liese, Ch. Sarpe-Tudoran, M. Winter, and T. Baumert. Control of interferences in an Autler-Townes doublet: Symmetry of control parameters. *Phys. Rev. A*, 68:015401, 2003.

[154] H.J. Wörner, H. Niikura, J.B. Bertrand, P.B. Corkum, and D.M. Villeneuve. Observation of electronic structure minima in high-harmonic generation. *Phys. Rev. Lett.*, 102:103901, 2009.

[155] www.fftw.org.

[156] D. Yost. *Development of an Extreme Ultraviolet Frequency Comb for Precision Spectroscopy.* PhD thesis, University of Colorado, 2011.

[157] D. Zhao, F.-l. Li, and Sh.-I. Chu. Coherent control and giant enhancement of multiphoton ionization and high-order-harmonic generation driven by intense frequency-comb laser fields: An *ab initio* theoretical investigation. *Phys. Rev. A*, 87:043407, 2013.

Curriculum Vitae

Personal information

Name	Maria Tudorovskaya
Birth date and place	14 May 1985, Moscow
Nationality	Russian

Education

2002-2008	Moscow Institute of Physics and Technology (B.Sc. and M.Sc.)
2009-2015	Kassel Universität/Leibniz Universität Hannover (Ph.D.)

List of publications

S.O. Adamson, M. Deminsky, A.V. Zaitsevskii, B.V. Potapkin, M. Tudorovskaya, I. Chernysheva, The role of dissociative electron attachment to metal halides in a low-pressure glow discharge, Russian Journal of Physical Chemistry B, 4:1, 2010

M. Tudorovskaya, and M. Lein, High-order harmonic generation in the presence of a resonance, Phys. Rev. A, 84:013430, 2011

R.A. Ganeev, T. Witting, C. Hutchison, F. Frank, M. Tudorovskaya, M. Lein, W.A. Okell, A. Zaïr, J.P. Marangos and J.W.G. Tisch, Isolated sub-fs XUV pulse generation in Mn plasma ablation, Opt. Express, 20:25239, 2012

M. Tudorovskaya, and M. Lein, High-Harmonic Generation with Combined Infrared and Extreme Ultraviolet Fields, J. Mod. Opt., 61:845, 2014